Empirical Relationship between Nightside Reconnection Rate and Solar Wind / Geomagnetic Measurements

Master's Thesis in Space Physics

by

Andreas Lysaker Kvernhaug

Department of Physics and Technology

University of Bergen

Norway

August, 2021

Abstract

According to the expanding-contracting polar cap paradigm (ECPC), dayside and nightside reconnection control magnetosphere-ionosphere dynamics at high latitudes by increasing and decreasing the open magnetic flux content, respectively. The dayside reconnection rate can be estimated using parameters measured in the solar wind, but there is no reliable and available proxy for the nightside reconnection rate. We aim to remedy this by using AMPERE to estimate a time series of open flux content. The AMPERE data set originates from the global Iridium satellite system, enabling continuous measurements of the field-aligned Birkeland currents, from which the open magnetic flux of the polar caps is derived. This method provides seven years of open flux change estimates. A series of nightside reconnection rates are then derived by directly relating the dayside reconnection rate to the estimated open flux change. Various proxies for the nightside reconnection rate are estimated by relating several geomagnetic indices with our estimated nightside reconnection rate through multivariate regression analysis.

By comparing the estimated open flux change with solar wind conditions and geomagnetic indices, we find our open flux estimates are highly dependent on the magnitude of the Birkeland currents. During low activity periods, the estimated open flux proves to be highly inaccurate with improving accuracy for higher activity periods. We also find that the nightside reconnection rate proxies fail to explain the majority of the variation in our estimated nightside reconnection rate series and propose that this is mainly due to the inaccuracy of our open flux estimates.

Acknowledgment

I would like to thank my supervisor Karl Laundal and co-supervisor Jone Peter Reistad for their consistent help and support throughout my master's work. I would also like to thank the Birkeland Centre for Space Science (BCSS) and the Dynamics of Asymmetric Geospace research group for their inclusive and engaging environment.

We thank the AMPERE team and the AMPERE Science Center for providing the Iridium-derived data products.

We acknowledge use of NASA/GSFC's Space Physics Data Facility's OMNIWeb service, providing solar wind and IMF conditions and geomagnetic indices.

We gratefully acknowledge the SuperMAG collaborators (https://supermag.jhuapl.edu/info/?page=acknowledgement) for providing geomagnetic indices.

Andreas Lysaker Kvernhaug

Bergen, August 2021

Contents

List of Abbreviations

AMPERE Active Magnetosphere and Planetary Electrodynamics Response Experiment

DMSP Defense Meteorological Satellite Program

DMSP SSJ Defense Meteorological Satellite Program Special Sensor J

ECPC Expanding-Contracting Polar Cap paradigm

FAC Field-Aligned Current

GSM Geocentric Solar Magnetospheric (coordinate system)

IMAGE Solar wind Magnetosphere Ionosphere Link Explorer

IMF Interplanetary Magnetic Field

MLAT Magnetic Latitude

MLT Magnetic Local Time

OCB Open-Closed field line Boundary

UT Universal Time

VIF Variance Inflation Factor

Chapter 1

Introduction

Earth's magnetosphere is the space surrounding the Earth dominated by its geomagnetic field. Outside the magnetosphere, the interplanetary magnetic field (IMF), originating from the Sun, is dominant. The solar wind propagates in conjunction with the IMF, carrying plasma from the Sun. The geomagnetic field within the magnetosphere is approximately shaped like a magnetic dipole close to Earth which becomes increasingly distorted further away due to interaction with the solar wind. This relationship between the solar wind and the magnetosphere is predominantly governed by the Dungey cycle, presented by *Dungey* (1961).

The Dungey cycle describes the dynamic movement of the geomagnetic field lines induced by interaction with the IMF. When the orientation of the interplanetary field lines has a southward pointing component, they couple with the northward pointing geomagnetic field lines at the subsolar point of the magnetosphere. The magnetopause magnetic coupling is generally referred to as dayside reconnection with a reconnection rate, Φ_D. Dayside reconnection causes the closed geomagnetic field lines, connected to both geomagnetic poles, to turn into open field lines magnetically connected to the Earth and the Sun. These open field lines are then pushed antisunward with the solar wind into the magnetotail stretching out behind the Earth. Magnetic pressure builds up in the magnetotail lobes, eventually causing the open magnetic field lines from the north and south pole to reconnect with each other in the magnetotail. The magnetotail reconnection is generally referred to as nightside reconnection with a reconnection rate, Φ_N.

Dayside and nightside reconnection are two of the fundamental processes driving ionospheric and magnetospheric electrodynamics. They significantly impact energetic particle precipitation, auroral events, magnetic storms, ionospheric plasma convection, and other processes. During stronger events, these processes can disrupt power grids on Earth's surface, cause radiation damage to satellites and destabilise low Earth orbit satellites due to

increased drag. Knowing the rate of dayside and nightside reconnection will then give considerable insight into these processes and how they depend on each other. Φ_D is dependent on the characteristics of the solar wind and can be readily estimated by applying solar winds measurements to empirically derived coupling functions (e.g. *Milan et al.*, 2015; *Newell et al.*, 2007; *Perreault and Akasofu*, 1978). Φ_N, on the other hand, is very difficult to measure. To circumvent this issue, several studies have resorted to using the expanding-contracting polar cap paradigm (ECPC) to measure the nightside reconnection rate indirectly.

The ECPC, introduced by *Cowley and Lockwood* (1992), gives a qualitative description of how the dayside and nightside reconnection rates are directly related to the topography of the polar caps. Dayside reconnection opens magnetic flux in the magnetosphere, increasing the size of the polar caps. Similarly, nightside reconnection closes the open flux, decreasing the size of the polar cap. Since nightside reconnection is generally delayed after dayside reconnection and their heterogeneous coupling rates, the polar caps experience a semi-periodic waxing and waning referred to as the ECPC. Based on the ECPC, if the dayside reconnection rate and the change in open flux of the polar cap are both known, the nightside reconnection rate can be estimated.

In earlier studies applying the ECPC, the open flux has been sporadically measured through auroral imaging over short periods (e.g. *Milan et al.*, 2007; *Ohma et al.*, 2018). In this study, we will attempt to establish a more continuous, long term estimate of the open flux. We will use the active magnetosphere and planetary electrodynamics experiment (AMPERE) to estimate a time series of open flux content. The AMPERE data set originates from the global Iridium satellite system, enabling continuous measurements of the field-aligned Birkeland currents. The open magnetic flux of the polar caps can be derived from the Birkeland current patterns. Using high time resolution open flux data derived from AMPERE and solar wind measurements from the OMNI data set, it should, in principle, be possible to provide a continuous estimate of the nightside reconnection rate.

The downside to this approach is that the AMPERE open flux series is an inaccurate and noisy data set compared to sporadic auroral imaging used in earlier studies. The open flux data also has to be differentiated, introducing additional complications. In this study, we sacrifice quality in favour of the quantity of open flux data to quantify the relationship of the ECPC. This study will explore how reliably the AMPERE open flux can estimate the nightside reconnection rate.

Laundal et al. (2020) suggested a method for estimating Φ_N using geomagnetic indices, correlated with magnetospheric coupling, which is the motivation for this project. Similar to this approach, we will use our derived open flux series to explore how geomagnetic indices can be used as a proxy for the nightside reconnection rate.

Chapter 2

Theoretical Background

2.1 The Sun and the Solar Wind

The Sun is crucial for the existence of life on Earth as we know it. Electromagnetic radiation from the Sun, mainly in the form of visible light, keeps the planet warm and able to sustain life. This radiation is due to the high surface temperature of around 6000 K, powered by thermonuclear reactions in the Sun's core, where temperatures can reach as high as 1.57×10^7 K. The heat generated in the Sun's interior is transported towards the surface and into the solar atmosphere through radiation and convection.

Another significant way the Sun affects the Earth, especially Earth's magnetosphere, is through the solar wind and its accompanying magnetic field, called the *interplanetary magnetic field* (IMF), which originates from the Sun. The solar wind consists of hot plasma released from the upper atmosphere of the Sun, travelling radially out of the Sun at typically 400 km/s along with the IMF. The solar wind plasma travels together with the Sun's magnetic field due to the infinite conductivity of the fully ionised plasma, known as the frozen-in approximation. The frozen-in approximation means that the plasma and the magnetic field travel together. Subsequently, the IMF in the heliosphere takes on a characteristic spiral structure caused by the rotation of the sun.

2.1.1 The Parker Spiral

Without going into further detail, the rotation of the Sun and the frozen-in concept causes the IMF to assume a spiral formation known as the Parker spiral (*Parker*, 1958). Figure 2.1 shows a simple illustration of the Parker spiral seen from above the solar system. The curved black lines are the interplanetary magnetic field lines originating from the Sun at the centre. Frozen into the IMF, the solar wind travels radially out of the Sun at speeds of ~ 300 km/s.

The dashed line shows the orbit of the Earth.

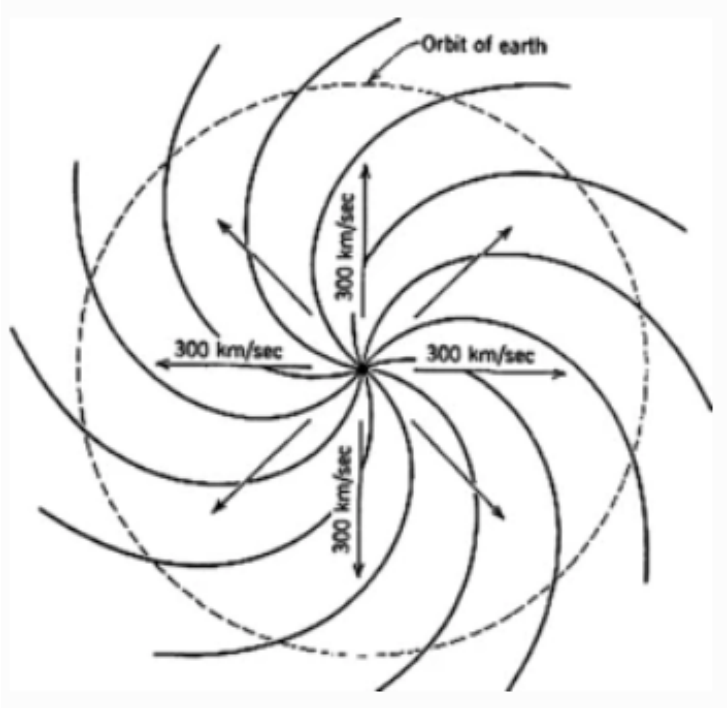

Figure 2.1: Illustration of the Parker spiral seen from above. Figure from *Akasofu* (2011).

2.1.2 The Heliospheric Current Sheet

With the IMF frozen in with the plasma, a current is induced at the boundary where the polarity of the Sun's magnetic field changes from away from the Sun to towards the Sun. The boundary is known as the heliospheric current sheet, illustrated in Figure 2.2 as the three-dimensional structure originating from the Sun. The smaller illustration to the upper right shows the Sun represented by the circle to the left and the Earth represented by the circle to the right in a vertical plane. The thick curved line represents the current sheet with the magnetic field lines moving along the current sheet with opposite polarities on either side. The current sheet assumes a wavy spiral shape due to the tilt of the magnetic axis relative to the rotation axis of the Sun and magnetic activity on the Sun. The interplanetary field lines can assume almost any direction in three-dimensional space when they reach the Earth. Because of the shape of the Parker spiral, the IMF x-component, B_x, will be negatively correlated with the y-component B_y, relative to the *geocentric solar magnetospheric coordinate system* (GSM). So when B_x is positive, B_y is negative and vice versa. B_z has a lesser correlation with the other components and can be positive or negative in both cases. The GSM coordinate system has its origin at the Earth's centre, with the x-axis pointing directly towards the Sun. The z-axis is the Earth's magnetic dipole axis (positive towards North) projected onto

the plane perpendicular to the x-axis.

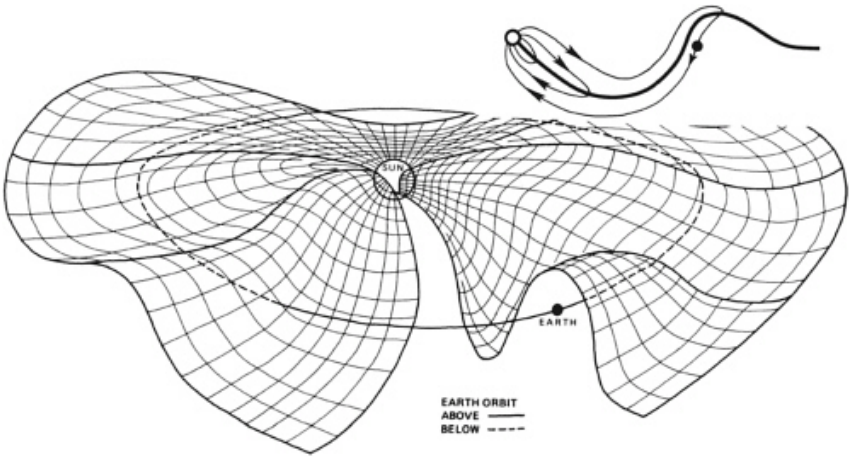

Figure 2.2: The large schematic shows a three-dimensional illustration of the heliospheric current sheet. The smaller illustration to the upper right shows the interplanetary magnetic field-lines moving along the current sheet in the Sun's equatorial plane. Figure courtesy of Akasofu S.-I.

2.2 The Geomagnetic Field

Earth's magnetic field extends into space from its interior, with convection currents in the outer core generating the magnetic field (*Borovsky and Valdivia*, 2018). The magnetic field generated by the Earth is approximately that of a dipole field with the dipole axis tilted about 9 degrees respective to Earth's rotation axis. However, due to interaction with the solar wind and the IMF, the dipole field approximation becomes increasingly distorted further into space. Figure 2.3 shows the distortion of the geomagnetic field around the Earth. The dashed lines show a normal dipole field for comparison, while the solid lines show the distorted geomagnetic field. On the left side, facing the Sun, the closed field lines on the dayside are compressed by the solar wind pressure and the remaining field lines are dragged antisunward into a magnetotail. This process will be covered in more detail in the next section.

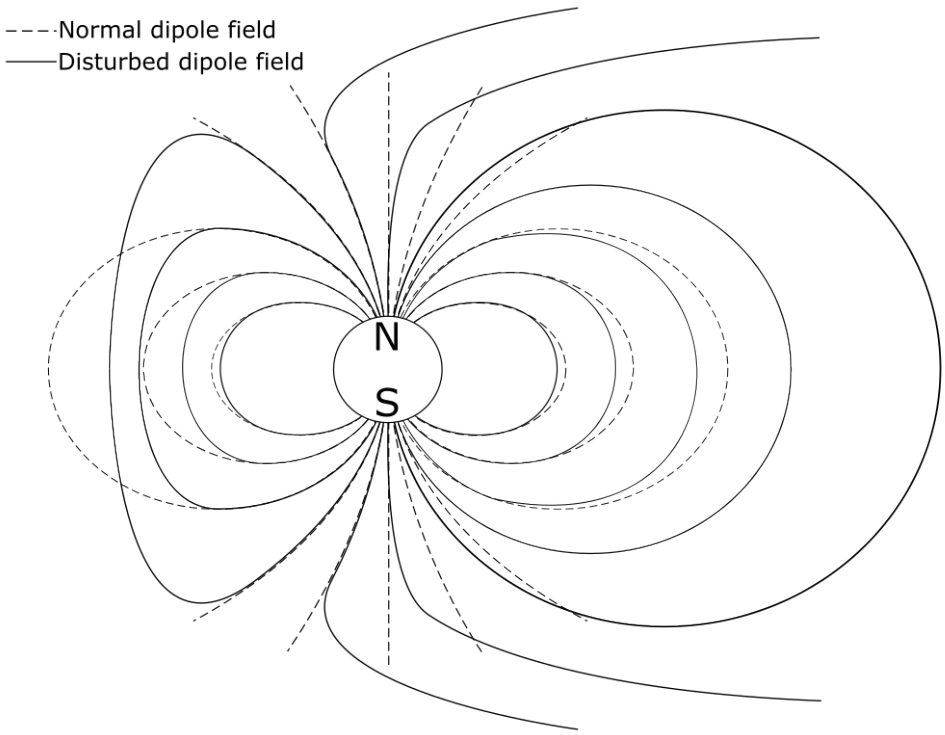

Figure 2.3: The dashed lines indicate an undisturbed magnetic dipole field. The solid lines illustrate the geomagnetic field, disturbed by the solar wind.

2.3 The Dungey Cycle

The Dungey cycle illustrated in Figure 2.4, suggested by and subsequently named after *Dungey* (1961), formulates how the IMF interacts with the geomagnetic field when the IMF is pointing roughly southwards. Consider the solar wind travelling toward Earth with the IMF pointing southward. When the IMF is brought close to the magnetopause by the solar wind, the southward pointing field lines of the IMF will couple with the northward pointing geomagnetic field lines in a process called magnetic reconnection. The reconnecting field lines are numbered 1' and 1 in figure 2.4, commonly referred to as dayside reconnection. After the interplanetary magnetic field line and the geomagnetic field line have reconnected, they will turn into open magnetic field lines connected to both the Earth and the Sun. After reconnecting, the open magnetic field lines are pushed towards the nightside of the Earth due to the kinetic energy of the solar wind (2-5 and 2'-5' in figure 2.4). The field lines fastened to the Earth will be gradually stretched antisunward into a long tail-like shape, called the magnetotail. With continuing reconnection on the dayside, magnetic pressure will build up in the magnetotail. The build-up will eventually cause the open magnetic field lines of the northern and southern hemispheres to couple with each other the same way the IMF and the geomagnetic field lines couple with each other during dayside reconnection. The coupling

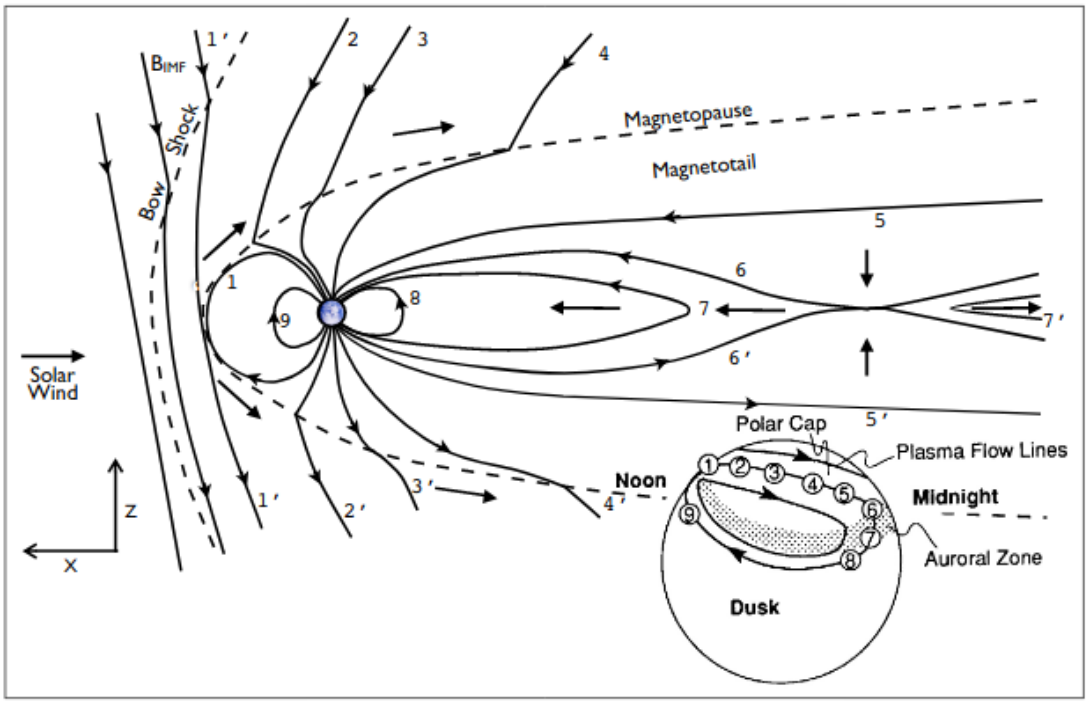

Figure 2.4: The Dungey cycle in the magnetosphere and the ionosphere. The numbers indicate the movement of a magnetic field line. Figure from *Kivelson et al.* (1996)

in the magnetotail is usually referred to as nightside reconnection, represented by the field lines numbered 6 and 6' in figure 2.4. After the field lines have reconnected on the night side, they return to a closed field line numbered 7 and another interplanetary field line numbered 7'. The closed field line will then move back toward the dayside like the field lines numbered 8 and 9 in figure 2.4.

The smaller illustration to the lower right in figure 2.4 shows where the magnetic field lines intersect Earth's ionosphere as they move across the polar cap, with the numbers matching those of the main illustration. The ionospheric footprint of the magnetospheric convection described by the Dungey cycle is also shown in figure 2.5 as the continuous arrowed lines, indicating the direction of the convection. Here the numbers represent the *magnetic local time* (MLT) of the ionosphere, where 12 MLT is towards the Sun and 24 MLT is antisunward. The circle represents the *open-closed field line boundary* (OCB). The auroral zone is just equatorward of the OCB. Outside the OCB are the closed field lines (7-8 in figure 2.4), and inside the OCB, also known as the polar cap, are the open field lines (2-5 in figure 2.4). The ionospheric location of the dayside and nightside reconnection (1 and 6 in figure 2.4) are shown as the dashed lines of the OCB at 12 MLT and 24 MLT respectively in figure 2.5.

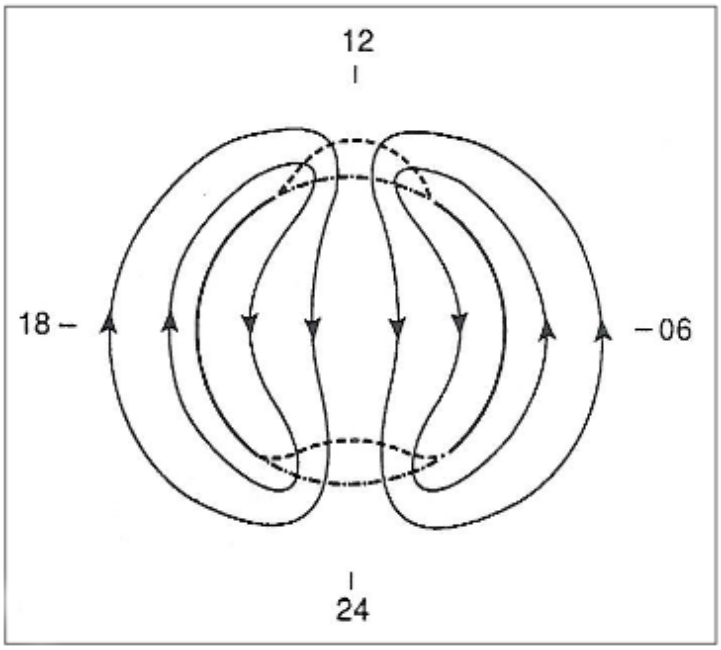

Figure 2.5: The flow of plasma mapped to the magnetic field lines just above the ionosphere at high latitudes. The circle represents the open-closed field line boundary, and the area inside the circle is called the polar cap. Figure from *Cowley and Lockwood* (1992)

2.4 Geomagnetic Open Flux

In electromagnetism, the magnetic flux through a surface is given by the normal component of the total magnetic field through a given surface multiplied by the area of the surface. In the geomagnetic field, the open magnetic flux refers to geomagnetic field lines, coupled with the IMF. In contrast, the closed magnetic flux is the field lines enclosed within the geomagnetic dipole field, such that the field lines have both footpoints on Earth. As previously mentioned, the OCB denotes the boundary between the open field lines and the closed field lines. The total open magnetic flux, F_{PC}, is given by the surface integral of the radial component of the magnetic field over the polar cap:

$$F_{PC} = \int^{polar\ cap} \mathbf{B} \cdot d\mathbf{A} \tag{2.1}$$

where **B** is the magnetic field orthogonal to the surface, A, in our case **B** is the radial component of the geomagnetic field, passing through the polar cap.

2.5 The Expanding-Contracting Polar Cap Paradigm

The *expanding-contracting polar cap paradigm* (ECPC) presented by *Cowley and Lockwood* (1992), details how the open magnetic flux of the polar caps varies in response to a two-component ionospheric flow model. First, we look at the nature of the open flux of the polar caps. The first component is driven by the dayside reconnection rate, which increases the open flux of the polar cap. Similarly, the second component is driven by the nightside reconnection rate, responsible for decreasing the open flux of the polar cap. Here, the magnetic reconnection rate describes the rate at which magnetic flux is transferred from an open to a closed topology and vice versa. With magnetic flux given in Tm^2 or Wb, change in flux due to magnetic reconnection is given in units Wb/s, which is the same as voltage V.

Figure 2.6 illustrates the response of the polar cap to an impulse of dayside reconnection from three different perspectives. In the first row, we see the Earth in the equatorial GSM X-Y plane as the small circle with the black curve representing the magnetopause with the closed field line magnetosphere shaded grey. The field lines at the magnetopause map down to the OCB in the ionosphere. Initially, we have a closed flux of $F_{tot}-F$, where F_{tot} is the total magnetic flux of each hemisphere of the magnetosphere and F is the open flux of the polar caps. The second row shows the open-closed topography of a cross-section of the magnetotail within the magnetopause (solid circle). Shaded in grey, we again have the closed field lines of the magnetotail plasma sheet. Above are the open flux field lines mapping to the northern hemisphere polar cap. Equivalently below are the open flux field lines mapping to the southern hemisphere polar cap. The third row illustrates the polar cap with open flux F within and MLT 12 pointing towards the Sun. The second column shows the opening of flux and excitation of flows from the onset of dayside reconnection. In the first row, we see a bulge in the magnetopause of previously closed field lines converted to open field lines with a total flux change dF. In the second row, these newly opened field lines will move with the solar wind toward the magnetotail as we saw in field lines 2-4 and 2'-4' in figure 2.4. The open field lines reach the magnetotail, usually within a few to tens of minutes depending on the solar wind speed and how far back in the magnetotail we are looking. The field lines will converge into the lobes creating similar bulges in the magnetopause boundary of open flux dF. In the third row, we see a bulge created sunwards in the polar cap of open flux dF. This bulge maps to the newly reconnected field lines created at the magnetopause illustrated in the first row. The perturbations created in the respective boundaries represents a deviation from an equilibrium state, exciting dynamic flows, represented by the blue arrows, approaching a new zero-flow equilibrium. The third column shows the new zero-flow equilibrium boundaries with the previous boundaries as the dashed red lines. In the new equilibrium, we have a total open flux of $F+dF$ in each hemisphere. The total flux of the magnetosphere hemispheres

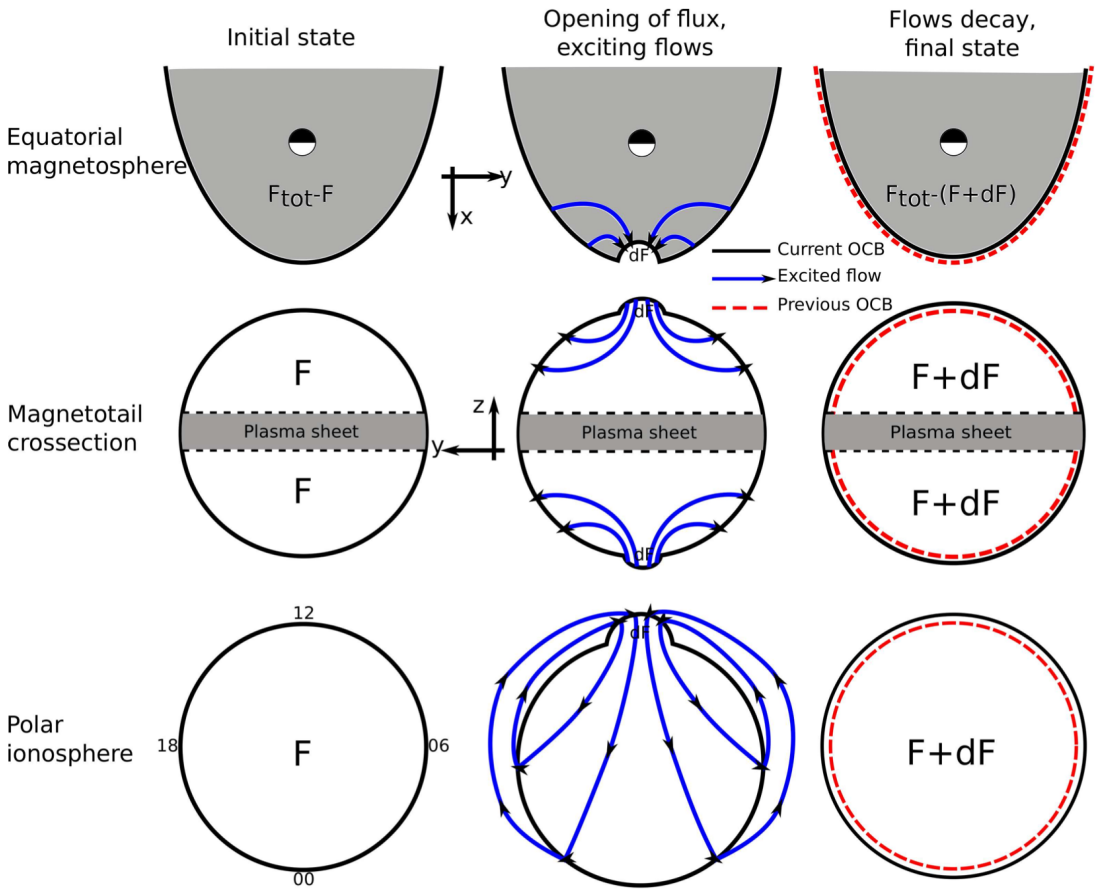

Figure 2.6: Illustration of a dayside reconnection event. The first row illustrates the magnetosphere from the equatorial plane. The second row shows a cross-section of the magnetotail and the final row shows the polar cap ionosphere. The first column shows the respective systems at their initial state. The second row shows the reaction induced by the onset of dayside reconnection. The last row shows the aftermath of the dayside reconnection event. Reillustrated from figures 5 and 6 in *Cowley and Lockwood* (1992)

F_{tot} remains unchanged.

Similarly to the third row in figure 2.6, the polar cap has the opposite response to impulsive nightside reconnection as shown in figure 2.7. Initially, we start with an open flux F. At the onset of nightside reconnection, open magnetic field lines in the magnetotail couples, akin to field lines 6 and 6' in figure 2.4. These field lines map to Earth's surface inside the OCB on the antisunward edge. This coupling creates a bulge of closed flux dF inside the previous OCB (Fig. 2.7b). The warping of the OCB will again create instability in the polar cap, exciting ionospheric flow towards a new zero-flow equilibrium represented by the arrows in figure 2.7c. Afterwards the polar cap reaches a new equilibrium of open flux $F - dF$ (Fig. 2.7d).

The rate of magnetic reconnection at the dayside is dependent on conditions in the solar wind and, most importantly, the orientation of the IMF. The magnetic reconnection on the

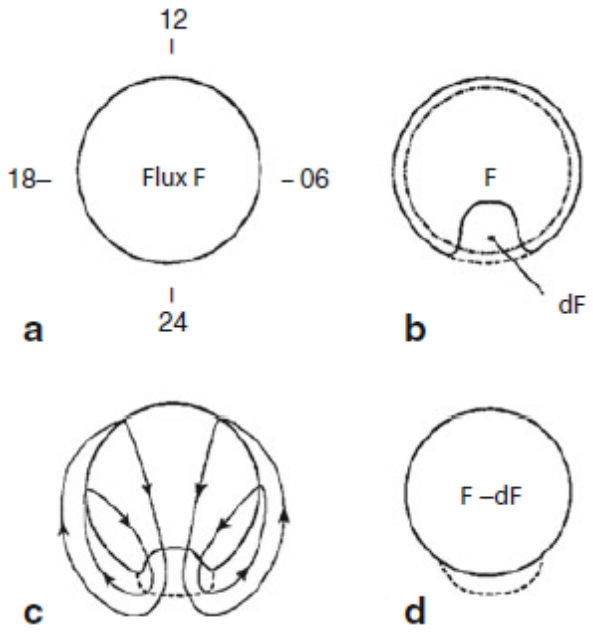

Figure 2.7: Illustration of the polar cap reaction to a nightside reconnection event. Figure from *Cowley and Lockwood* (1992)

nightside cannot instantaneously adjust to match the dayside reconnection, resulting in significant variations in the amount of open flux in the polar caps. Changes in the open flux, and hence the size of the polar cap, can be a measure of the global reconnection rates. The voltage, or flux transfer rates, on the dayside and nightside, is usually considered to be the only means by which the amount of open flux can change (*Milan et al.*, 2017). This direct relationship gives us the following continuity equation for open flux:

$$\frac{dF_{PC}}{dt} = \Phi_D - \Phi_N \tag{2.2}$$

where dF_{PC}/dt is the rate of change in the open flux of the polar caps, Φ_D the dayside reconnection rate, and Φ_N the nightside reconnection rate, and has dimensions of Wb/s or equivalently volts (V) (*Milan* (2015)). Equation 2.2 is a variation of Faraday's law, requiring that the change in open magnetic flux within a closed loop (here described by the OCB) is equal to the electric field integrated around the boundary (here associated with the dayside and nightside reconnection). In the magnetosphere system, Φ_D is responsible for the accumulation of open magnetic flux in the system and expanding the polar caps. This accumulation of open flux leads to an inflation of the magnetotail lobes, building up magnetic pressure. When this build-up is sufficiently high, the magnetic pressure is released by initiating magnetic reconnection in the magnetotail. The release reduces the amount of open flux in the magnetosphere, given that Φ_N is greater than Φ_D, which is typically the case when Φ_N is present. Integrated over sufficiently long timescales, typically a few hours *Laundal*

et al. (2020), the release of open flux in the magnetotail must balance its accumulation at the magnetopause:

$$\langle \Phi_N \rangle = \langle \Phi_D \rangle \tag{2.3}$$

Over shorter timescales, however, the variation of F_{PC} can be as significant as a factor of 4 or more, between 2.5% and 12% of the total magnetospheric flux (*Milan et al.*, 2004).

2.6 The Dayside Coupling Function

There have been many attempts at quantifying the coupling of energy from the solar wind into the magnetosphere. Dayside coupling is driven by the amount of the IMF Poynting flux entering the magnetosphere, first defined as the ϵ parameter *Perreault and Akasofu* (1978):

$$\epsilon = \frac{4\pi}{\mu_0} L_0^2 V_X B^2 \sin^4 \frac{1}{2}\theta \tag{2.4}$$

Here V_X is the negative x-component of the solar wind speed in the GSM coordinate system, $B = \sqrt{B_X^2 + B_Y^2 + B_Z^2}$ is the magnitude of the IMF based on their respective GSM components, and θ is the clock-angle between the IMF vector and the z-axis in the GSM Y-Z plane, $\theta = \arctan 2(B_Y, B_Z)$. For IMF along the positive Z-axis, we will then have a clock angle of 0° resulting in no reconnection. With IMF along the negative Z-axis, we have a clock-angle of 180° resulting in maximum dayside reconnection. L_0^2 is an approximate measure of the cross-section of the magnetopause exposed to the interplanetary Poynting flux and was in the previous paper estimated to be about $L_0 \approx 7R_E$. B^2/μ_0 is proportional to the electromagnetic energy density in the solar wind, and V_X is the rate of transport toward the magnetosphere. $\sin^4(\theta/2)$ represents the clock-angle dependency of the coupling between the solar wind and the magnetosphere. The coupling rate goes from zero to a maximum as the IMF rotates from a parallel to an anti-parallel alignment with the northward-pointing geomagnetic field.

Figure 2.8 illustrates a diagram of the magnetosphere with closed magnetic field lines in red and open magnetic field lines in blue in the GSM X-Z plane. Φ_D quantifies the rate of flux opening at the dayside, while Φ_N quantifies the flux closing on the nightside. The dayside reconnection rate is dependent on the upstream solar wind speed V_X and the magnitude and orientation of the interplanetary magnetic field **B**.

Many studies have used ϵ for estimating the magnetospheric energy input and then subsequently attempt to determine the partitioning of this energy into different energy sinks. Au-

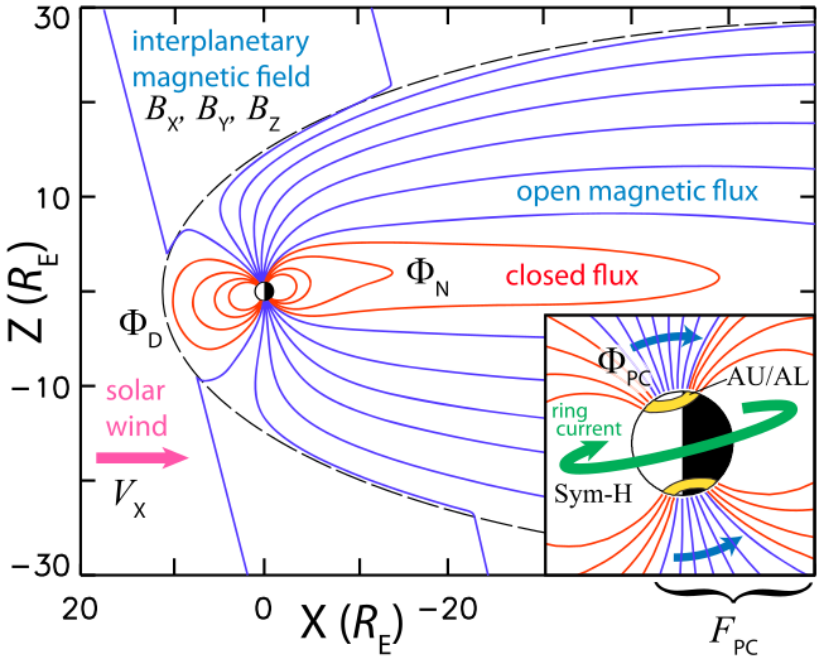

Figure 2.8: Illustration of the magnetosphere with closed magnetic field lines in red and open field lines in blue. Φ_D quantifies the rate of flux opening at the dayside magnetopause and Φ_N the rate of flux closing in the nightside magnetotail. Φ_D depends on the solar wind speed towards the subsolar point, V_X, and the orientation and magnitude of the IMF, **B**. The lower right panel shows the near-Earth magnetosphere with related regional geomagnetic indices. Figure from *Milan et al.* (2012)

roral precipitation power, joule heating, energisation of the ring current and auroral electrojets are among these energy sinks. These energy sinks are very difficult to measure directly, leading to geomagnetic indices being used as proxies for the relative amount of energy transferred to the different magnetospheric systems *Scurry and Russell* (1991). These energy sinks and geomagnetic indices will later be discussed in more detail.

The inset panel in figure 2.8 shows the areas around the OCB where the auroral electrojet currents are illustrated in yellow, and the ring current around the Earth equator illustrated in green, with the related geomagnetic indices AU/AL and SYM-H, respectively. Several studies correlating geomagnetic indices and upstream solar wind conditions have been performed to improve upon the ϵ parameter. One of these correlative studies, using ten different magnetospheric variables, were performed by *Newell et al.* (2007) resulting in the following coupling function:

$$\frac{d\Phi_{MP}}{dt} = V_X^{4/3} B_{YZ}^{2/3} \sin^{8/3}\frac{1}{2}\theta \tag{2.5}$$

where $B_{YZ} = \sqrt{B_Y^2 + B_Z^2}$ is the magnitude of the IMF in the GSM Y-Z plane, $d\Phi_{MP}/dt$ describes the rate of magnetic flux opening at the magnetosphere. An issue with using geomagnetic indices when estimating Φ_D is that they are also affected by Φ_N, which are poorly correlated over short timescales, leading to correlative studies resorting to data averaging over long timescales, up to several hours, where $\langle\Phi_N\rangle = \langle\Phi_D\rangle$ as mentioned in the previous section.

Another possible method is determining Φ_D through the excitation of ionospheric convection, as it should be directly related to the magnetic flux transfer caused by reconnection. These kinds of studies use cross-polar cap potential Φ_{PC} as a measure for the ionospheric convection (*Reiff et al.*, 1981), and has the following relation to Φ_D and Φ_N:

$$\Phi_{PC} = \frac{1}{2}(\Phi_D + \Phi_N). \tag{2.6}$$

A difficulty with this approach is that both viscous interaction between the solar wind and the magnetosphere and lobe reconnection occurring when IMF $B_Z > 0$ can both excite ionospheric convection, independently of low latitude magnetopause reconnection measured by Φ_D (*Axford and Hines*, 1961). Also, with its dependency on both Φ_D and Φ_N, it is only reliable when the nightside reconnection rate is negligible.

A different method attempting to measure Φ_D almost directly and instantaneously was presented in *Milan et al.* (2012). In this approach, Φ_D is measured based on the expansion rate of the polar cap during periods of no nightside reconnection ($\Phi_N = 0$). With respect to equa-

tion 2.2 we obtain the following relation:

$$\Phi_D = \frac{dF_{PC}}{dt}, \quad \Phi_N = 0. \tag{2.7}$$

Milan et al. (2012) determined the location of the OCB from observations of the poleward boundary of the auroral oval through global auroral imaging. From this method, the following coupling function for the dayside reconnection was derived:

$$\Phi_D = L_{\text{eff}} V_X B_{YZ} \sin^{9/2}\frac{1}{2}\theta, \quad L_{\text{eff}} = 3.8 R_E \left(\frac{V_X}{4\times 10^5 ms^{-1}}\right)^{1/3} \tag{2.8}$$

where L_{eff} is an empirically determined constant of proportionality, such that Φ_D has units of voltage and equals dF_{PC}/dt when $\Phi_N = 0$. Equation 2.8 is the coupling function that will be used as a proxy for Φ_D in the present thesis due to its direct relationship with the opening of flux in the polar cap (Eq. 2.2), which is the main parameter of interest going forward. Some disadvantages to this method are that there is no reliable automated method to measure F_{PC} from auroral images, and it is limited to periods of no nightside reconnection, which limit the scope of possible statistical analyses.

2.7 Nightside Reconnection

In the following section, we discuss the rate at which open magnetic flux is closed in the magnetotail through nightside reconnection. As discussed earlier, dayside reconnection is solely responsible for the opening of magnetic flux in the polar caps and can be estimated through solar wind measurements. Nightside reconnection, however, is solely responsible for the closing of magnetic flux and has a more indirect relation to the IMF. It is often the case that we get a surge in nightside reconnection several tens of minutes after the onset of active dayside reconnection. Such delays arise partly due to the finite magnetic flux propagation speed between the subsolar reconnection region and the reconnection region in the tail. This information propagates with the accompanying solar wind or magnetospheric currents at speeds of a few hundred km s^{-1}. With the magnetotail reconnection region being around 100 to 150 R_E downstream from Earth *Slavin et al.* (1985), the information delay from the subsolar region will be about 20-30 min. Once reconnection in the tail is initiated, the information will then have to propagate back to the ionosphere corresponding to the Alfven speed 1000 km s^{-1}), adding 10 min to the delay. It is also not guaranteed that the opened flux from a period of dayside reconnection will incite nightside reconnection after propagating into the magnetotail. Whether or not nightside reconnection occurs is also dependent on

the magnetotail being sufficiently inflated with magnetic pressure, which can lead to more prolonged periods of weak dayside reconnection without an onset of nightside reconnection. The actual response in the magnetotail to changing interplanetary conditions remains one of the significant areas of uncertainty in the magnetospheric system.

Figure 2.9 presents an idealised example, presented by *Cowley and Lockwood* (1992), illustrating the consequences of such delays in the nightside reconnection. The example starts with a 2-hour interval of steady southward-directed IMF as indicated in the first graph, inducing an equivalent 2-hour period of constant dayside reconnection, increasing the voltage from zero to V volts, illustrated in the second graph. After a 1-hour delay, the onset of equal nightside reconnection occurs with the same constant voltage and period indicated in the third graph. The fourth panel shows the open magnetic flux of the system responding to the periods of dayside and nightside reconnection. In the first hour of the reconnection event, the polar cap experiences a *growth phase* with the size of the polar cap steadily increasing due to the sole presence of dayside reconnection. After an hour, there is a 1-hour *steady state* period of equal dayside and nightside reconnection where the size of the polar cap remains constant. After the dayside reconnection subsides, only the nightside reconnection remains, steadily decreasing the polar cap size back to its initial flux. The final graph shows the polar cap potential response to Φ_D and Φ_N across the central polar cap at ionospheric heights, assuming a circular expanding and contracting polar cap centred on the polar cap. During the period of unbalanced dayside reconnection, Φ_{PC} steadily increases to $V/2$ volts, in accordance with equation 2.6, increasing to V volts during the steady-state period. During the subsequent period of unbalanced nightside reconnection, the potential drops back down to $V/2$, finally returning to zero after all reconnection has ceased. Due to the finite information propagation, there is about a 15 min delay for the polar cap potential to fully respond to the changes in Φ_D and Φ_N.

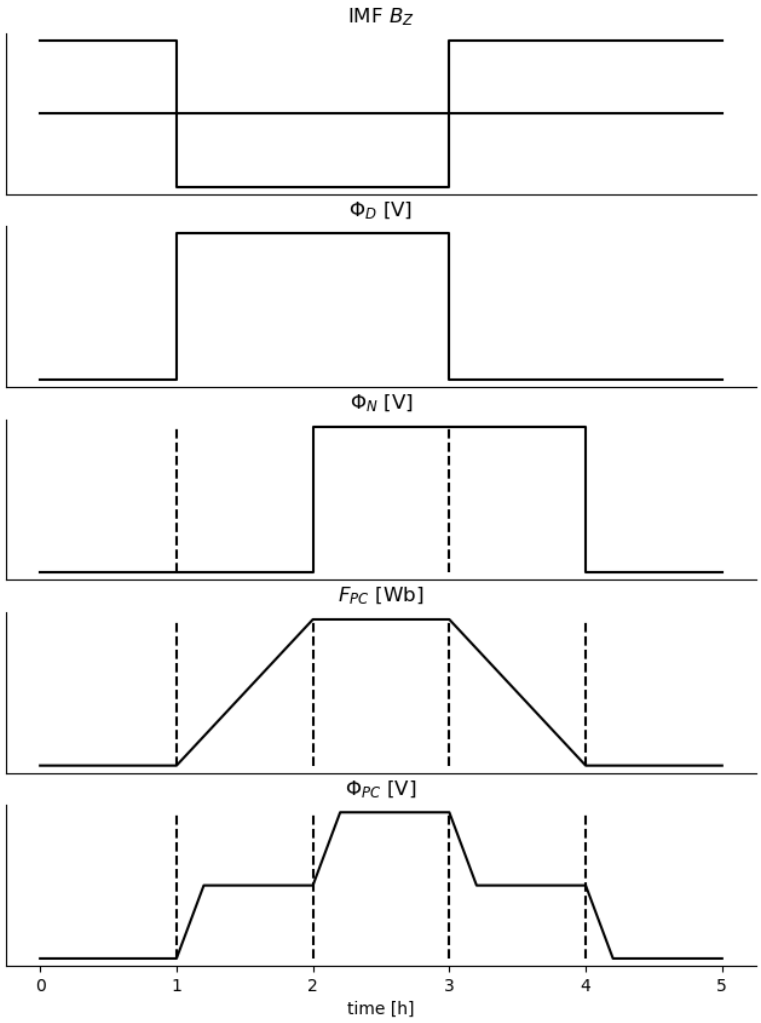

Figure 2.9: Graphs illustrating the response from a 2 hour period of dayside reconnection, followed by a 2 hour period of nightside reconnection after a 1 hour delay. Figure adopted from *Cowley and Lockwood* (1992)

2.7.1 Substorms

While dayside reconnection typically occurs at a steady rate, depending on the orientation of the IMF, nightside reconnection is mainly associated with shorter and more intense bursts of energy release from the magnetotail, known as substorms. What separates substorms from other reconnection events is the increased reconnection rate, leading to a sudden increase in ionospheric activity and brightening auroral arcs, especially in the nightside ionosphere.

In *Milan et al.* (2007), a quantitative study of magnetic substorms was performed, providing some general statistics. On average, the substorm events lasted 70 min, closing 0.3 GWb of

open flux. The average nightside reconnection rate was 85 kV. For comparison, the average dayside reconnection rate was 31 kV for the same periods. On average, a substorm occurred every 2.7 hours at regular F_{PC} values, where the average onset was found at 0.65 GWb. During higher activity periods, around 1 GWb, substorms were expected to initiate every 30 min. There was also no evidence for any lower intensity nightside reconnection occurring outside the substorm periods, indicating that substorms were the primary or only source of nightside reconnection.

2.8 Magnetospheric Current Systems

Figure 2.10 shows an overview of the magnetic field configuration and current systems of the magnetosphere in the northern hemisphere, from the *Milan et al.* (2017) review paper. First, we have a 3D schematic of the geomagnetic field where the closed magnetic field in blue and the open magnetic field in red propagating back into the magnetotail lobes (Fig. 2.10a). In general, currents flow where the geomagnetic field is distorted from a dipolar configuration, leading to spatial gradients in the field where $\nabla \times \mathbf{B} \neq 0$, which implies a current according to Ampère's law. In the second panel, we see the effect of this with the *Chapman-Ferraro currents* on the magnetopause between the weaker magnetic field in the magnetosheath from the stronger field within the magnetosphere *Chapman and Ferraro* (1931). In the equatorial plane of the closed magnetotail, where the magnetic field sharply turns from sunward to antisunward, the *cross-tail current* flows from dawn to dusk, connecting with the Chapman-Ferraro current. Substorm events with strong nightside reconnection will give rise to stronger currents causing the cross-tail current to map into the nightside ionosphere through the *substorm current wedge* (Fig. 2.10b). Finally we have the *region 1* (R1) and *region 2* (R2) *field-aligned currents* (FAC) or *Birkeland currents* heavily associated with the Dungey cycle, expanded upon earlier. In the ionosphere, the Birkeland currents travel along the geomagnetic field, and its magnitude is found to be strongly correlated with both dayside and, likely, nightside reconnection *Coxon et al.* (2014). The region 1 currents in blue travel along the open field lines inside the polar cap, while the region 2 currents in red travel along the closed field lines. Other FACs are also present in the ionosphere, but the R1/R2 currents are the most prominent. The *ring current* in magenta flows westward around the geomagnetic equator is induced from Earth's dipole field with an additional partial ring current excited from the region 2 currents (Fig. 2.10c). *Milan et al.* (2017).

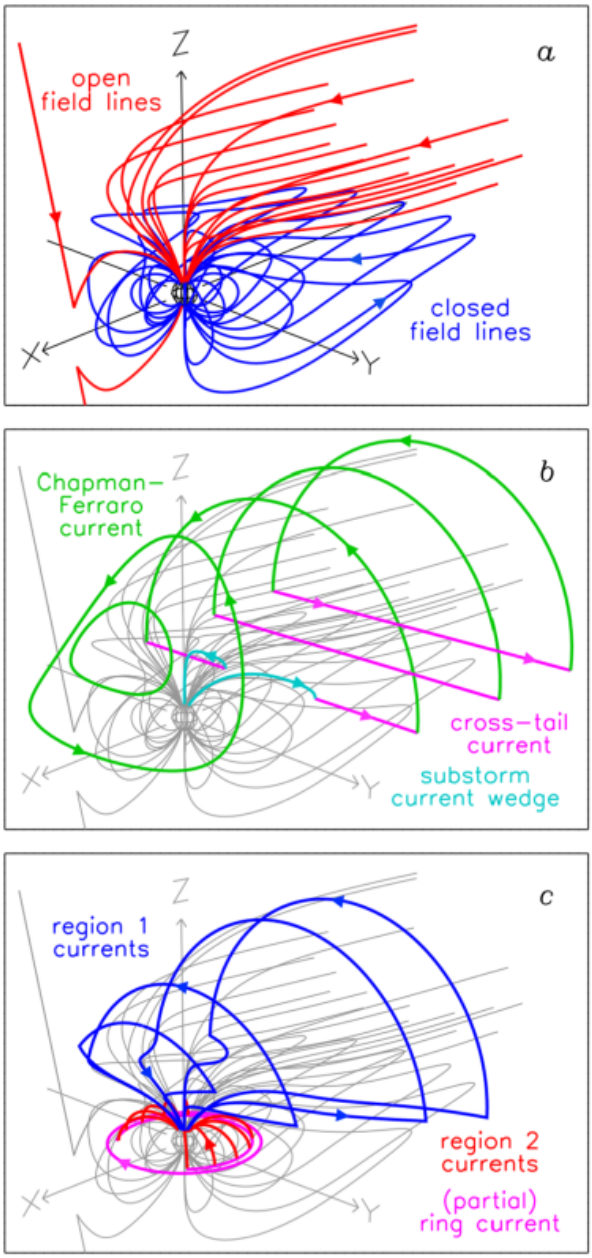

Figure 2.10: Schematic of the magnetic field configuration and current systems of the terrestrial magnetosphere, focusing on the northern hemisphere. **(a)** Open geomagnetic field lines (red) and closed field lines (blue). The open flux comprises field lines newly reconnected with the IMF with the rest of the open field lines accumulated in the tail lobe. **(b)** Chapman-Ferraro currents (green) flowing from dawn to dusk across the dayside magnetopause and from dusk to dawn across the magnetotail magnetosphere. The cross-tail current (magenta) flows from dawn to dusk across the closed tail-magnetosphere connecting with Chapman-Ferraro tail currents at the edges. The substorm current wedge (cyan), present during the substorm expansion phase, diverted from the near-Earth cross-tail current through the nightside ionosphere. **(c)** The region 1 (blue) and region 2 (red) field-aligned current system and the ring current (magenta). The R1, R2 and partial ring current from the convection circuit are associated with the Dungey cycle. The current flows from the magnetopause along R1 into the ionosphere, then along R2 into the partial ring current at the dawnside. The current flows along the partial ring current back into the ionosphere along R2 then out to the magnetopause along R1 on the duskside. Figure from *Milan et al.* (2017)

2.9 Ionospheric Current Systems

Figure 2.11 shows the electrodynamics of the polar ionosphere of the northern hemisphere. Here the ionospheric convection related to the Dungey cycle is presented in black and the OCB line in purple, both discussed earlier. In red and blue are the ionospheric footprints of the Birkeland currents presented in figure 2.10c. The R1/R2 currents are associated with shears in the magnetic field along the OCB, produced by the antisunward convection of open magnetic field lines on the poleward edge of the OCB, and the opposite sunward convection of closed field lines on the equatorward edge of the auroral zone.

The FACs, travelling parallel along the field lines, can be expressed as $J_{\parallel}$, and the horizontal currents in the ionosphere can then be expressed as $\mathbf{J}_{\perp}$. It is common to decompose the horizontal currents into Pederson and Hall currents *Laundal et al.* (2015):

$$\mathbf{J}_{\perp} = \mathbf{J}_H + \mathbf{J}_P \tag{2.9}$$

where $\mathbf{J}_H$ are the Hall currents and $\mathbf{J}_P$ are the Pedersen currents. Pedersen currents are defined to be parallel to the horizontal electric field $\mathbf{E}_{\perp}$, produced by the magnetosphere-ionosphere plasma dynamics *Parker* (1996). The Hall currents are defined to be parallel to $\mathbf{B} \times \mathbf{E}_{\perp}$. These currents are height integrated, providing the surface current density in the ionosphere, ignoring height-based differences in current density. The Pedersen and Hall currents can be further expressed as:

$$\mathbf{J}_P = \Sigma_P \mathbf{E}_{\perp} \tag{2.10}$$

$$\mathbf{J}_H = \Sigma_H \hat{\mathbf{B}} \times \mathbf{E}_{\perp} \tag{2.11}$$

where Σ_P and Σ_H are the Pedersen and Hall conductances, respectively. These conductances are proportional to the electron density of the ionosphere, i.e. the density of charge carriers. In figure 2.11a, the Pedersen currents are represented in green, and the Hall currents are represented in orange. In general, the conductances are enhanced in the auroral zones and the sunward side of the solar terminator, shaded grey in figure 2.11a. The Hall currents, associated with the R1/R2 current system, propagating in the auroral zones are commonly known as the *eastward* and *westward electrojets*. Both currents are flowing from the dayside to the nightside ionosphere. The westward and eastward electrojets are often measured to monitor magnetospheric activity. The magnitude of the electrojets is estimated by measuring the magnetic perturbations at ground level caused by the currents. Measuring the electrojets is possible because of Fukushima's theorem, which states that for all points beneath

the ionosphere, the magnetic fields from FACs and Pedersen currents exactly cancel each other out *Fukushima* (1994). The theorem holds provided that the FACs are perpendicular to the ground and that the ionospheric conductance is spatially constant. Neither of these assumptions holds firmly in the polar ionosphere, but the magnetic perturbations from Hall and Birkeland currents are still generally small compared to the Hall currents.

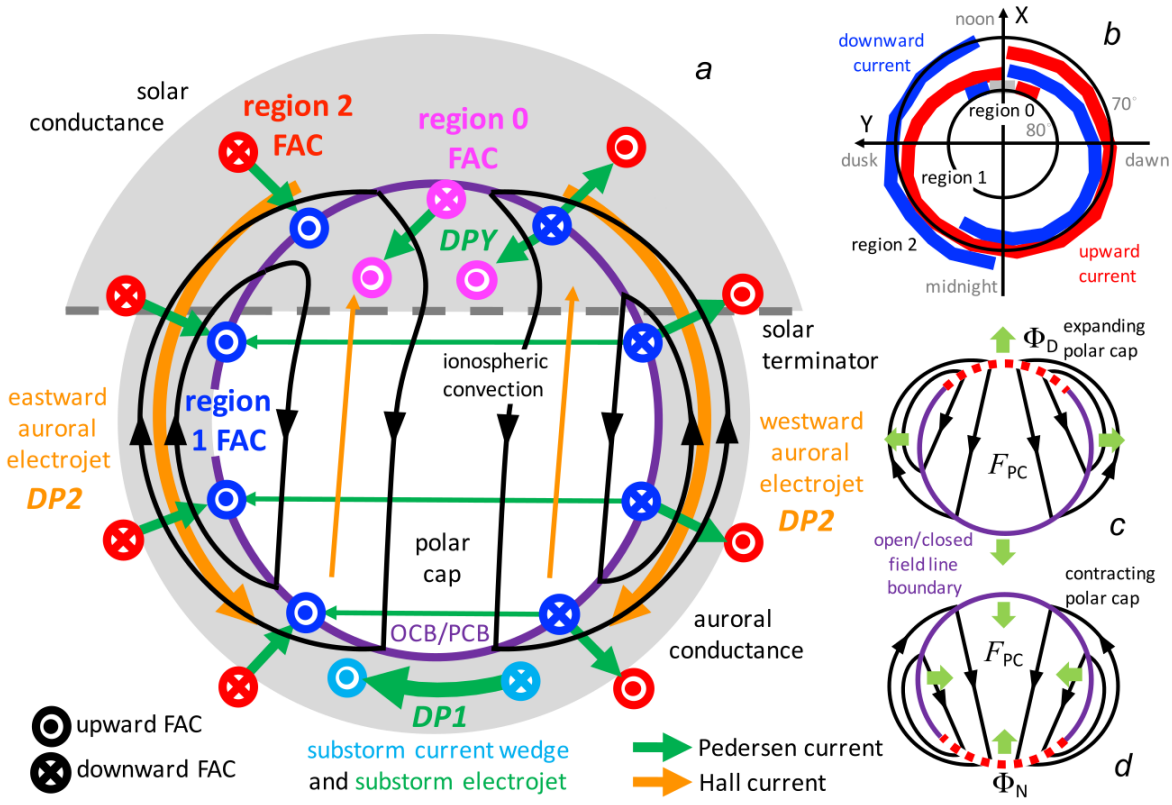

Figure 2.11: The current systems of the northern hemisphere polar ionosphere. **(a)** The purple circle indicates the OCB encircling the polar cap. The back arrows indicate the twin-cell ionospheric convection pattern related to the Dungey cycle. The upward and downward region 1 (blue) Birkeland currents are situated near the poleward edge of the PCB, and region 2 (red) Birkeland current at the equatorward edge of the auroral zone corresponding to the currents in figure 2.10c. Region 0 Birkeland currents (magenta) flow in the cusp throat of the convection pattern, here drawn for IMF $B_y > 0$. The grey shaded areas indicate the auroral zones and the sunward region of the solar terminator, where conductance is enhanced. Pedersen currents (green) flow horizontally between the Birkeland currents and to a lesser degree across the polar cap due to low conductance. Hall current in the auroral zone from the eastward and westward electrojets and weaker currents flowing sunwards in the polar cap, both perpendicular to the respective Pedersen currents. The substorm wedge FACs (cyan) and the interconnecting substorm electrojet (green) are present during the substorm expansion phase. **(b)** Distribution of upward (red) and downward (blue) Birkeland deduced by *Iijima and Potemra* (1976). **(c)** Ionospheric convection pattern with the sole presence of dayside reconnection, expanding the polar cap. The dashed red line of the OCB indicates the area with magnetic field lines mapping to the magnetopause merging gap where reconnection occurs. **(d)** Ionospheric convection pattern with the sole presence of nightside reconnection, contracting the polar cap. *Milan et al.* (2017)

2.10 Timescale Dependence of Solar Wind-Based Regression Models of Ionospheric Electrodynamics

The motivation for this thesis is heavily based on the study performed in *Laundal et al.* (2020). The study quantifies the timescale dependence between geomagnetic indices, dayside and nightside coupling through simple linear regression. Considering a model estimating Φ_N using Φ_D as a variable:

$$\Phi_N^\tau = c(\tau) + d(\tau)\Phi_D^\tau \tag{2.12}$$

where τ denotes the time averaging window or timescale, defined as:

$$y(\tau) = \frac{1}{\tau}\int_{t-\tau}^{t} y(t)\,dt \tag{2.13}$$

We know that Φ_D and Φ_N are poorly correlated over short timescales as it can take several hours after a dayside reconnection event, for nightside reconnection to occur, and often at different rates. This means that for small timescales, τ, $d(\tau)$ in Equation 2.12 is also small. For the limit $\tau \to \infty$, we get $c(\infty) = 0$ and $d(\infty) = 1$ since dayside and nightside reconnection are equal for longer timescales (Eq. 2.3).

In *Laundal et al.* (2020), a set of geomagnetic indices: *AL*, *AU*, *PCN*, and *ASY-H*, are used to build a model for estimating the nightside reconnection rate. The *AL* and *AU* indices measure the westward and eastward electrojets, respectively. The *PCN* and *ASY-H* indices, as well as a variant of the *AL* index, the *SML* index, will later be explained in more detail. The geomagnetic indices can be written on the following functional form:

$$y = \alpha + \beta\Phi_{PC} \tag{2.14}$$

assuming each index is a linear function of dayside and nightside reconnection rates. y represents any of the indices used in the study and Φ_{PC} represents the cross polar cap potential (Eq. 2.6). α and β are proportionality coefficients. Since Φ_{PC} is not known, we can use Equations 2.12 and 2.6 to rewrite Equation 2.14 to a timescale dependent version that only depends on Φ_D^τ:

$$\begin{aligned} y^\tau &= \alpha + \beta\Phi_{PC}^\tau = \alpha + \frac{1}{2}\beta(\Phi_D^\tau + c(\tau) + d(\tau)\Phi_D^\tau), \\ y^\tau &= a(\tau) + b(\tau)\Phi_D^\tau, \end{aligned} \tag{2.15}$$

where

$$a(\tau) = \alpha + \frac{1}{2}\beta c(\tau) \tag{2.16}$$

$$b(\tau) = \frac{1}{2}\beta(1 + d(\tau)). \tag{2.17}$$

Next, Equation 2.15 is used to estimate $a(\tau)$ and $b(\tau)$, for multiple timescales and indices, through simple linear regression. Figure 2.12 presents the Pearson correlations coefficient, r^2, between the regression model and the data for the respective indices. This correlation gives the fraction of the data which the model explains. The horizontal axis represents the timescale, in hours, of the averaging of the variables. We see all indices experience an increasing correlation with their respective models for increasing timescales. The improving correlation is expected since the indices are assumed to depend on both Φ_D and Φ_N (Eq. 2.14), but only Φ_D is used in the regression model since Φ_{PC} is not known. The poor correlation at shorter timescales is because of Φ_D and Φ_N being poorly correlated at shorter timescales and equal at longer timescales.

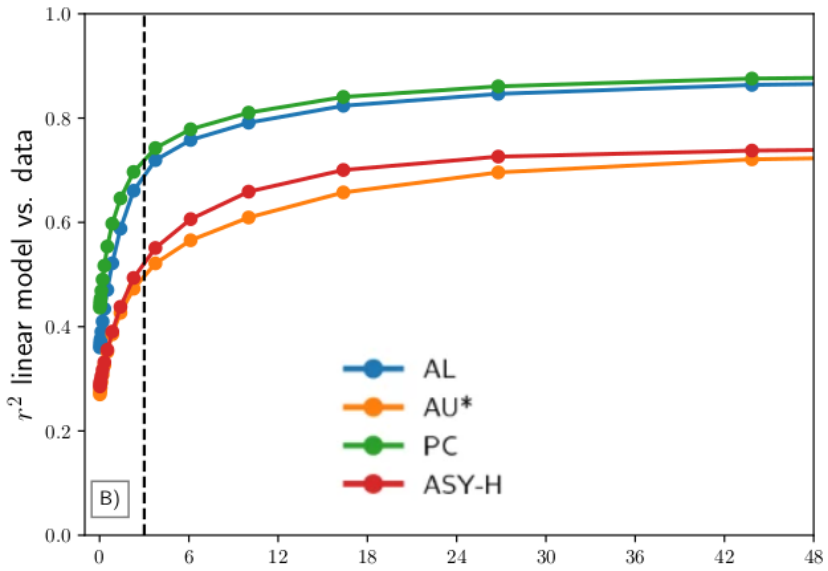

Figure 2.12: *Laundal et al.* (2020)

Using the previous equations, we can now derive an equation for nightside reconnection which is independent of timescales. In the limit $\tau \to \infty$, Equations 2.16 and 2.17 reduces to $a(\infty) = \alpha$ and $b(\infty) = \beta$, respectively, since $c(\infty) = 0$ and $d(\infty) = 1$. By solving Equation 2.6 and replacing Φ_{PC} with Equation 2.14, we get:

$$\Phi_N = 2\frac{y - \alpha}{\beta} - \Phi_D = 2\frac{y - a(\infty)}{b(\infty)} - \Phi_D. \tag{2.18}$$

$a(\infty)$ and $b(\infty)$ for each index can be estimated by averaging the data over several days. Figure 2.13 shows a time series of Φ_N, calculated from Equation 2.18. The thin blue lines show the Φ_N estimated from the individual indices, and the thick blue line shows the average of the four estimates. The green line shows the Φ_D estimate for comparison. The vertical lines denote the onset time for two substorms observed in global images of the aurora, produced by the *Far Ultra Violet* (FUV) imager on the IMAGE satellite (*Frey et al.*, 2004).

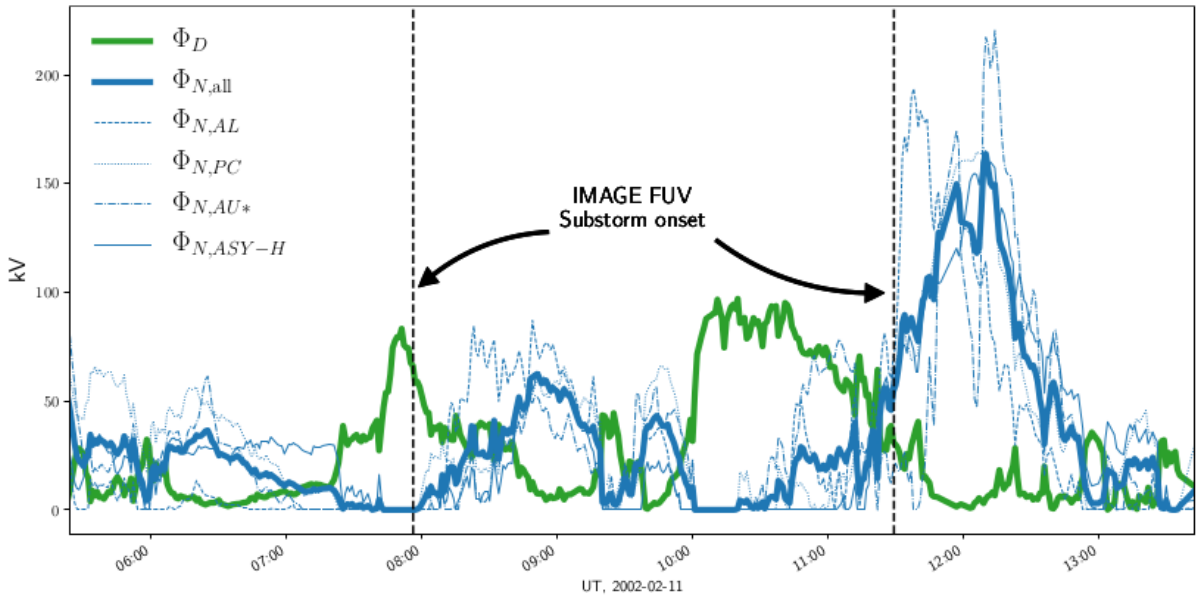

Figure 2.13: *Laundal et al.* (2020)

2.11 Geomagnetic Indices

Considering the ECPC (eq. 2.2), equation 2.8 will be used as a direct measurement for Φ_D. However, there is no consistent method to measure the nightside reconnection rate Φ_N directly. Instead, it could be possible to use geomagnetic indices to estimate Φ_N (*Laundal et al.*, 2020). These indices are measures of geomagnetic activity in various magnetospheric systems. Next, we will go through the geomagnetic indices expected to be correlated with nightside reconnection.

2.11.1 The *SML* Index

The *SML index* is a geomagnetic index from the *SuperMAG* database. SuperMAG is a worldwide collaboration of organisations and national agencies that currently provide standardised data from more than 300 ground-based magnetometers (*Gjerloev*, 2012). Some of these stations around the northern hemisphere polar cap are illustrated in figure 2.14. SuperMAG

utilises three-dimensional vector measurements of the magnetic field obtained from these ground-based magnetometers. The *SML* index measures the maximum westward auroral electrojet strength using data from magnetometer stations between 40° and 80° magnetic north *Newell and Gjerloev* (2011). Specifically, the *SML* index is given by the minimum measured value of the H component by the ground magnetometer (minimum being the value of largest magnitude as the *SML* index is almost always given in a negative value). The H component represents the magnitude of the horizontal magnetic field perturbations at ground level. This component comes from the (H, D, Z) coordinate system where H is the horizontal perturbation of the magnetic field, D is the declination in degrees between geographic north and the horizontal direction of the magnetic field. Z is the vertical component of the magnetic field, positive towards Earth's centre.

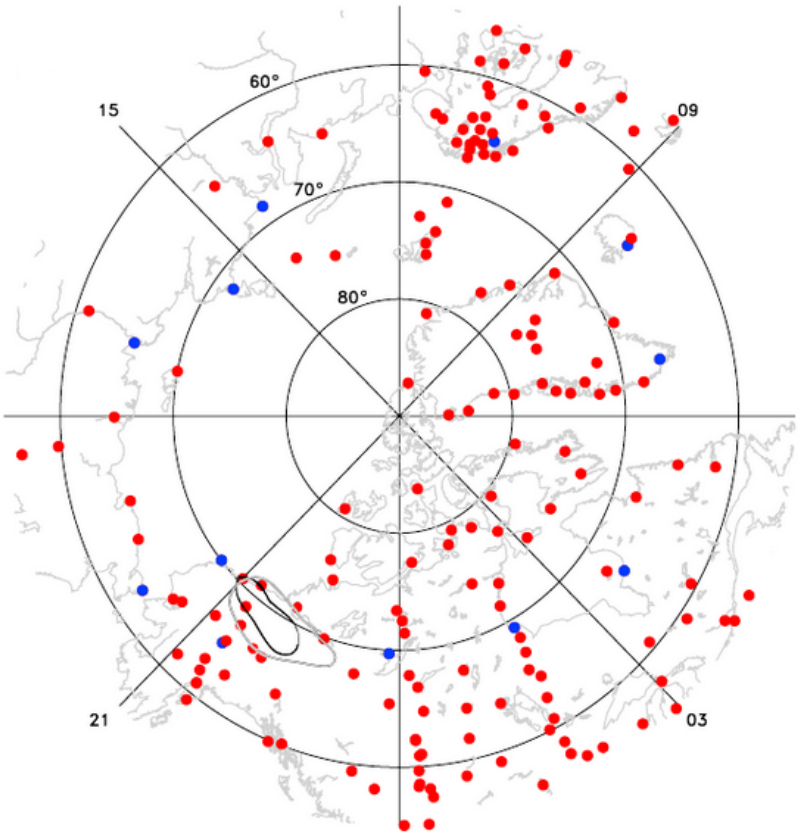

Figure 2.14: Geomagnetic stations used to measure the AL index (blue) and stations used to measure the SML index (red + blue). This illustration only shows the active stations from 30 January 0841 UT, as there are likely more active stations in present time. *Newell and Gjerloev* (2011)

Similarly to the *SML* index, there is also an *SMU* index, which measures the eastward electrojet. The reason we are using the *SML* index in favour of the *SMU* index is that the *SML* index also pick up perturbations caused by the substorm current wedge, which is present during active nightside reconnection. For this reason, the *SML* index is expected to be much

more correlated with nightside reconnection than *SMU*.

The *AL* and *AU* indices used in *Laundal et al.* (2020) are very similar to the *SML* and *SMU* indices. They measure the westward and eastward electrojets, respectively, but only uses the 12 stations marked in blue in Figure 2.14.

In addition to *SML*, the *SML-LT* index will also be used. *SML-LT* is a regional version of the *SML* index where the *SML* index is measured separately for each hour period of *MLT Newell and Gjerloev* (2014). In this thesis, *SML-LT* will refer to the minimum *SML* value between 21 MLT and 03 MLT, the six-hour period centred around midnight. This is in an attempt to minimise the impact from dayside reconnection on the *SML* index, so it may better describe ongoing nightside reconnection. It is found that the *SML-LT* is better correlated with the change in open flux dF_{PC}/dt which we will come back to in a later section.

2.11.2 The *PC* Index

The *Polar Cap (PC) indices*, *PCN* and *PCS* for the northern and southern polar cap respectively, was originally introduced by *Troshichev and Andrezen* (1985). It is based on data from a single near pole station in each hemisphere, Qaanaaq (MLAT ~ 85°) and Vostok (MLAT ~ −83°). The purpose of these indices is to estimate the intensity of the sunward Hall currents in the polar cap by measuring the magnetic field variations induced by the current. This Hall current is associated with the antisunward convection in the polar caps. From this, the PC index should estimate the loading of the magnetosphere associated with the dayside coupling. Similarly, the *PC* index can respond to nightside coupling in the same order as with dayside coupling (*Huang*, 2005). (*Kauristie et al.*, 2017)

2.11.3 The *ASY-H* Index

The *ASY-H* index is part of the mid-latitude geomagnetic indices, *SYM-H*, *ASY-H*, *SYM-D* and *ASY-D* (*Iyemori and Toh*, 2010). These indices aim to describe variations of the equatorial magnetospheric ring current, earlier presented in Figure 2.10c (magenta). Specifically, they measure disturbances in the magnetic field caused by the ring current. There are 11 stations in total used to measure the disturbances, shown as the black circles in Figure 2.15. Only six of the stations are used for deriving the index, some stations being favoured based on the availability and condition of the data. The stations interconnected with the black lines in Figure 2.15 are the ones who can replace each other. The stations are placed at mid-latitudes to avoid disturbances caused by the auroral and equatorial electrojets.

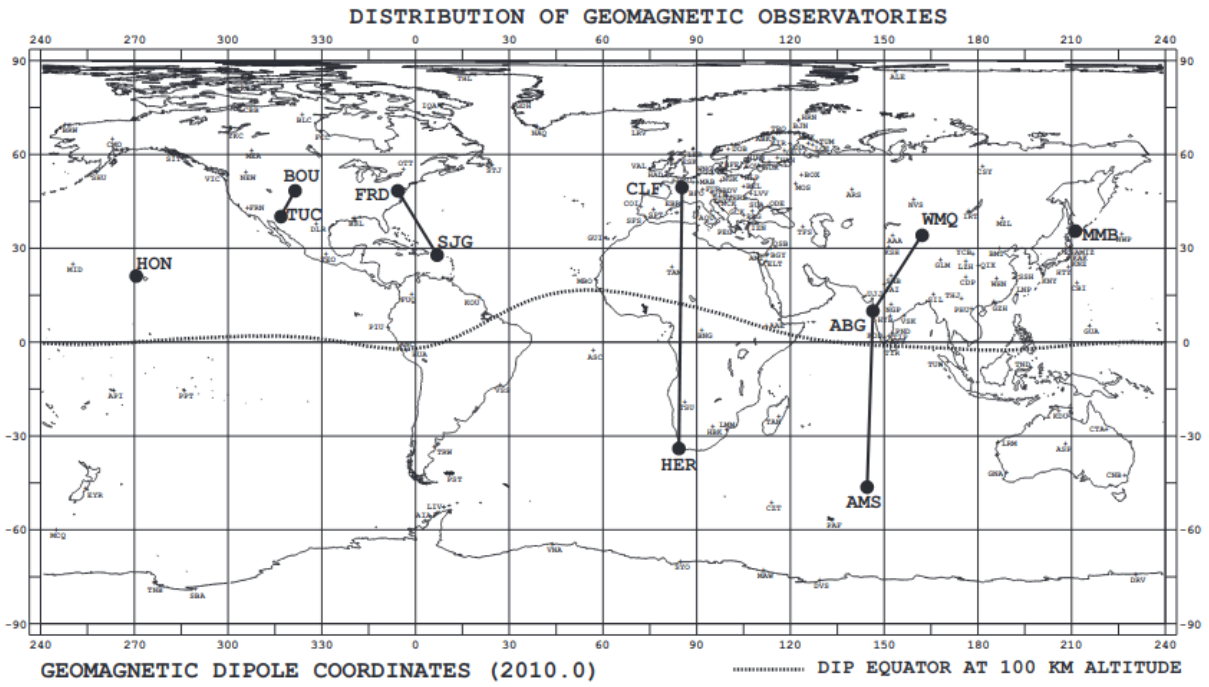

Figure 2.15: (*Iyemori and Toh*, 2010)

The indices describe the geomagnetic disturbance fields with a longitudinally asymmetric (*ASY*) and symmetric (*SYM*) disturbance index, both derived with H and D components. Although the geomagnetic field is approximately like a dipole field, close to the surface, the direction of the magnetic field at each observatory is generally different from the northward dipole pole direction. The local geomagnetic field is then decomposed into a H component along the dipole north direction and a D component, perpendicular along the east-west direction.

The *SYM-H* index is calculated by taking the average of the disturbance H component at each of the six stations. This H component is found at each station by subtracting the local quiet-time magnetic field and normalising it based on the latitude of the respective stations. The asymmetric component at each station is then obtained by subtracting the *SYM-H* index from each disturbance field, such that the deviation from the average is then found at each station. The *ASY-H* index is defined as the difference between the minimum and maximum deviation from the *SYM-H* index.

The reason why we are using the *ASY-H* index is that it is expected to be the best correlated with magnetospheric reconnection. *ASY-H* is the index that should be the most perturbed by the partial ring current induced by the Birkeland currents, which are stronger during magnetosphere coupling.

Chapter 3

Method

3.1 Determining the Open Magnetic Flux using AMPERE

3.1.1 Description of the AMPERE Data Set

The active magnetosphere and planetary electrodynamics experiment (AMPERE) (*Anderson et al.*, 2000, 2002, 2008; *Waters et al.*, 2001) provide estimates of the Birkeland currents or field-aligned currents (FACs) in the Northern and Southern hemisphere, using magnetometer observations from the Iridium constellation. The Iridium satellite constellation consists of about 90 commercial satellites, distributed over six orbital planes at 780 km altitude, providing global satellite telephone and data services (*Waters et al.*, 2020). Each satellite carries a magnetometer as part of its attitude control system. The magnetic field perturbation data gathered from these satellites allows one to estimate the distribution of radial current densities or Birkeland currents.

Magnetic field measurements from the Iridium magnetometers have been available for space physics research since 1999, provided initially at a sample period of 200 s. In 2009, the AMPERE project was developed, which enhanced the delivery and processing of the Iridium magnetometer data, summarised in *Anderson et al.* (2014), reducing the sampling period from 200 s to 20 s. With the improved sampling rate, the limiting factor becomes the time taken for the satellites to reach full latitude coverage from one instance to another, about 9 min. From this limitation, the AMPERE field perturbation data are fitted from a 10 min data collection window.

From the magnetic field perturbation maps, current density maps of the Birkeland currents can be estimated as described by *Waters et al.* (2001). With the extensive coverage of the AMPERE magnetic field data, the curl of the magnetic field perturbations, $\Delta\mathbf{B}$, is estimated

through a spherical harmonic fitting technique. The current densities, **J**, are then estimated by applying Ampere's law:

$$\nabla \times \Delta \mathbf{B} = \mu_0 \mathbf{J} \tag{3.1}$$

An example current density map is presented in figure 3.1, where the red regions indicate upward currents and the blue regions indicate downward currents. The AMPERE current maps are estimated every 2 min from a 10 min rolling data gathering window. However, two current density maps 2 min apart will be based on mostly the same data and highly correlated due to the 10 min data sampling window (*Waters et al.*, 2020).

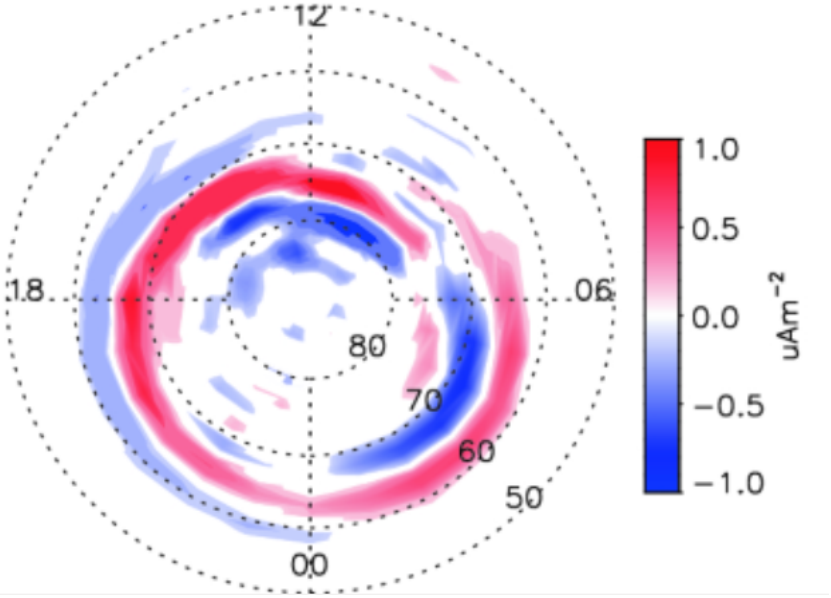

Figure 3.1: Example AMPERE current density map for 0520-0530 UT, 24 August 2010 *Waters et al.* (2020)

3.1.2 Determining the Region 1 / Region 2 Current Boundary

In *Milan et al.* (2015), a method of estimating the size of the polar cap, using AMPERE current maps, is presented. Each AMPERE map covers the polar region poleward of 40° geomagnetic latitude. The current maps are provided on a 24 × 50 polar grid, one grid cell for each MLT hour (equivalent to 15° longitude) and each degree of co-latitude. Figure 3.2a presents an example of such a current map where the grid cells are visible. The signatures of the region 1 and 2 (R1/R2) current system are also visible, similar to Figure 2.11b.

The R1/R2 current regions are assumed to have a circular shape, centred on a point, $\Lambda_0 = (x_0, y_0)$, where y_0 lies between 0° and 5° anti-sunward co-latitude, and x_0 between ±2° along the dawn-dusk meridian. In Figure 3.2a, Λ_0 is estimated at the point (0°, 3°), represented by

the cross. For each radius, Λ, centred on (x_0, y_0), the mean current density, j, is found at 48 equally spaced points around the circumference of each circle in the range $0° \leq \Lambda \leq 50°$. The sum of the current densities, Σj, around each circle is found after multiplying the dusk sector currents (12-24 MLT) by -1, such that the regions 1 currents are positive, and the region 2 currents are negative in both the dawn and dusk sector. The summed current density, Σj, as a function of radius Λ is presented in Figure 3.2b.

The positive and negative peak values of Σj are identified as region 1 and region 2 currents, respectively. The latitude where $\Sigma j = 0$ between these peaks is identified as boundary between the R1/R2 currents, Λ_{fit}, presented by the black circle in Figure 3.2a. This process is repeated for several different Λ_0 and Λ_{fit} until the combination with the greatest R1/R2 peak-to-peak difference is used as the final fit. The fitted circle radii in the northern and southern hemispheres, for 2010 to 2016, at a 2 min cadence, can be downloaded from the following repository; https://doi.org/10.25392/leicester.data.11294861.v1.

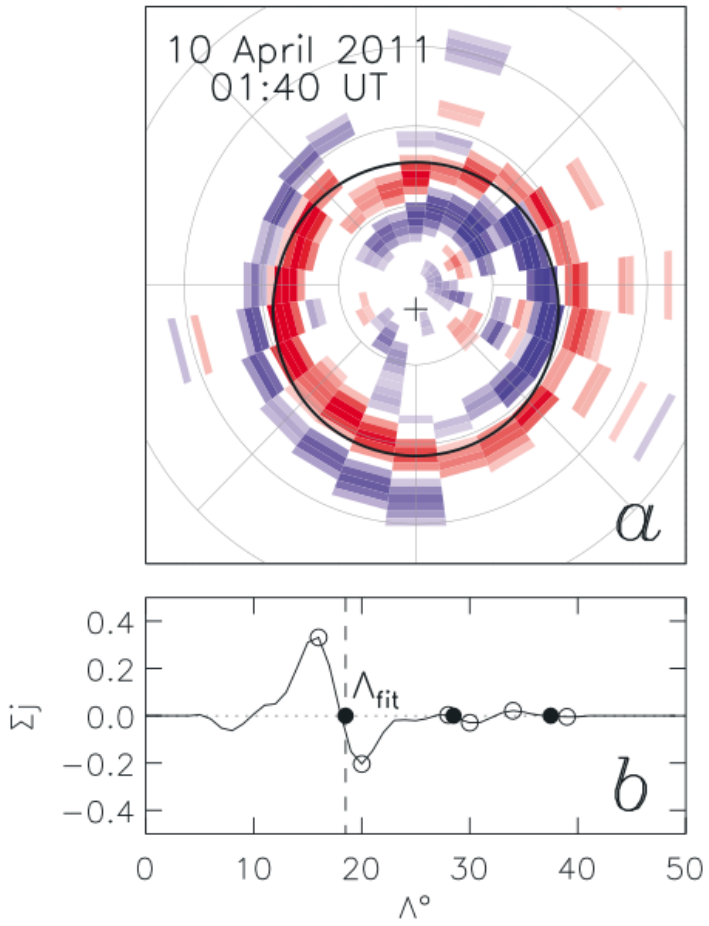

Figure 3.2: **(a)** AMPERE current density map converted into a 24 × 50 grid for 0140 UT, 10 April 2011. The black circle represents the R1/R2 boundary fit, and the cross represents the centre of the circle fit. **(b)** The circle integrated current density plotted as a function of radius, Λ. The open circles represent local positive and negative peaks, with the solid circles representing the zero-crossings between the peaks. The zero-crossing with the largest peak-to-peak magnitude is identified as the R1/R2 boundary, Λ_{fit}. Figure from *Milan et al.* (2015)

3.1.3 Creating an AMPERE OCB Proxy

The R1/R2 boundary is closely related to but not necessarily equal to the open-closed field line boundary (OCB), which we are trying to identify. Generally, the OCB tends to lie a few degrees poleward of the R1/R2 current boundary, depending on the MLT. To account for the OCB displacement, a correction term, *K*, is applied to the AMPERE R1/R2 boundary, based on a process outlined in *Burrell et al.* (2020). The OCB correction is found by comparing the median AMPERE R1/R2 boundary to the OCB referred from the Defense Meteorological Satellite Program Special Sensor J (DMSP SSJ). The DMSP is a satellite system, where the SSJ measures the electron energy flux from ionospheric particle precipitation (*Redmon et al.* (2017)). Implementing the technique described in *Kilcommons et al.* (2017), a set of OCBs were obtained by estimating the poleward boundary of auroral ovals, identified from the

DMSP SSJ electron flux data. A generalised ellipse function (Eq. 3.2) is used to fit the offset between the DMSP SSJ OCBs and the AMPERE R1/R2 boundaries:

$$K(\lambda) = \frac{a(1-e^2)}{1+e\cos(\lambda-\tau)} \tag{3.2}$$

where λ is the MLT in radians, a is the semi-major axis, e is the eccentricity of the ellipse, and τ is the offset of the ellipse's axes in radians. The results of the OCB fitting process is presented in Figure 3.3, taken from Figure 3 in *Burrell et al.* (2020). In Figure 3.3, the dashed line represents the median AMPERE R1/R2 boundary. The latitude difference, $\Delta\phi$, between the median DMSP SSJ OCB for each MLT hour is represented by the blue dots with the respective error bars. The elliptical boundary correction (black line) is fitted onto the $\Delta\phi$ series, and the estimated parameters of Equation 3.2 are shown above the plot. The OCB correction is slightly over 3 degrees poleward of the R1/R2 boundary on average. The grey histogram in the background shows the number of DMSP SSJ OCB observations in each MLT bin.

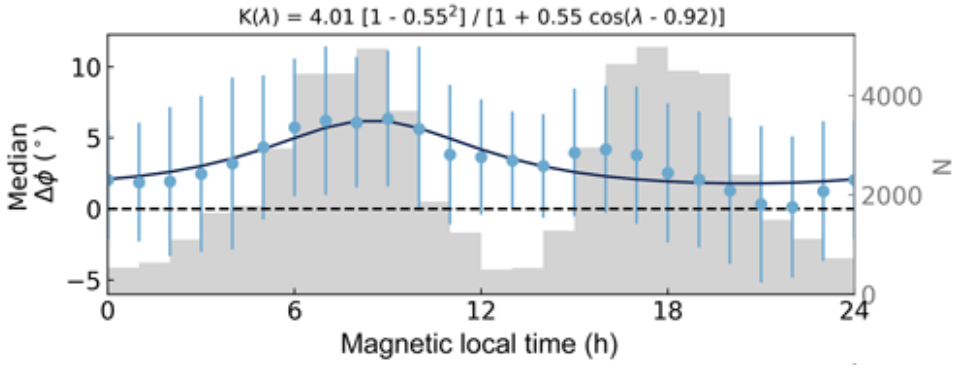

Figure 3.3: Elliptical boundary correction (black line), K, fitted to the median $\Delta\phi$ (blue dots) with respective error bars in each MLT bin. The grey histogram presents the number of OCB boundary counts in each MLT bin. *Burrell et al.* (2020)

3.1.4 Estimating the Open Flux within the AMPERE OCB

Now that the AMPERE OCB can be identified finding the total magnetic field within the OCB is necessary to estimate the open flux (Eq. 2.1). The method described in *Ohma et al.* (2018) will be applied to estimate the magnetic field. The OCB estimates are projected onto an equal area grid map with a resolution of 1° in the latitudinal direction. The final grid map consists of a total of 3720 grid cells in the region above 60° MLAT. The magnetic flux within each grid cell is estimated by integrating Equation 4.15 in *Richmond* (1995) with the magnetic field within the cells represented by the International Geomagnetic Reference Field (IGRF) (*Thébault et al.* (2015)). The total open magnetic flux is then found by the sum of the

magnetic flux of all grid cells having their central location within the OCB.

3.1.5 The Open Flux Data Set

The final AMPERE data set with which we are working contains the (x_0, y_0) coordinates and the radius of each AMPERE R1/R2 boundary fit, the estimated open magnetic flux for each map, and a quality parameter estimated for each fit which we will come back to later. Figure 3.4 shows the histogram of the northern hemisphere open flux provided by the AMPERE data set. The histogram shows the complete open flux data from 2010 to 2017 at a 2min cadence, totalling about 1.5 million values. In reality, the open flux is expected to assume an even distribution, but we see the values are distributed around several discrete values. The discrete distribution is due to the radius, Λ, being fitted with a 1° resolution. However, based on this assumption, we should expect only to see a single spike representing each discrete radius. At the same time, in practice, we have a small distribution of values around these peaks. There are several reasons attributed to these variations. Different values of x_0 and y_0 leads to differences in open flux due to spatial variations in the IGRF for a fixed radius. Temporal variations in the IGRF can also lead to different open flux values while holding (x_0, y_0) constant. The OCB correction applied to the R1/R2 boundary fits has more significant effects on the open flux for a large radius versus a small radius.

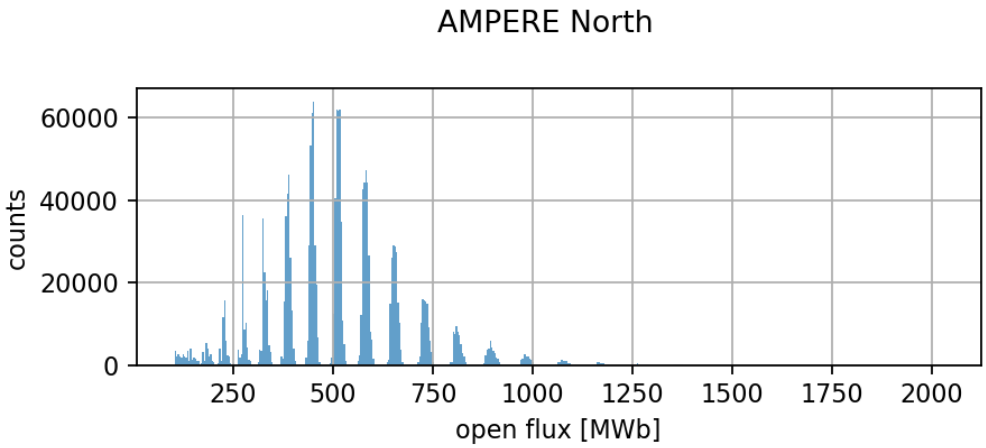

Figure 3.4: Histogram of entire AMPERE data set from 2010 to 2017 for the northern hemisphere.

3.2 Curve Fitting the AMPERE Data

The upper plot of figure 3.5 shows the AMPERE North open flux values plotted for a full day, 4 March 2010. The lower plot shows the direct derivative of the AMPERE open flux. These plots visualise the staggered nature of the AMPERE data. Rather than having a smooth

curve, the open flux values are jumping between different bins. As shown in the second plot, this indicates the open flux is increasing or decreasing through short bursts of flux transfers reaching up to several hundred MWb/s in magnitude. These magnitudes can not be the case as the opening of flux is directly driven by the flux transfer rate of the dayside reconnection, which never reaches these magnitudes.

The AMPERE data set include open flux values from both the northern and the southern hemisphere. We have chosen to concentrate on data from the northern hemisphere instead of combining them for several reasons. There are known to be systematic differences between the northern and southern hemispheres in which combining them can affect the average in a non-transparent way. When using the quality constraint, which will be elaborated upon later, one could swap between north and south depending on whoever has a better fit quality, which could lead to changes in open flux values that are not real. We use the northern hemisphere in favour of the southern hemisphere because it should be closely related to geomagnetic indices like the SML index, which is also measured in the northern hemisphere. There is also more data coverage in the northern hemisphere. Additionally, the AMPERE data from the northern hemisphere is found to be more reliable in general (*Anderson et al.*, 2017).

From figure 3.4 & 3.5 we see that the raw data from the AMPERE set does not make for a very precise representation of the realistic open flux. Finding the derivative of the open flux (dF_{PC}/dt) can be very inaccurate. Different univariate regression analyses will be applied to the AMPERE data to circumvent these issues in an attempt to find a more accurate and workable representation of open magnetic flux.

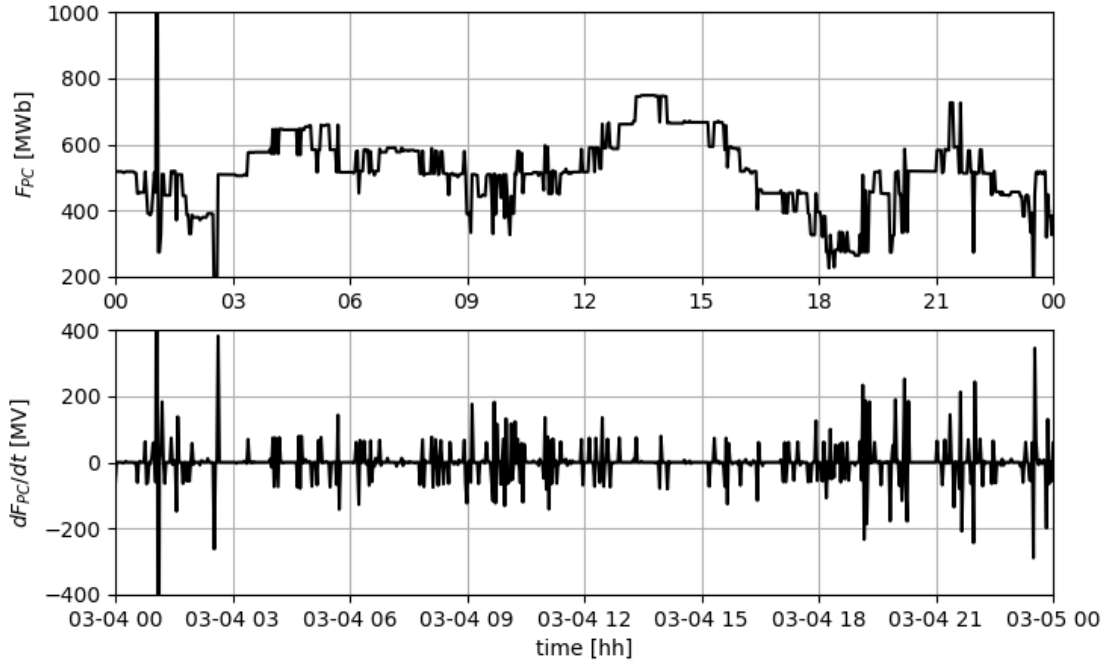

Figure 3.5: The upper plot shows the AMPERE open flux series of the northern hemisphere for 04 March 2010. The lower plot shows the same open flux series differentiated.

3.2.1 Polynomial Regression Representation of AMPERE Open Flux

The first type of analysis performed on the AMPERE data is a polynomial regression applied to a rolling window. Assuming the rolling window has a length of 30 min, the fit function applies a 2nd-degree polynomial regression on a 30 min window around the value for each AMPERE value. From this regression, the vector containing the regression coefficients at the centre of the window is returned to the corresponding timestamp. The polynomial regression will, in this thesis, be performed with several different lengths on the rolling window as these can yield different results, and it is not apparent what an optimal time window would be. Having a shorter time window offers a better resolution of the data but is more sensitive to noise prevalent in the AMPERE data.

On the other hand, a longer time window is less sensitive to noise but may also show a lower variation of the open flux than what we would see in reality. The relationship between different geomagnetic processes is also expected to depend on different timescales, where matching these timescales may yield better results. The upper plot in figure 3.6 shows the polynomial interpolation performed on the AMPERE North data for three different window sizes, 30 minutes (orange), 60 minutes (green) and 90 minutes (red). The lower plot shows their respective derivatives. The plots indicate how, for larger time windows, the fitted curve be-

comes progressively smoother, while for smaller windows, more of the changes in the AMPERE data is picked up.

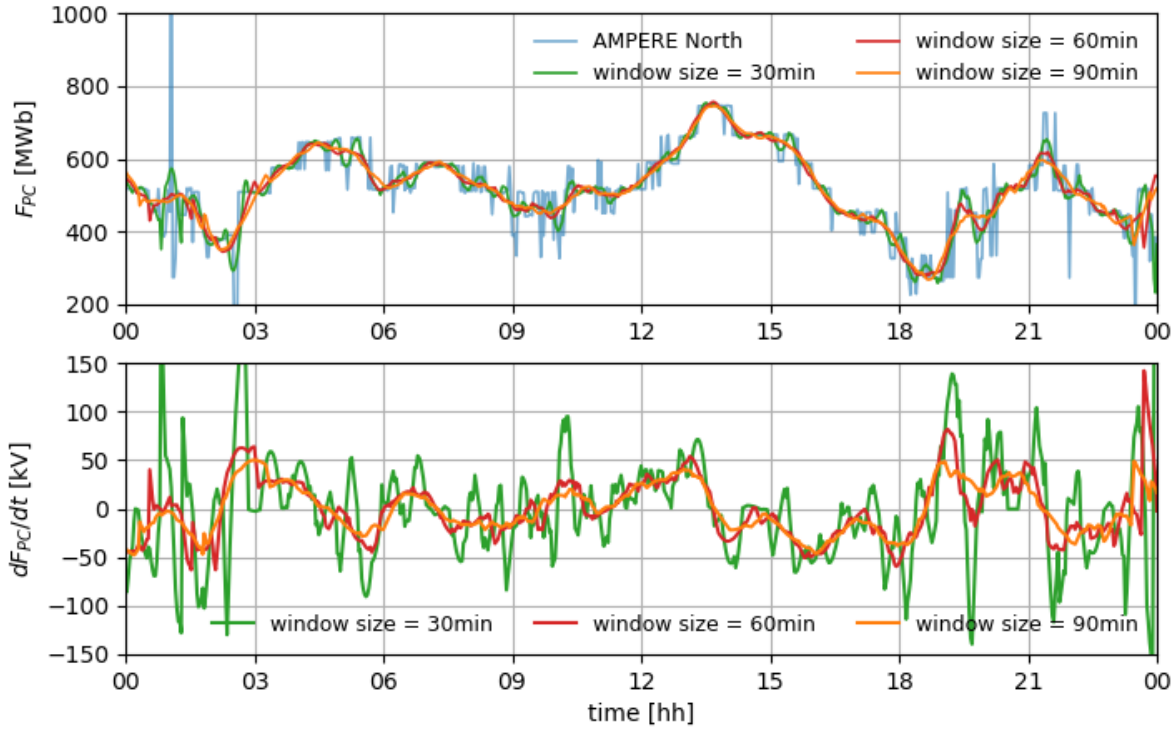

Figure 3.6: Plots of the open flux (upper) and change in open flux (lower) of the OCB for a full day, 4 March 2010. The upper graph show the AMPERE North fit (blue) plotted together with its polynomial regressions for rolling windows of 30min (orange), 60min (green) and 90min(red). The lower graph shows the derivatives of the respective polynomial fits.

3.2.2 Spline Representation of AMPERE Open Flux

The second type of analysis performed on the data set is a cubic spline interpolation. This method breaks the data up in a series of equally spaced knots and performs a piecewise 3rd degree polynomial fit between each knot. The preference for performing a spline interpolation over a polynomial interpolation is the possible reduction of the interpolation error and avoiding Runge's phenomenon, in which oscillation can occur between points when interpolating using high degree polynomials. Similarly to the polynomial interpolation, the timescale dependence of the spline interpolation can be changed by changing the space between each knot. Figure 3.7 shows three spline interpolations performed in a similar fashion to the polynomial interpolations in figure 3.6. Both plots in both figures are from the same day, 4 March 2010. A striking difference between the spline fits and the polynomial fits is that the spline fits are a lot smoother. The oscillation of the spline fit is limited to a 3rd de-

gree polynomial between each knot. Increasing the space between each knot will therefore reduce the number of oscillations in the fit. This also reduces the amount of variation captured by the spline method since the knots and the fit window are fixed. On the other hand, the polynomial fit makes a separate fit for each value in the AMPERE data and can therefore oscillate with the same 2min cadence as AMPERE. However, the oscillations are damped by increasing the window size.

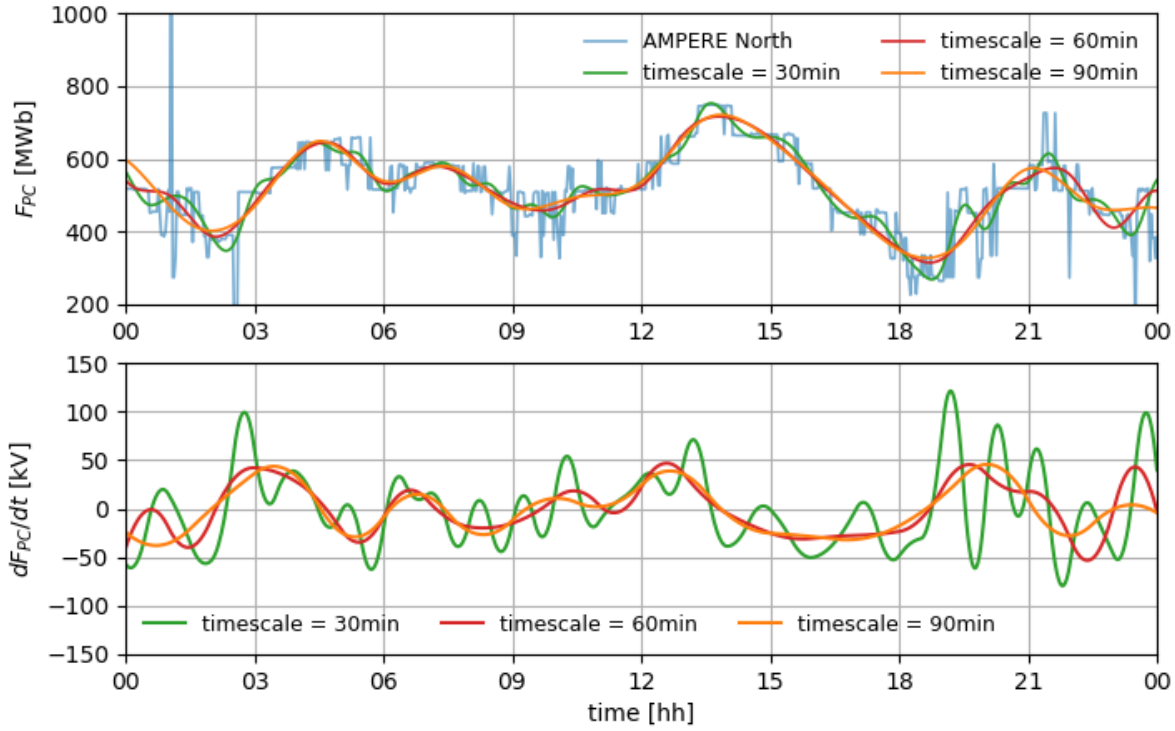

Figure 3.7: Plots of the open flux (upper) and change in open flux (lower) of the OCB for a full day, 4 March 2010. The upper graph show the AMPERE North fit (blue) plotted together with its spline interpolations for knot spacing of 30min (orange), 60min (green) and 90min(red). The lower graph shows the derivatives of the respective spline fits.

3.3 Concerning the AMPERE Quality Parameter

In addition to the open flux data, the AMPERE data set also comes with a quality parameter. The quality parameter is automatically calculated for each R1/R2 boundary fit, described in *Milan et al.* (2015). The fit quality is estimated by calculating the average peak-to-peak current density between the R1/R2 currents, given in units μA m^{-1}, meaning the quality parameter is proportional to the R1/R2 Birkeland current strength (Fig. 3.2b). The quality parameter is a general estimate for how accurately the circle fit predicts the R1/R2 boundary. It

is more challenging to identify the R1/R2 boundary when the Birkeland currents are weak. In the *Milan et al.* (2015) study, for example, fits of quality less than 0.15 were considered unreliable and ended up being discarded. The quality parameter will also be used in the present study to filter out unreliable AMPERE data. The second panel in Figure 3.8 shows the quality parameter plotted for the same time interval we have looked at earlier. The final panel illustrates the dayside reconnection, Φ_D, calculated with Equation 2.8 and the *SML* index from the SuperMAG database. As indicated from these panels, a possible issue with filtering out low-quality data is that we create a bias towards higher activity periods, causing our model to represent lower activity periods poorly. Filtering data based on the quality parameter will be discussed in the next section concerning the selection of open flux data.

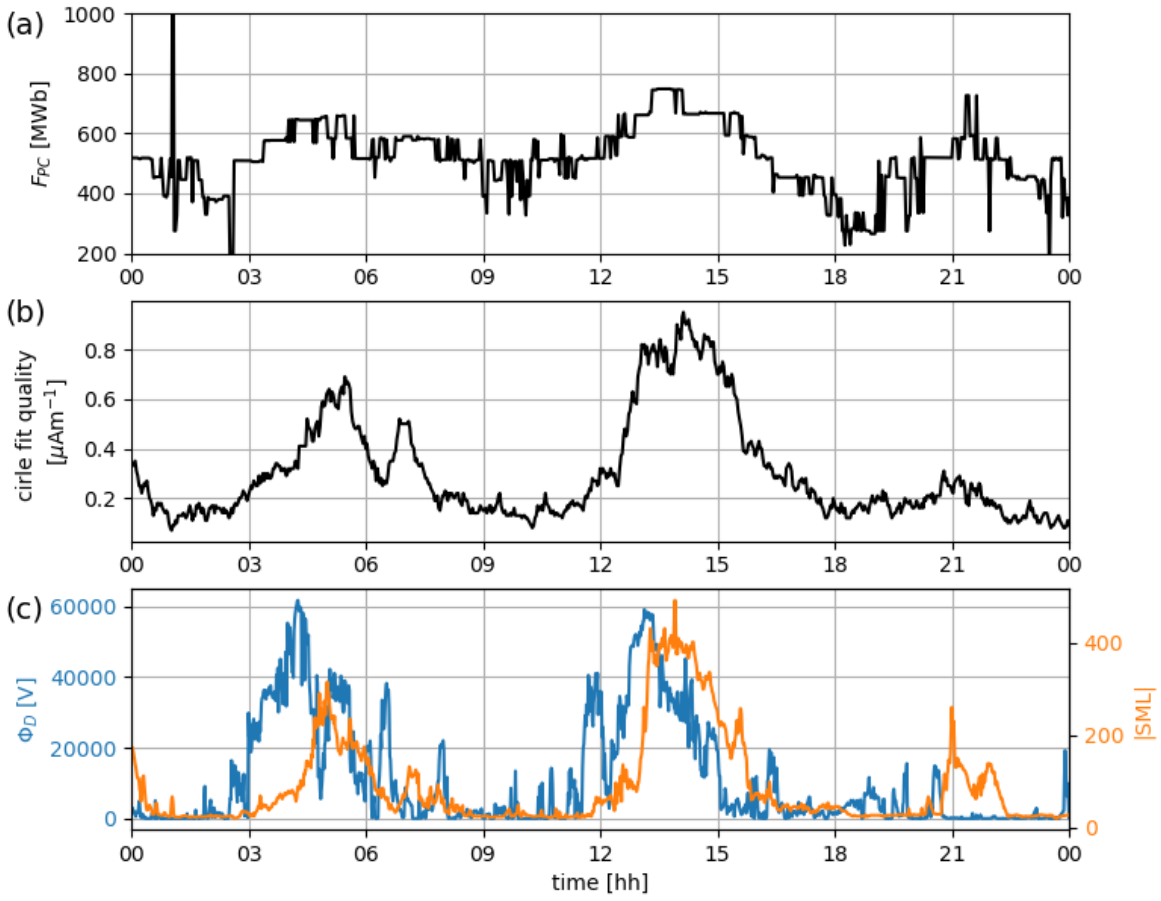

Figure 3.8: **(a)** The same open flux series plotted from earlier examples, 4 March 2010. **(b)** The AMPERE circle fit quality parameter plotted for the same period. **(c)** The blue graph presents Φ_D and the orange graph presents the *SML* index. Comparing these plots indicate how higher quality values are biased towards higher activity periods.

3.4 Data Selection

In this section, we will go through some of the data selection methods used to improve the quality of the data we are analysing. The data we are selecting from envelops most the seven years between 1st January 2010 and 1st January 2017, save for a few data gaps, at a 2 min cadence.

3.4.1 Choosing an Appropriate AMPERE Fit

Earlier, it was presented how the AMPERE data could be fitted as a spline or polynomial fit. Both fits could also be performed for different time windows / knot spacings as shown in figures 3.6 & 3.7. The different methods will be correlated with Φ_D and different geomagnetic indices expected to be highly correlated with Φ_N, to figure out which one should work best. Figure 3.9a shows Φ_D (solid), *SML* (dashed), *PCN* (dotted) and *ASY-H* (dash-dot) indices (explanatory variables) correlated with F and dF/dt in black and red respectively. Additionally there is the dashed blue line which is the *SML-LT* index which only takes into account nightside activity. *SML-LT* will also be referred to as the modified *SML** index.

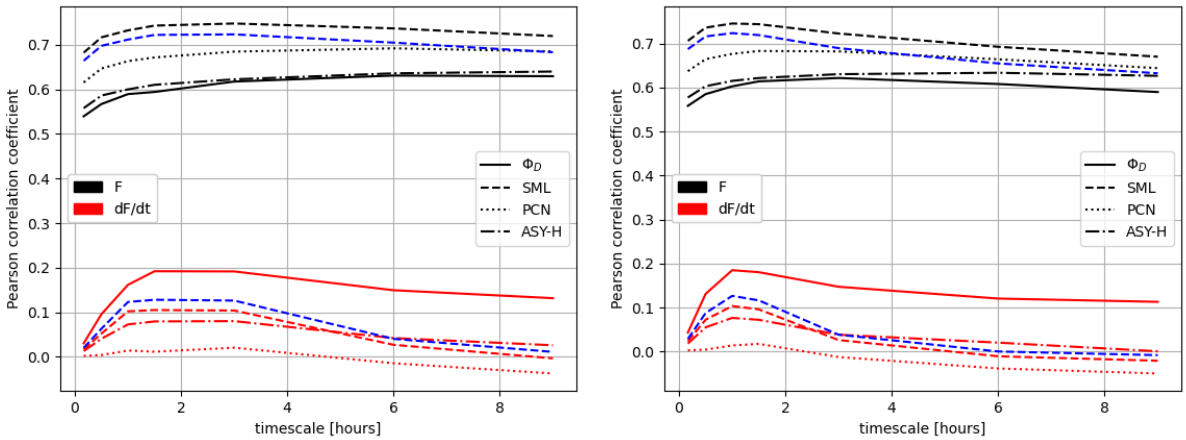

(a) (b)

Figure 3.9: Plots of Φ_D (solid), *SML* (dashed), *PCN* (dotted) and *ASY-H* (dash-dot) indices correlated with F (black) and dF/dt (red) for both polynomial fit (a) and spline fit (b). The plots show the Pearson correlation coefficient for time windows / knot spacing (timescales) between 10 min and 9 hours. The dashed blue lines F and dF/dt correlated with the *SML-LT* index which only takes the nightside into account. The correlation is performed on all seven years of data.

One immediate observation from these plots is that the explanatory variables show a much stronger correlation with F than dF/dt. Interestingly, the correlation with F seems to initially be somewhat similar to what we saw in figure 2.12 from *Laundal et al.* (2020), even

though we are correlating with the open flux and *Laundal et al.* (2020) is correlating with the dayside reconnection. In figure 3.9 however, some of the correlations decrease for higher "timescales", which is expected as we are not using any time averaging on the explanatory variables. With dF/dt, on the other hand, the correlation is much lower. The lower correlation is the opposite trend of what the theory suggests, where at least Φ_D is more closely related to the change in open flux.

From the plots, we see the correlation between dF/dt and the explanatory variables peak at 90 min for the polynomial fit and at 60 min for the spline fit. The lower correlation is likely due to overfitting the curve to noise in the AMPERE data at lower timescales and flattening of the AMPERE series at higher timescales. This flattening is also why the spline fit peaks at a lower timescale than the polynomial fit. The spline shows much less variation for knot spacings of equal length to a polynomial fit window length. Looking at the peaks of the respective fits, it is not apparent which method has a better correlation with the explanatory variables. By visually comparing daily plots of both methods, like in figures 3.6 & 3.7, the polynomial fit seems to portray the AMPERE open flux series more accurately. The lower oscillation rate of the spline fit often fails to pick up changes in AMPERE. The polynomial fit has also yielded better results in regression analyses which will be presented in later sections. Building upon these arguments, we will settle on the 90 min polynomial fit as the best dF/dt fit, which will be used going forwards. From this point on, F_{fit} will refer to the 90 min polynomial fit of the open flux and dF_{fit}/dt to its derivative, representing the change in open flux.

3.4.2 Filtering AMPERE using the Quality Parameter

The seven years of AMPERE data being used contain numerous periods of insufficient quality data. An obvious way to filter out most of the insufficient data is by filtering based on the AMPERE quality parameter mentioned earlier. The first plot in figure 3.10 shows the same AMPERE open flux histogram from figure 3.4 and the second plot presents a histogram of the AMPERE series after performing the polynomial fit in blue. The additional histograms are after removing data with quality below the thresholds. After filtering away data of quality beneath 0.15, 0.3 and 0.5, the remaining data encompasses about three quarters, half and a quarter, respectively, of the total data. Notice how the remaining data tends to distribute itself towards the higher open flux values. This is due to the quality parameter being proportional to the FACs' magnitude, stronger during high activity periods with high open flux. It is more challenging to identify the boundary between the R1/R2 current system during lower activity periods, leading to more noisy data in general. The second plot also showcases how the polynomial curve fit has smoothed the flux data, while some of the discrete flux peaks from AMPERE are still discernible.

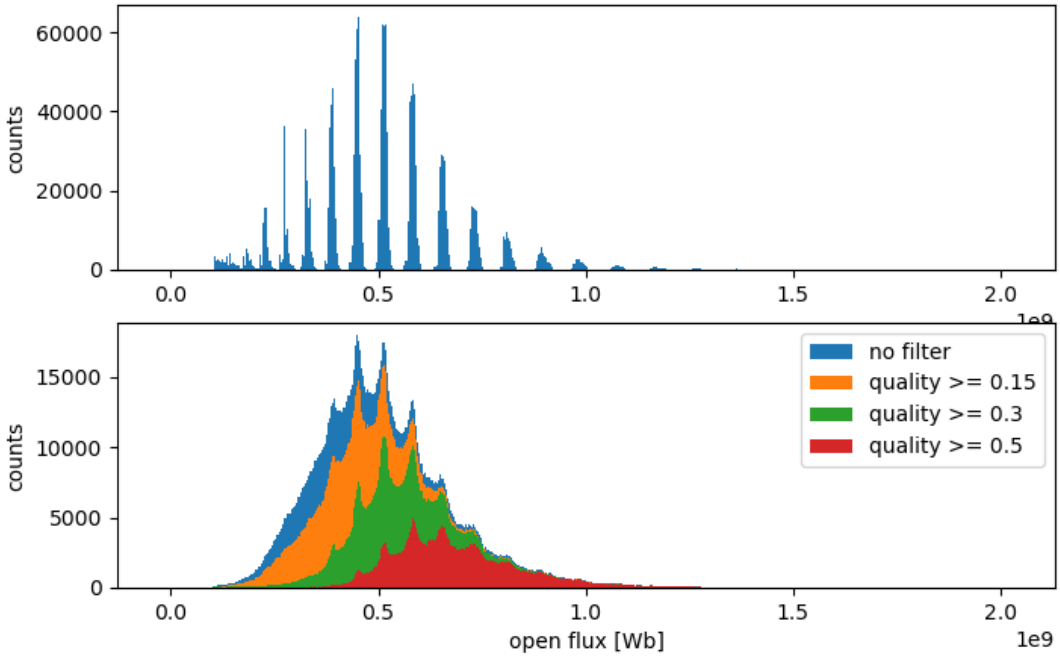

Figure 3.10: The first plot is the same AMPERE open flux histogram from figure 3.4 for comparison purposes. The blue histogram in the second plot shows the entire open flux series like in the first plot, but after the polynomial fit has been performed. The other histograms placed on top are after filtering away values with quality lower than 0.15 (orange), 0.3 (green) and 0.5(red)

Figure 3.11 presents how filtering by quality affects the correlation between the explanatory variables and dF_{fit}/dt. Here we see the advantage of filtering the data by quality, with the correlation of each parameter improving with increasing filter thresholds. A possible trade-off with filtering away lower quality data is the loss of low flux values such that mostly high flux data is taken into account.

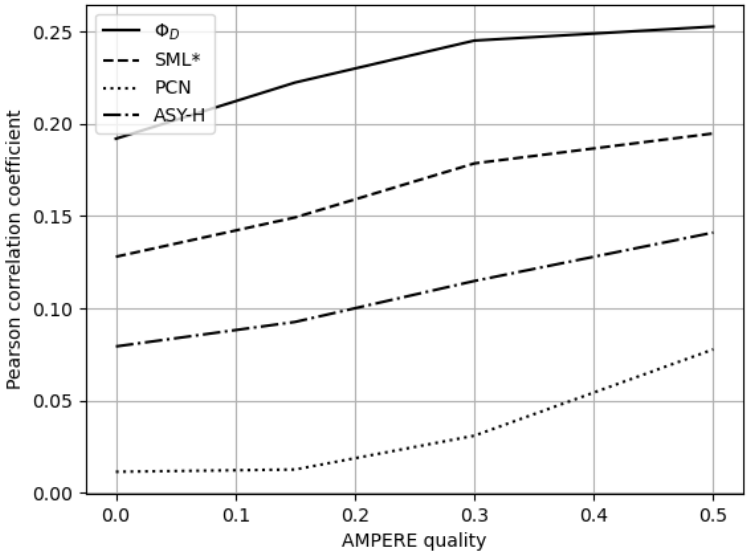

Figure 3.11: Correlation between the explanatory variables and dF_{fit}/dt after filtering out data under qualities 0, 0.15, 0.3 and 0.5.

Filtering out values under 0.5 in quality presents an additional side effect in the distribution of the data. Figure 3.12, presents a histogram with the number of data points related to each month of the year. The blue histogram is for the entire AMPERE data set, showing a similar number of counts for each month. The slight variation in the number of counts is due to the number of days in the respective months. The orange histogram shows the counts left after filtering out values of quality less than 0.5. Here we see a clear bias towards the summer months. There are, for example, about 3.4 times more values left in May versus what is left in January after filtering out lower quality values. This difference is due to the tilt of the Earth relative to the Sun throughout the year. During the summer months, the northern hemisphere tilt toward the Sun increases the ionospheric conductivities, leading to stronger Birkeland currents. Due to the nature at which the quality parameter is calculated, this increase in Birkeland currents also increases the quality parameter value, creating a bias in the data towards the summer months. It is not clear if this bias affects the final analysis and will be ignored, but it is worth mentioning if it is proven otherwise.

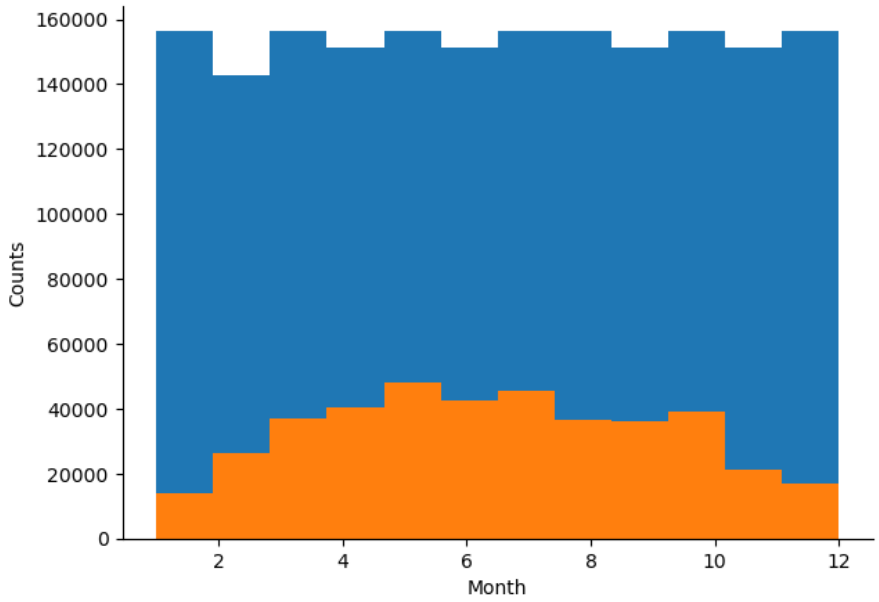

Figure 3.12: Histogram presenting the number of values related to each month of the year. The entire AMPERE data set is presented in blue, and the values left after filtering out lower quality data (less than 0.5) is presented in orange.

3.5 Estimating Change in Open Flux through Multiple Regression Analysis

Multiple regression analysis will be used to establish the relationship between the rate of change in open flux and the dayside reconnection rate and geomagnetic indices. This is to see if the geomagnetic indices can be used as parameters in a proxy for nightside reconnection rate. Multiple linear regression is used to find how several independent variables (predictors) are linearly related to a dependent variable (response).

3.5.1 The Multiple Regression Model

A multiple linear regression model with q predictors and n values is as follows:

$$\mathbf{y} = \mathbf{X}\boldsymbol{\beta} + \boldsymbol{\epsilon} \tag{3.3}$$

where $\mathbf{y}$ is an $n \times 1$ response vector and $\mathbf{X}$ an $n \times (q+1)$ matrix, containing an intercept column and q predictor columns. $\boldsymbol{\beta}$ is a $(q+1) \times 1$ vector of fixed parameters generated by the model, and $\boldsymbol{\epsilon}$ is the $n \times 1$ residual vector. In detailed notation equation 3.3 can be expressed as:

$$\begin{pmatrix} y_1 \\ y_2 \\ \vdots \\ y_n \end{pmatrix} = \begin{pmatrix} 1 & x_{11} & x_{12} & \dots & x_{1q} \\ 1 & x_{21} & x_{22} & \dots & x_{2q} \\ \vdots & \vdots & \vdots & \ddots & \vdots \\ 1 & x_{n1} & x_{n2} & \dots & x_{nq} \end{pmatrix} \begin{pmatrix} \beta_0 \\ \beta_1 \\ \vdots \\ \beta_q \end{pmatrix} + \begin{pmatrix} \epsilon_1 \\ \epsilon_2 \\ \vdots \\ \epsilon_n \end{pmatrix} \tag{3.4}$$

In our case, we want to use multiple regression analysis to create a proxy for the nightside reconnection rate using Φ_D as the parameter for the opening of flux and geomagnetic indices for the closing of flux. In our model, these parameters will be used as predictors, and dF_{fit}/dt will be used as the dependent variable, y. Table 3.1 presents the correlation between the explanatory variables and dF_{fit}/dt (y) for all values, only positive values and only negative values of dF_{fit}/dt. Ideally, Φ_D is only correlated with positive y, and the geomagnetic indices are only correlated with negative y. For negative y, the correlations seem reasonable, with Φ_D showing very low correlation and all the indices being close to 0.3. For positive y, on the other hand, in addition to having a correlation with Φ_D as expected, there is also some correlation with the different indices. The problem with this is that since the indices only have positive values (negative for *SML**), they are only able to model opening or closing of flux, not both. This will sometimes lead to the indices indicating flux closing, while in reality, the index is observing flux opening. For the *PCN* index, this even leads to the index parameter alternating between describing flux opening and flux closing between different regression analyses. Removing some of these variables might help minimise these issues, but we will keep them, for now, to see if there is more reason for or against dropping them later.

With our regression model having Φ_D, *SML**, *PCN* and *ASY-H* as predictors and dF_{fit}/dt as the response, equation 3.3 will take the following form:

	Φ_D	*SML**	*PCN*	*ASY-H*
y	0.25	0.19	-0.08	-0.14
y>0	0.32	-0.03	0.16	0.09
y<0	-0.002	0.28	-0.26	-0.28

Table 3.1: Correlation between the explanatory variables and positive, negative and all values of dF_{fit}/dt (y).

$$\begin{pmatrix} \frac{dF_{\text{fit},1}}{dt} \\ \frac{dF_{\text{fit},2}}{dt} \\ \vdots \\ \frac{dF_{\text{fit},n}}{dt} \end{pmatrix} = \begin{pmatrix} \Phi_{D1} & SML_1^* & PCN_1 & ASY\text{-}H_1 \\ \Phi_{D2} & SML_2^* & PCN_2 & ASY\text{-}H_2 \\ \vdots & \vdots & \vdots & \vdots \\ \Phi_{Dn} & SML_n^* & PCN_n & ASY\text{-}H_n \end{pmatrix} \begin{pmatrix} \beta_1 \\ \beta_2 \\ \beta_3 \\ \beta_4 \end{pmatrix} + \begin{pmatrix} \epsilon_1 \\ \epsilon_2 \\ \vdots \\ \epsilon_n \end{pmatrix} \tag{3.5}$$

In equation 3.5, the intercept vector is removed. This is because dayside and nightside reconnection are equal over long timescales, $\langle \Phi_D \rangle = \langle \Phi_N \rangle$, usually over a few hours, well within the seven years of data we are working. For long timescales, we then have:

$$\left\langle \frac{dF_{\mathrm{PC}}}{dt} \right\rangle = \langle \Phi_D \rangle - \langle \Phi_N \rangle = 0 \tag{3.6}$$

which means the intercept vector defaults to zero in the model.

3.5.2 Describing the Data Set

Before building the model or exploring the data further, some of the key metrics of the data set are presented in table 3.2 to see how the data is distributed and if there are any outliers. The count is the number of data points from about 1.8 million values to around 383 000 after filtering out values with quality less than 0.5. Looking at the respective max/min values of the different variables, we see that they all contain outliers falling well outside three standard deviations of the respective variables. It is not evident whether or not these values should be dropped as, especially for Φ_D and the indices, these are measured quantities that likely come from actual observations and not errors. About 5.3% of the data lies outside three standard deviations, which is much higher than expected for a normal distribution. According to the *three-sigma rule*, only about 0.3% of the data should lie outside three standard deviations, suggesting there is an overrepresentation of outliers, which is a reason for concern. Considering this, we will drop the outliers as they may lead to dubious results. For instance, it is later found that the outliers lead to residuals deviating from a normal distribution.

	Φ_D	SML*	PCN	ASY-H	dF_{fit}/dt
count	3.8e+05	3.8e+05	3.8e+05	3.8e+05	3.8e+05
mean	3.5e+04	-2.5e+02	2.3	3.1e+01	3.8e+02
std	3.5e+04	1.9e+02	1.5	2.1e+01	3.1e+04
min	0.0	-2.6e+03	-1.2e+01	0.0	-3.1e+05
25%	1.3e+04	-3.3e+02	1.4	1.7e+01	-1.7e+04
50%	2.7e+04	-2e+02	2.1	2.6e+01	5.9e+02
75%	4.7e+04	-1.1e+02	3.1	3.8e+01	1.8e+04
max	7.6e+05	3.3e+01	1.9e+01	3.6e+02	2.1e+05
+3 std	1.4e+05	3.3e+02	6.9	9.3e+01	9.3e+04
-3 std	-6.9e+04	-8.3e+02	-2.2	-3.1e+01	-9.2e+04

Table 3.2: Descriptive statistics of the variables used in the regression model.

3.5.3 Building and Evaluating the Model

To build our regression model, we will use the *scikit-learn* library for machine learning in *Python* (*Pedregosa et al.*, 2011). Before performing a linear regression analysis, we will split the data into random train and test subsets. The training subset contains 80% of the data, and the testing subset contains 20% of the data. A model will be generated by performing a linear regression analysis on the training subset. The model then makes a prediction of the testing subset. The purpose of doing this over-performing a linear regression on the whole data set is to avoid overfitting, where the model becomes very good at predicting its own data but worse at predicting a general data set. By passing the training data set through the regression model, we end up with the following parameters:

$$\boldsymbol{\beta} = (0.52,\, 45,\, -270,\, -190) \tag{3.7}$$

This means that for example, a 1 V increase in Φ_D would lead to a 0.52 V increase in $(dF/dt)_{\text{reg}}$ and a 1 nT decrease in *SML** would lead to a 45 V decrease in $(dF/dt)_{\text{reg}}$. The change in open flux predicted by the regression model will be referred to as $(dF/dt)_{\text{reg}}$ to distinguish it from dF_{fit}/dt.

When evaluating the model, we will use the *statsmodels* library for Python (*Seabold and Perktold*, 2010). Before getting into specifics, there are a few fundamental assumptions made when performing a multiple regression analysis:

1. There is a linear relationship between the dependent variable and the independent variables
2. No multicollinearity between the independent variables
3. The residuals are homoskedastic
4. There is no autocorrelation of the residuals
5. The residuals are normally distributed

The assumptions affect the data differently when they do not hold. Some assumptions, if violated, may reduce the reliability of the modelled parameters. The different assumptions will be explained in more detail when we arrive at them while evaluating the model.

Checking for Linear Relationship between Dependent and Independent Variables

Linearity means that the dependent variable can be explained by a linear relationship between the independent variables. In our case, we expect linearity as the model being tested

is based on the linear equation 2.2, with Φ_D and Φ_N represented by the independent variables. One way to identify if the relationships are non-linear is by examining residual plots of the fitted model. Figure 3.13 shows the residual plot of our model. The residual plot is a scatter plot with the predicted values $(dF/dt)_{\text{reg}}$ on the horizontal axis and its residuals with the dependent variable on the vertical axis. The blue dots are from the training subset, and the green dots are from the testing subset. The residual plots are produced with the *Yellowbrick* machine learning extension for Scikit-Learn (*Bengfort et al.*, 2018).

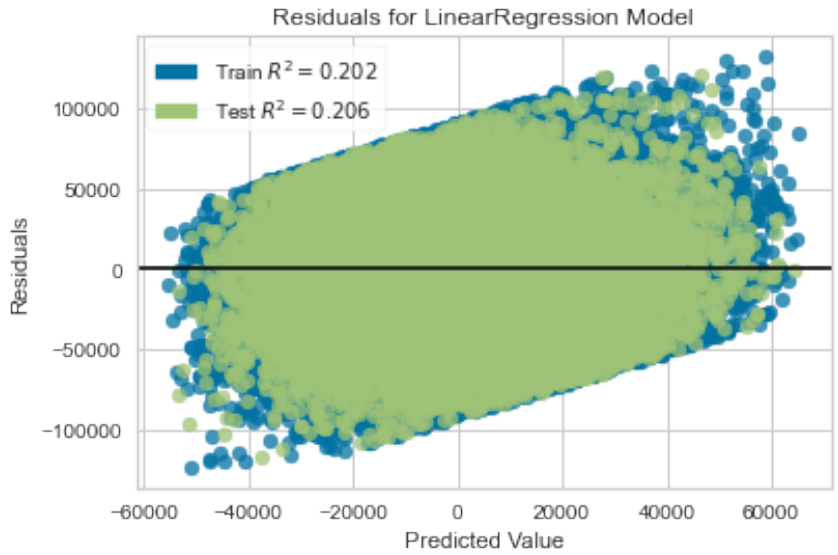

Figure 3.13: Residual plot showing the scattering between the predicted values $(dF/dt)_{\text{reg}}$ and the residuals between $(dF/dt)_{\text{reg}}$ and dF_{fit}/dt. The blue dots show the residuals for the training subset and the green dots for the testing subset.

Suppose there is a linear relationship between the variables in the model. In that case, we expect the residuals to be randomly dispersed, and for non-linear relationships, we expect to see some curvature or a distinct shape in the scatter plot. We see the residuals assuming a diagonal shape with a semi-hard upper and lower edge in our plot. These cutoffs are likely caused by removing outliers outside three standard deviations of the mean. A problem here is that we do not see where the majority of the dots were found due to the sheer quantity of data. Figure 3.14 shows the same plot again, but dots only have an opacity of 1%. Here it is presented that the residuals are clustered around the centre. The histogram on the right side also indicates that the residuals should be normally distributed.

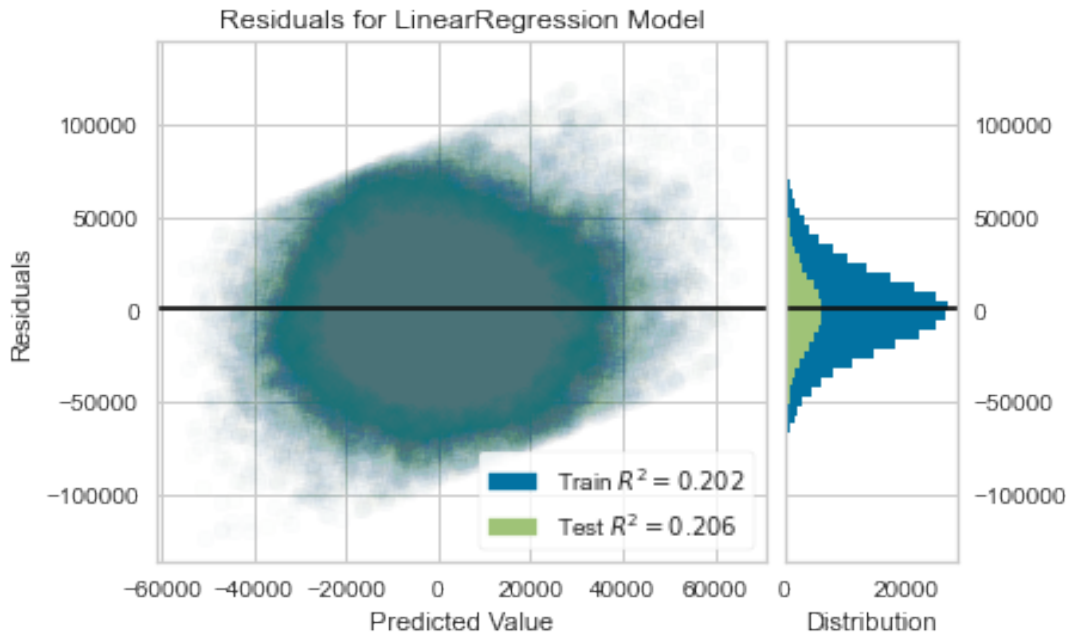

Figure 3.14: Same plot as in 3.13, but the dots opacity is reduced to 1%. The panel to the right contains a histogram showing the distribution of the residuals.

Alternatively, we can create a hexbin plot to identify the distribution of the residuals more clearly. The hexbin plot is a two-dimensional histogram with the predicted values along the horizontal axis and the residuals along the vertical axis, just like the residual plots. But instead of plotting a dot for each residual, a hexagon-shaped grid map is created, where the number of residual points within each bin is counted and presented in a heat map. Figure 3.15 presents two such hexbin plots. On the left-hand side, the hexbin plot is plotted with the number counts represented by a linear scale, and the panel to the right shows the same hexbin plot, but with the number of counts on a logarithmic scale. From these plots, it becomes even more apparent that the majority of the residuals are "hugging" the origin with no clear bias towards any direction. The residual plots do not indicate that the linearity assumption is violated such that a linear regression model is appropriate.

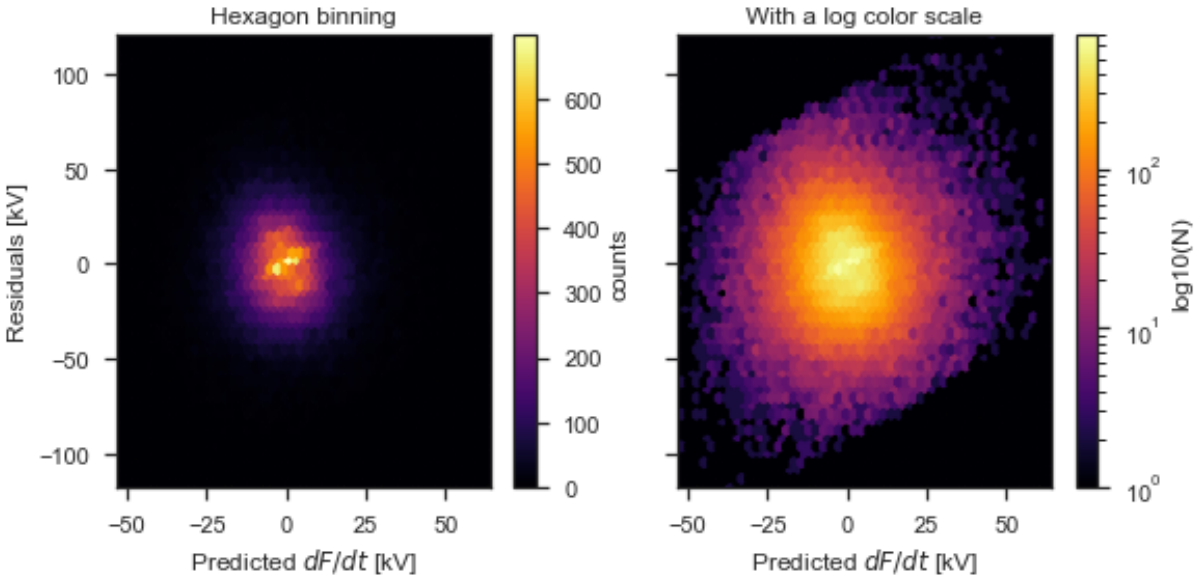

Figure 3.15: Hexbin plots of the residuals with the number of counts within each bin represented by a linear (left) and logarithmic (right) heat map.

Checking for Multicollinearity

Multicollinearity occurs when one of the explanatory variables are highly correlated with another explanatory variable. The problem with multicollinearity is that the coefficient estimates and their standard errors tend to be unreliable. The model will have difficulties isolating the variables' individual effects on the dependent variable with two highly correlated variables. To detect multicollinearity, one can look at the correlation between the individual variables. If the correlation between two variables is particularly high (close to 1 or -1), multicollinearity will likely become an issue. Table 3.3 is a correlation matrix presenting each variables correlation with all other variables, including the dependent variable dF_{fit}/dt. In our case, the highest correlation is found between *SML** and *PCN* at -0.62. The correlation indicates a certain relationship between the two variables; though far from perfectly correlated, it may not be clear if this correlation will be problematic for the model. The correlation between dF_{fit}/dt and the independent variables presented in this table are slightly higher than those found in Table 3.1. This increase comes from removing outliers outside three standard deviations of the mean from the data set.

	Φ_D	SML*	PCN	ASY-H	dF/dt
Φ_D	1.0	-0.36	0.47	0.38	0.29
SML*	-0.36	1.0	-0.62	-0.54	0.20
PCN	0.47	-0.62	1.0	0.56	-0.062
ASY-H	0.38	-0.54	0.556	1.0	-0.13
dF/dt	0.29	0.20	-0.062	-0.13	1.0

Table 3.3: Correlation between the individual variables used in the regression model.

Another way to detect multicollinearity is by looking at the *variance inflation factor* (VIF). The VIF assesses how much the variance of the regression changes by removing and including the different variables. If the variance is greatly affected by adding a certain variable, there should be considerable multicollinearity between that variable and all those already included in the model. So a higher VIF for a variable means more of the information of that variable is already contained within the model. A general recommendation from the statsmodels documentation is that if VIF is greater than 5, the variable is highly collinear with the other explanatory variables, leading to large standard errors in the coefficient estimates. In table 3.4 our initial VIFs are presented in the left column of values. We see that all the indices have a VIF above 5, indicating that multicollinearity is too high between the variables. Removing one of these indices should also reduce the VIF of the other indices, as they all probably have some level of collinearity since they are all expected to be correlated with nightside reconnection. The obvious contender here is the *PCN* index since it both has the highest VIF and the worst correlation with $dF\text{fit}/dt$ as presented earlier. By dropping the *PCN*, we end up with the VIFs presented in the right column of table 3.4. Here we see all the variables are below 5 since their collinearities are reduced by excluding the *PCN* index. From here, we will be working with a new regression model where *PCN* is removed.

Φ_D	3.29	2.91
SML*	5.55	4.40
PCN	7.50	-
ASY-H	5.91	4.86

Table 3.4: VIF of the explanatory variables before (left) and after (right) removing the *PCN* index from the model.

Checking for Heteroskedasticity

One of our assumptions for the regression model is that the residuals are homoskedastic. In other words, homoskedasticity means that the variance of the residuals is constant across all values of the independent variables. We assume there is no heteroskedasticity in our model, which essentially means we have homoskedasticity, where the variance of the residuals is constant. A problem associated with heteroskedasticity is that the standard errors of the output are underestimated because the linear regression model does not detect the increase in variance caused by heteroskedasticity. To check for heteroskedasticity, we can use the *Breusch-Pagan* test. The Breusch-Pagan test performs a new regression to fit our independent variables to the squared residuals from our original regression. If our independent variables are significant in explaining the variance in the residuals, then heteroskedasticity must be present. In the Breusch-Pagan test, we have a null hypothesis that there is homoskedasticity, meaning that if the test returns a p-value less than 0.05, we reject the null hypothesis, and there is heteroskedasticity. In our case, the Breusch-Pagan test returns a p-value of 0, which means the p-value is much less than 0.05, indicating the regression has very high heteroskedasticity.

Another method of identifying heteroskedasticity is by looking at residual plots to see if the scatter of the residuals change with respect to the predicted values. By examining the clustering of scatter points in figure 3.14, we see the main cluster of residuals peak around the predicted value 0 and tapers for predicted values of increasing magnitude. The residuals are lower in magnitude when the independent variables are greater in magnitude and vice versa, indicating heteroskedasticity. From this, we should expect the error between dF_{fit}/dt and $(dF/dt)_{\text{reg}}$ to be at its greatest when $(dF/dt)_{\text{reg}}$ is close to zero. Two of the main reasons for this trend in the errors are significant changes in dF_{fit}/dt when there is little activity present in the independent variables. And lags between dF_{fit}/dt and $(dF/dt)_{\text{reg}}$, causing systematic differences between the two variables which are more prevalent when one of the variables are close to zero. These effects can be observed when we will later look at specific events.

Checking for Autocorrelation

Autocorrelation occurs when there is a significant correlation between a variable and a delayed version of itself. It essentially means that each of the residuals is affected by the one before it, making the error terms dependent on each other. Our regression model assumes that there is no autocorrelation, meaning we have independent error terms. Much like with heteroskedasticity, the problem caused by autocorrelation is that the standard errors of the

model cannot be relied upon. To test for autocorrelation of the residuals, we will use the *Ljung-Box* test. With the Ljung-Box test, we have the null hypothesis that the residuals are independently distributed, and there is no autocorrelation. Similarly to Breusch-Pagan, the Ljung-Box test will return a p-value, where the null hypothesis is rejected if the p-value is less than 0.05. Again for our model, the p-value defaults to 0, indicating that we have a strong correlation in the residuals.

The autocorrelation function is plotted in figure 3.16with lags on the horizontal axis and the correlations on the vertical axis. Additionally, there is also a blue-shaded region around the horizontal axis, indicating the confidence intervals of the correlation. If the autocorrelation values go beyond this shaded region, the correlation can be assumed to be statistically significant. In our case, the autocorrelation seems to be very significant as we have a very low confidence interval, barely intelligible from the horizontal axis.

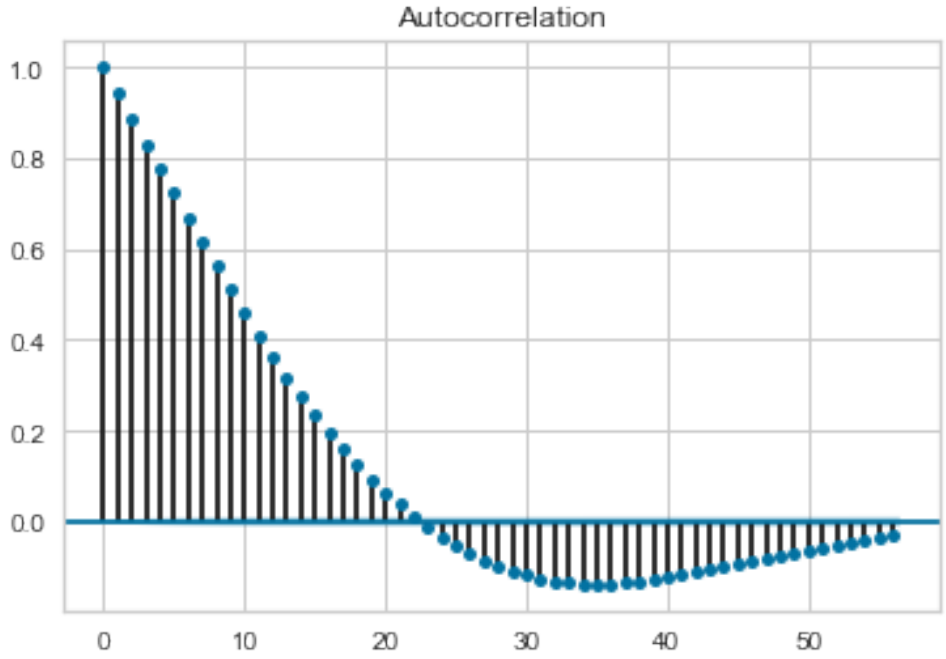

Figure 3.16: Autocorrelation of the regression residuals for increasing lags.

In our model, the autocorrelation present is primarily due to variations in dF_{fit}/dt not picked up by the explanatory variables. Later we will find that the R-squared of the model is fairly low, meaning the majority of the variation in dF_{fit}/dt is not being represented by $(dF/dt)_{\text{reg}}$. As seen from the residual plots presented earlier, the errors are generally most significant around zero, which is also probably where we have the greatest autocorrelation due to the variations in dF_{fit}/dt when the exploratory variables are small.

Checking for Normally Distributed Residuals

Our last assumption is that the residuals of the regression are normally distributed. In figure 3.14, a histogram of the residuals was presented, where the residuals seem to assume a normal distribution. Another way to check the normality is by visually assessing a Q-Q (quantile-quantile) plot of the residuals, presented in figure 3.17. For each point (x, y) in the Q-Q plot, a sample quantile (y-coordinate) plotted against the corresponding theoretical quantile (x-coordinate). The sample quantiles represent each of the n residuals from the regression model. Each value in the theoretical quantiles represents a quantile of a normal distribution partitioned into n equally probable quantiles, given in standard deviations from the median. If the residuals are normally distributed, most of the points will be on the straight red line. In our case, this is mostly true, except for some slight deviations towards the outlying values. Regardless, the linearity of the points suggests that the residuals are normally distributed.

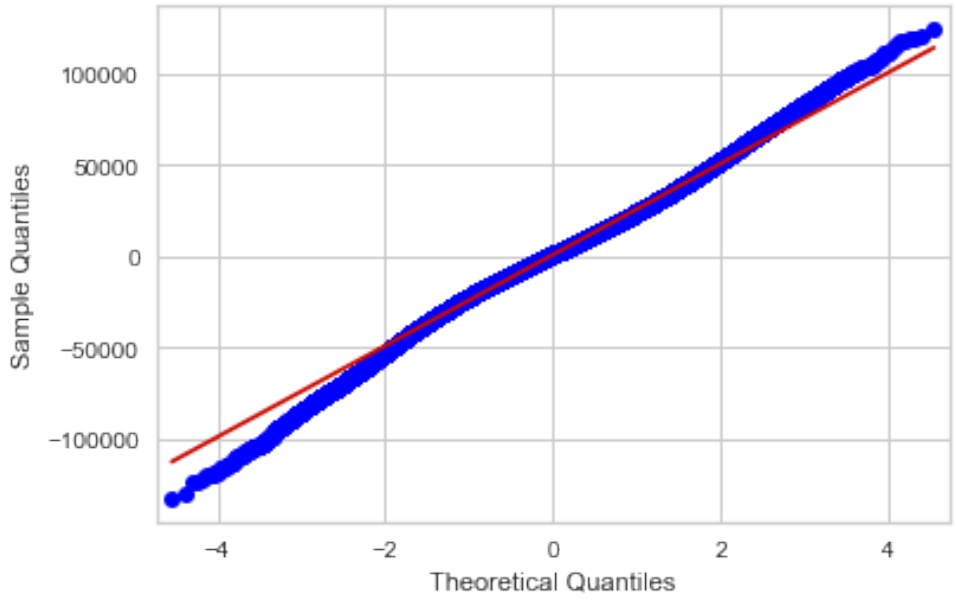

Figure 3.17: Q-Q plot of the residuals (blue dots) compared to a normal distribution (red line).

3.5.4 Regression Model Summary

Moving on from testing the assumptions of the regression model, table 3.5 summarises some of the results from the regression analysis. First, we have the *mean absolute error* (MAE), the *mean squared error* (MSE) and the *root mean squared error* (RMSE), giving a measure of how well our data fit the model. The mean absolute error is the mean of the absolute value of the residuals of the model. The MAE gives an idea of the magnitude of the errors. The mean

squared error is the mean of the squared errors. Squaring the residuals have the added effect of "punishing" more significant errors over MAE. The root mean squared error is the square root of the mean squared error. RMSE is usually favoured as it both punishes significant errors and gives an error in the same units as the dependent variable. In units of open flux change, the RMSE of the model gives us a total error of 25 kV. This error is quite significant as the absolute mean value of dF_{fit}/dt is only about 21 kV in comparison.

The *R-squared* metric provides a way to measure the goodness of fit between the model and the data. The metric output is between 0 and 1, where 1 is a 100% matching fit between the data and the model. In our case the R-squared is 0.203, which means the independent variables are explaining 20.3% of the variation in the dependent variable, dF_{fit}/dt. A limitation with R-squared is that the score will increase as the number of independent variables increases, even if they have almost no correlation with the independent data. To combat this, the *adjusted R-squared* metric penalises models with multiple variables with little impact on the model, reducing the score. In our case, the R-squared and adjusted R-squared are the same, so there are no unnecessary variables.

Next, we have summary statistics for each of the independent variables. The coef column shows the estimated coefficients of the independent variables, producing the $\boldsymbol{\beta}$ vector:

$$\boldsymbol{\beta} = (0.51,\ 46,\ -197) \tag{3.8}$$

The next column shows the standard errors of the respective regression coefficients, measuring how precisely the model estimates the coefficients. Dividing the regression coefficients by their standard errors calculates the t-values. The higher the magnitude of the t-value, the more significant the variable is in the regression model. In our case, Φ_D is the most significant for the model, and *ASY-H* is the least significant. Next is the p-value related to the null hypothesis that the coefficients are equal to zero. If we fail to reject the null hypothesis, there is a significant chance that the coefficients are zero, meaning they may have no real impact on estimating the dependent variable. In our case, all p-values are near zero, so we reject the null hypothesis, and the coefficients should not equal zero. We also see the same result in the 95% confidence intervals presented in the last two columns. The confidence intervals exclude zero for all variables, so their coefficients should not equal zero. However, due to the residuals being heteroskedastic and suffering from autocorrelation, the standard errors and the other statistics describing the uncertainty of the variables, all highlighted in red, are unreliable. These uncertainties should likely be more significant if heteroskedasticity and autocorrelation were not present.

	MAE:	1.92e+04	**R-squared:**		0.203	
	MSE:	6.25e+08	**Adj. R-squared:**		0.203	
	RMSE:	2.5e+04				
	coef	**std err**	**t**	**P> |t|**	**[0.025**	**0.975]**
Φ_D	0.5135	0.002	293.071	0.000	0.510	0.517
SML	46.2543	0.312	148.472	0.000	45.644	46.865
ASY-H	-196.5362	2.810	-69.934	0.000	-202.044	-191.028

Table 3.5: Summary statistics of the $(dF/dt)_{\text{reg}}$ regression

Chapter 4

Results

This chapter presents the results and is divided into three parts. First, we present spectral analysis periodograms of the different variables used in the study in order to identify periodicities associated with various magnetospheric and solar processes. Second, we present the summary statistics of two regression models alternative to the one presented in Section 3.5. Last, we present our estimates by plotting them for a few selected days, giving a comprehensive overview of the resulting observations.

4.1 Spectral Analysis of Magnetospheric Variables

The following section will look at periodograms of the different magnetospheric parameters we are using and investigating. A periodogram is an estimate of the power density of a signal for different sinusoidal periods. In our parameters, we might expect to observe periodicities related to magnetosphere processes and the solar wind, i.e. substorm periodicity, solar rotation, annual or semi-annual changes. For our data, we will use the *Lomb-Scargle method*, a form of least-squares spectral analysis which allows for data gaps in the signal. Figure 4.1 presents the Lomb-Scargle periodograms for F_{fit}, dF_{fit}/dt, Φ_D, *SML*, *PCN* and *ASY-H*. The power density of periodic signals of periods between 10 minutes and 400 days are plotted on a linear time scale. Figure 4.2 presents the same plots on a logarithmic time scale to readily observe the power distribution of shorter periods.

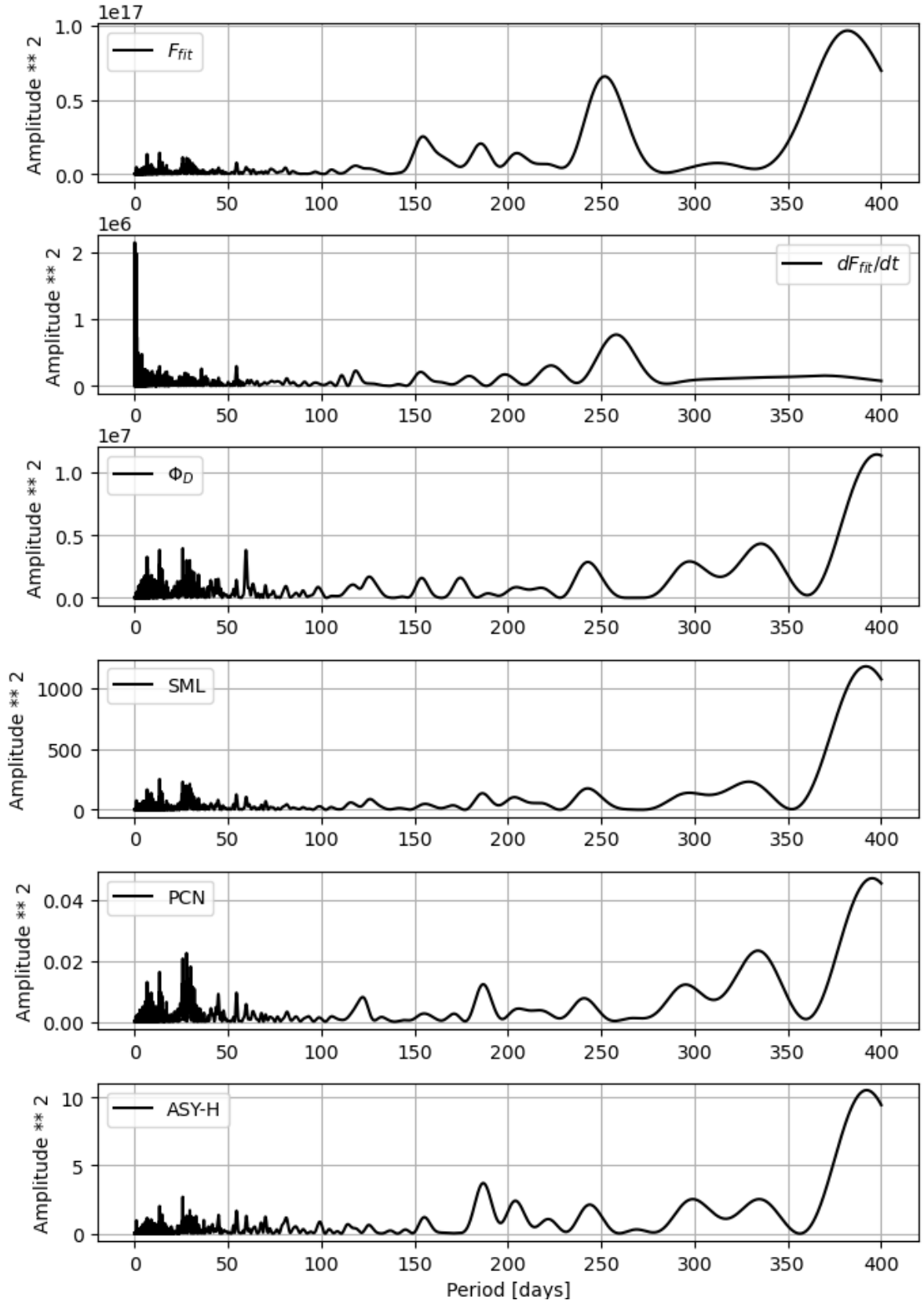

Figure 4.1: Lomb-Scargle periodograms for F_{fit}, dF_{fit}/dt, Φ_D, *SML*, *PCN* and *ASY-H* for periods between 10 min and 400 days. The periodogram is plotted on a linear time scale, showcasing the higher periodicities.

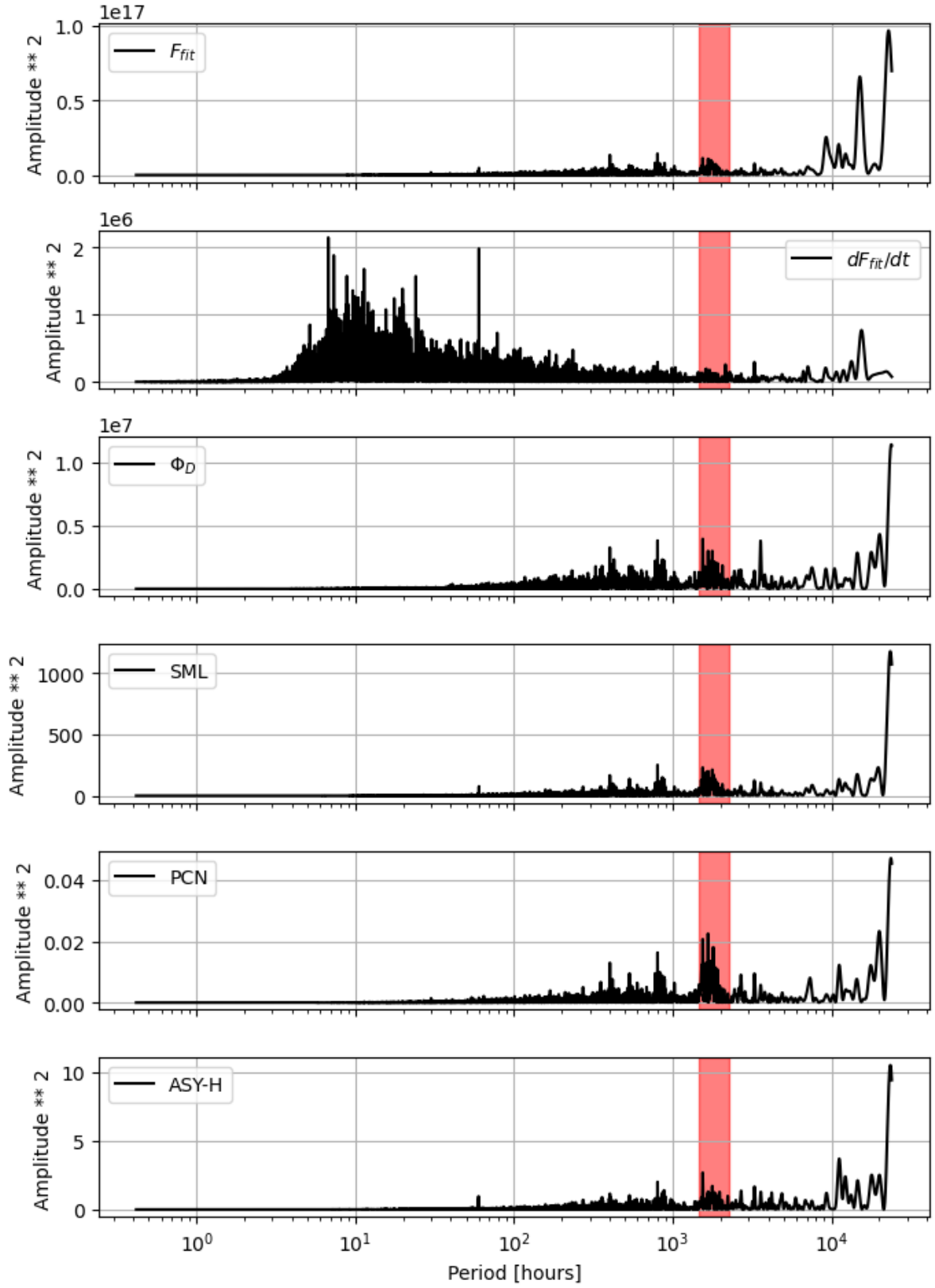

Figure 4.2: Same periodograms as presented in Figure 4.1 with a logarithmic time scale to better illustrate lower periodicities.

Comparing the periodograms for the different variables, we see several signatures shared

amongst them. The largest amplitude in all variables, except for dF_{fit}/dt, is found in periods between 350 and 400 days. These amplitudes are likely related to annual periodicities present in the signals. Around 250 days, we see another signature that is present in all variables. In Figure 4.2, we see the periodograms are much noisier for lower periodicities. Especially for dF_{fit}/dt, it is difficult to tell whether we are looking at actual signatures or noise on the signal. However, the increase in amplitude seen in the red shaded areas might be of interest. The shaded areas indicate periodicities related to the solar rotation period varying from 24.47 days at the equator up to around 38 days near the poles, explaining the increases in amplitude for this period. We can see this signature present in all variables, except for dF_{fit}/dt, meaning it is lost after differentiating F_{fit}.

4.2 Other Multiple Regression Models

In section 3.5, we went through multiple regression model, relating dF_{fit}/dt to Φ_D, *SML** and *ASY-H*. Now we will present the results from two other regression models, one estimating Phi_N and the other estimating F_{PC}. For these models, we will not go through the process of testing for the different assumptions of the models as the results are very similar to that of the dF/dt model. In the next two sections, we will present the other models' summary statistics and point out some of the differences between the models.

4.2.1 Nightside Reconnection Model

This model will exclude Φ_D from the independent variables and try to predict the nightside reconnection rate exclusively. The dependent variable, Φ_N, is calculated by subtracting the change in flux estimated by the polynomial regression, dF_{fit}/dt, from the dayside reconnection rate estimated with Equation 2.8, Φ_D. Φ_N is calculated from the following equation:

$$\Phi_N = \Phi_D - \frac{dF_{\text{fit}}}{dt} \tag{4.1}$$

For independent variables, the *SML**, *ASY-H* and *PCN* indices are used. The *PCN* index was allowed back into the model since the VIF is reduced by removing Φ_D from the model. Table 4.1 presents the summary results of the $\Phi_{N,\text{reg}}$ regression model. The error estimates are about the same as what we saw for the $(dF/dt)_{\text{reg}}$ model. On the other hand, the R-squared is noticeably higher at 0.291 versus 0.203, almost a 50% increase. This increase, however, does not necessarily mean that this method is better than the one presented in the previous chapter. This increase in correlation is likely because of the independent variables correlat-

ing with the Φ_D component from Equation 4.1 and not necessarily with dF_{fit}/dt.

The motivation behind creating a model for Φ_N is to force the coefficient of Φ_D to be equal to one. This is the same as assuming that the dayside reconnection rate is adequately estimated using Phi_D. Since dF_{PC}/dt and Φ_D have the same units (Wb s^{-1}) and should be directly proportional to each other, it makes physical sense for both variables to have the same size. From the $(dF/dt)_{\text{reg}}$ model, Φ_D got a coefficient of 0.51, indicating that only half of the dayside reconnection rate is impacting the open flux increase of the polar cap. We will later compare how these models perform in comparison to each other when looking at specific events.

MAE:	1.69e+04	**R-squared:**	0.291
MSE:	5.18e+08	**Adj. R-squared:**	0.291
RMSE:	2.28e+04		

	coef	**std err**	**t**	**P> |t|**	**[0.025**	**0.975]**
SML	-41.8	0.540	-77.5	0.000	-42.9	-40.8
PCN	6422	66.9	96	0.000	6291	6553
ASY-H	444	4.92	90.4	0.000	435	454

Table 4.1: Summary statistics of the $\Phi_{N,\text{reg}}$ regression

4.2.2 Open Flux Model

From Figure 3.9a, we see that Φ_D and the different indices have much greater correlation with F_{fit} than with dF_{fit}/dt. Based on this information, performing a regression analysis directly on the open flux series might yield a better result. Figure 3.8 gives a good indication as to why the open flux and the other variables are so well correlated. Generally, for high open flux values, the other variables are also greater in magnitude and the opposite for lower values. The argument against building a model based on the open flux is that assuming the geomagnetic indices are correlated with nightside reconnection, it makes less physical sense for the Φ_D and the indices to explain better the open flux, based on Equation 2.2.

Table 4.2 presents the summary statistics of the F_{reg} regression model. In this model, a constant of 428 MWb has been added as some open flux is always expected to be present in the polar caps. The open flux model also allowed for incorporating all the other variables with respect to multicollinearity since much of the VIF is being absorbed by the constant.

The coefficients and errors we obtain here are very different to those of the previous models. These numbers are difficult to compare with the other models since they explain different

phenomena, open flux and change in open flux. One change worth note is the much improved R-squared value at 0.538.

MAE:	6.99e+07	**R-squared:**	0.538		
MSE:	6.99e+15	**Adj. R-squared:**	0.538		
RMSE:	9.03e+07				
	coef	**std err**	**t**	**P> |t|**	**[0.025**	**0.975]**
const	4.28e+08	2.14e+05	1997	0.000	4.28e+28	4.28e+08
Φ_D	1177	5.94	198	0.000	1167	1189
SML	-4.97e+05	1139	-436	0.000	-4.99e+05	-4.94e+05
PCN	2.02e+06	1.27e+05	15.9	0.000	1.77e+06	2.27e+06
ASY-H	1.95e+06	1.05e+04	186	0.000	1.93e+06	1.97e+06

Table 4.2: Summary statistics of the F_{reg} regression

4.3 Events

In this section, we will present the results from our models for a few selected days. Event 1 is the same day presented in earlier examples from the previous chapter. This is the only event presented with lower quality AMPERE data in it, showcasing why we choose to avoid these periods. Event 2 presents a two day high activity period showing a large discrepancy between the estimated nightside reconnection rate and the dayside reconnection rate, violating the ECPC. Events 3 and 4 show two of the better days found in the seven-year period, where the disparity between the open flux change from AMPERE and the regression models are minimal.

4.3.1 Event 1

Figure 4.3 presents the model results for 4 March 2010, the same day we used as an example in Chapter 3. Figure 4.3a presents the open flux series for the selected period. In blue and orange are the AMPERE north open flux series, F_{AMPERE}, and 90 min polynomial fit, F_{fit}, respectively, same as in Figure 3.6. In addition, the black line shows the open flux series predicted by the open flux regression model, F_{reg}, presented in Section 4.2.2.

Figure 4.3b presents the polynomial fit open flux change, dF_{fit}/dt, in orange and the dayside reconnection, Φ_D, calculated from Equation 2.8 is plotted in green. Φ_N (purple), is calculated by rearranging Equation 2.2 and solving for Φ_N, $\Phi_N = \Phi_D - dF_{\text{fit}}/dt$. The black line shows

the nightside reconnection predicted by the regression model, $\Phi_{N,\text{reg}}$, presented in Section 4.2.1. The purpose of this panel is to present what the different components of Equation 2.2 looks like, assuming Φ_D and dF_{fit}/dt are accurate, and to see how $\Phi_{N,\text{reg}}$ and Φ_N relates to each other.

In Figure 4.3c, the flux change model, $(dF/dt)_{\text{reg}}$, from Section 3.5, is compared to dF_{fit}/dt. The green and purple graphs represent the components of the regression model responsible for opening and closing of flux, respectively.

In Figure 4.3d, an alternative method of estimating open flux change is presented in black, by subtracting $\Phi_{N,\text{reg}}$ (purple) from Φ_D (green). Finally, in Figure 4.3e, the AMPERE quality parameter is plotted.

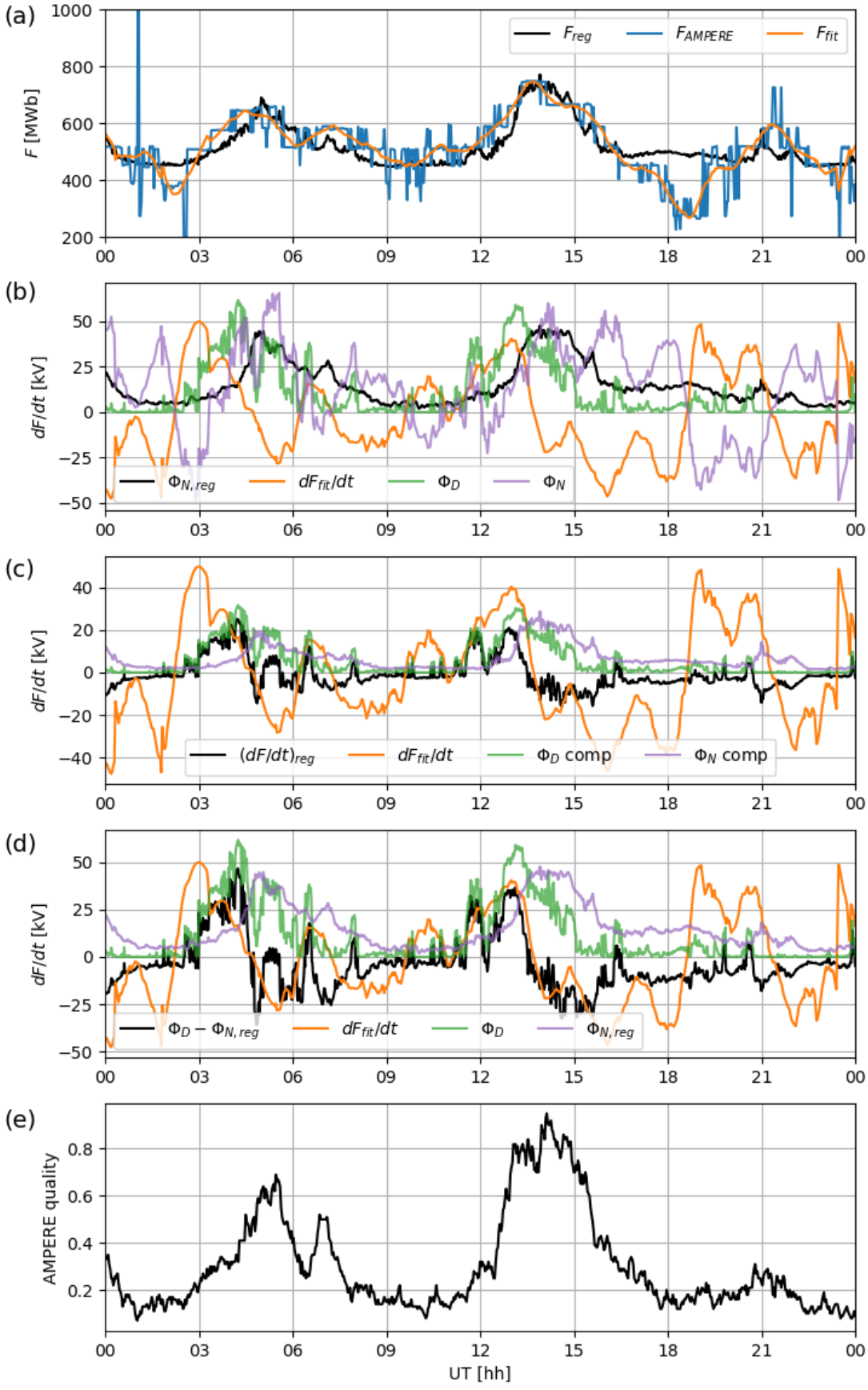

Figure 4.3: Different variables and regression models plotted for 4 March 2010.

Unlike the other events we will look at, Figure 4.3 presents a relatively low activity day. The AMPERE quality stays below 0.5 for most of the day, which is less than in the data we used when building the respective models. Plotting this low-quality data helps illustrate why we avoid using the lower quality data. Throughout most of the day, except for the two short periods of higher activity, we see the F_{AMPERE} series is quite noisy, sporadically shifting between different highly dispersed open flux values. For example, between 00-03 UT and after 18 UT, it should not be possible for F_{PC} to change so drastically as we see in these periods. The noisy open flux data comes from the R1/R2 boundary fit method, failing to identify correctly at which colatitude the boundary is located. The consequence of these inaccurate estimates is that the fitted open flux series, F_{fit}, estimates changes in open flux, which are not present in reality. The differentiated open flux series, dF_{fit}/dt, will, in return, show periods of flux opening or flux closing which does not exist. We can see an example of this between 18-21 UT in Figure 4.3b. Here, dF_{fit}/dt shows a period of strong flux opening, but the dayside reconnection rate, Φ_D, is barely present. The greater dF_{fit}/dt than Φ_D in this period suggests that we have a negative nightside reconnection rate, Φ_N, which should not be possible. These periods of negative nightside reconnection are relatively common in the data set where about 25% of the estimated Φ_N values are negative. This amount is reduced to around 13% after removing values under quality 0.5.

4.3.2 Event 2

Figure 4.4 plots a two day period from 15 to 17 July 2012. Here we see what looks like an intense reconnection event lasting for about one and a half day. The event starts after 06 UT the 15th, with Φ_D increasing to the abnormally high value of 300 kV, considering 99% of the Φ_D values are below 100 kV (Fig. 4.4b, d). The dayside reconnection event lasts continuously, slowly subsiding until about 15 UT the next day. In panels c and d, we see the nightside reconnection derived from the geomagnetic indices producing a much lower reconnection rate than Φ_D.

A consequence of this imbalance is that the change in flux from the regressions models will be continuously positive for the entire period. For example, integrating $(dF/dt)_{\text{reg}}$ from panel c leads to a total open flux of 100 GWb, much greater than the maximum of around 2 GWb found in the AMPERE data. We can conclude from this event that there are instances where the indices used fail to pick up on the magnitude of the nightside reconnection rate.

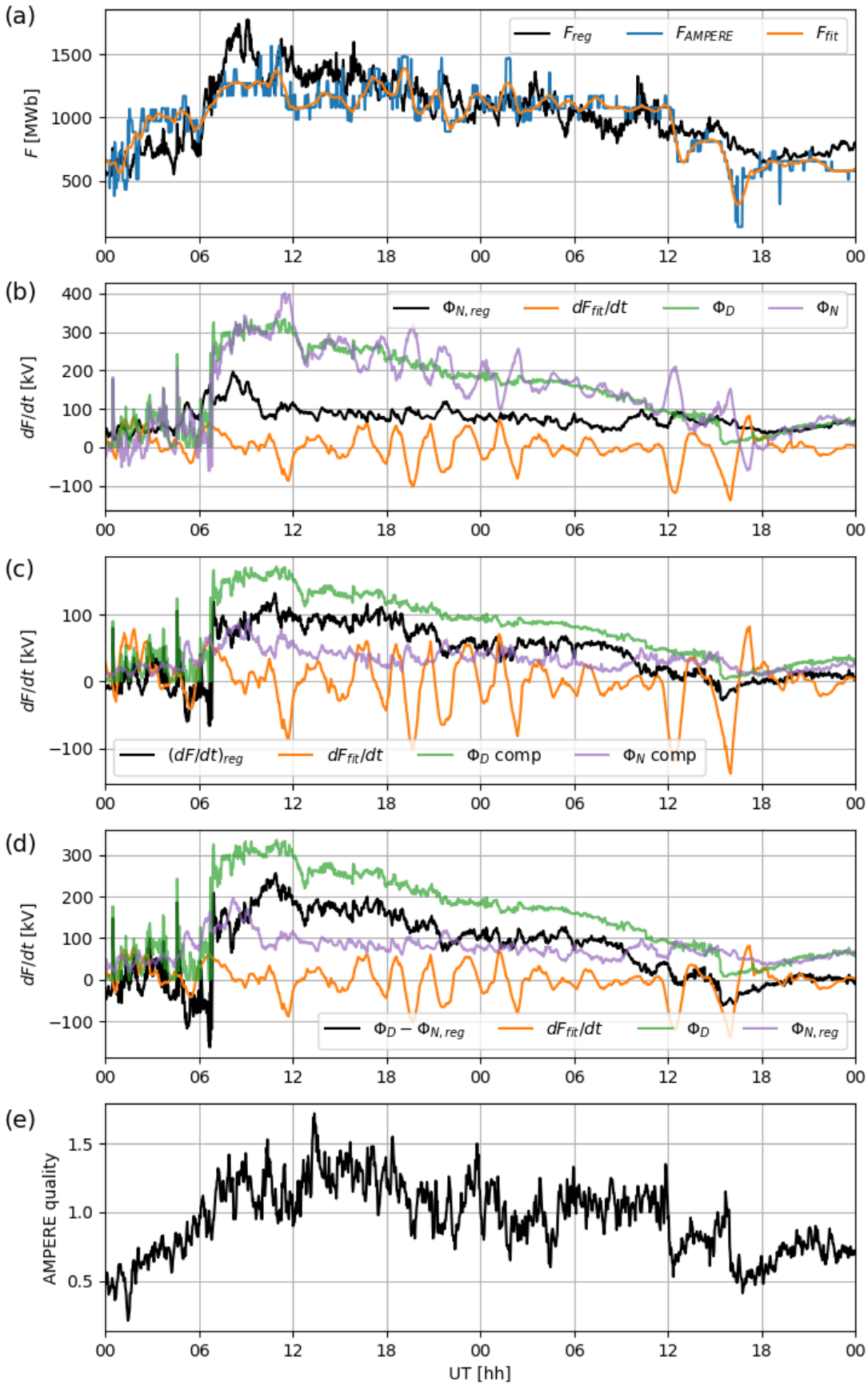

Figure 4.4: Different variables and regression models plotted for 15 & 16 July 2012.

4.3.3 Events 3 & 4

Figures 4.5 & 4.6 shows plots for 08 October and 21 December 2015, respectively. These are two of the days where the closest resemblance between dF_{fit}/dt and the regression models were found. However, dF_{fit}/dt and the regression models are still not reaching correlations surpassing 0.5, meaning most of the variation in dF_{fit}/dt is still not explained by the regression models.

In Figure 4.5 there is a sharp decrease in dF_{fit}/dt from about 04 UT to 06 UT. In panels c & d, we see the decrease reflected by the flux change estimated by the regression models. However, the decrease estimated by the regression models precedes dF_{fit}/dt by a few tens of minutes. These premature occurrences of flux change estimated by the regression models are fairly common in the time series as a whole, suggesting the geomagnetic indices used to model the flux closing are a reaction to nightside reconnection before the open flux estimated with AMPERE. In Figure 4.6 we see two similar signatures around 08 UT and 12 UT.

Judging by the flux opening and closing components of dF_{reg}/dt (Fig. 4.5c) in the period between 03 UT and 12 UT, 07 October 2015, we see a period of steady Φ_D starting right after 03 UT and ending around 10 UT and a period of Φ_N from around 05 UT to 12 UT. There seems to be a slight increase in the Φ_N component before 05 UT. This increase might be due to the geomagnetic indices responding to the onset of Φ_D. We also see this occurrence reflected by F_{AMPERE} series (Fig. 4.5a). After 03 UT, the open flux increases steadily until a brief steady-state period (05 UT - 06 UT), followed by a short period of flux closing due to stronger Φ_N, around 06 UT. Afterwards, we again see a period of flux opening until the dayside reconnection starts subsiding, around 09 UT. Finally, the open flux again decreases from the delayed Φ_N induced by the Φ_D period (09 UT - 11 UT).

In panel b, there is a small spike in the nightside reconnection rate, derived from subtracting dF_{fit}/dt from Φ_D, just after 03 UT. In this same period, Φ_D quickly reaches 100 kV, while dF_{fit}/dt more slowly reaches the same magnitude. In this situation, we can assume that dF_{fit}/dt and Φ_D should be equal in the beginning, with no nightside reconnection present. But dF_{fit}/dt is lagging behind Φ_D and does not detect the same increase in flux change. The lag can be partly due to the averaging window of the polynomial fit dampening changes in the AMPERE open flux estimates and partly due to the open flux estimates not being entirely accurate.

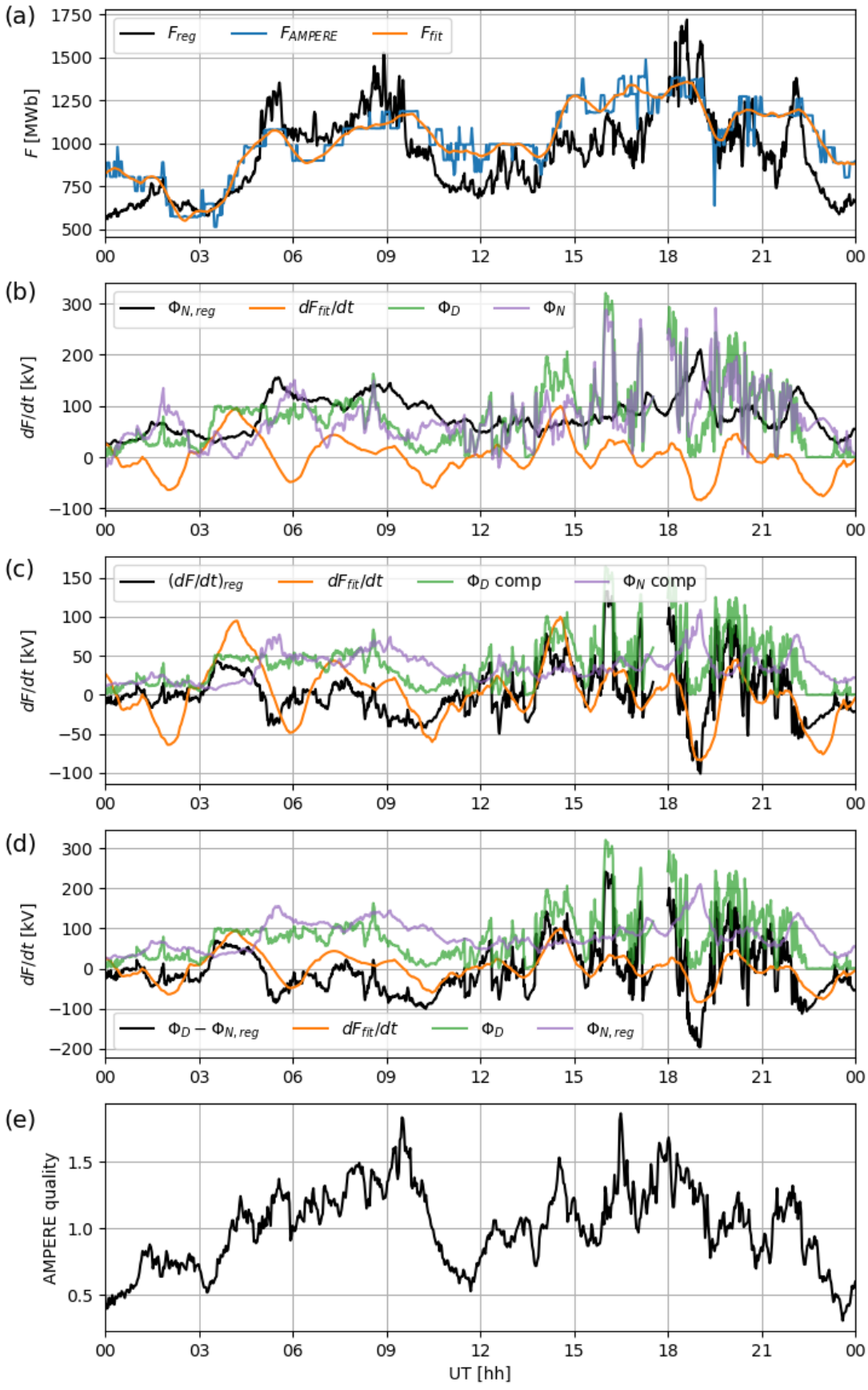

Figure 4.5: Different variables and regression models plotted for 08 October 2015.

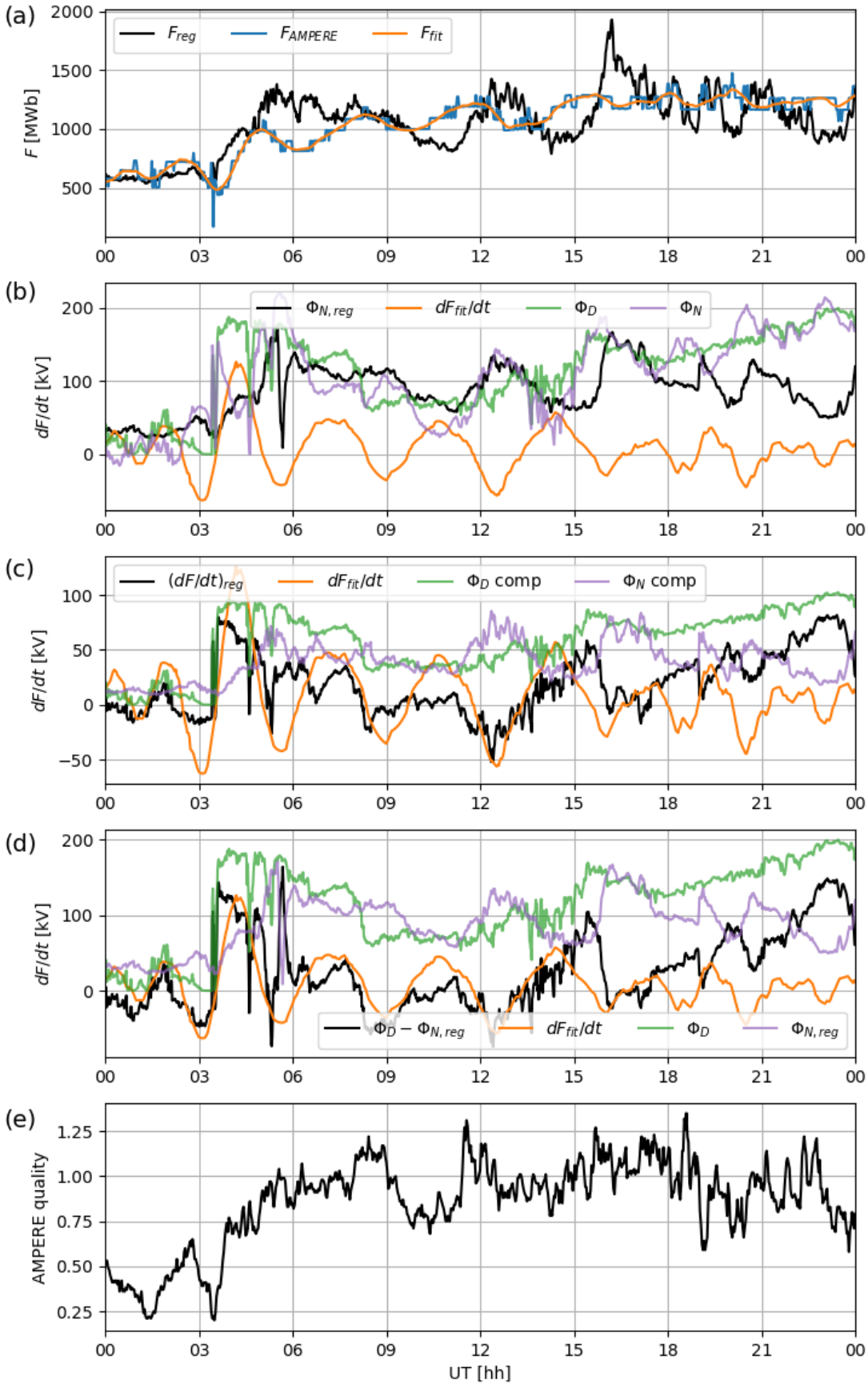

Figure 4.6: Different variables and regression models plotted for 21 December 2015.

Chapter 5

Discussion

In this chapter, we will discuss our results and the choices we made throughout the study. First, we discuss the fitting technique used to represent F_{fit} as the accuracy of the estimated open flux has a significant impact on our results. We discuss the presence of dual-lobe reconnection as a possible source of additional inaccuracies. Previous attempts at expressing the ECPC by integrating Φ_D and the geomagnetic indices are also briefly discussed. Next, we attempt to quantify the error of the open flux change series, dF_{fit}/dt. Finally, we discuss which of the different regression models is best at estimating changes in open flux or nightside reconnection rate.

5.1 Limitations of the Open Flux Averaging

As explained in Section 3.4, the 90 min polynomial fit, F_{fit}, was the resulting fit chosen to represent the polar cap open flux. This fit was ultimately decided upon due to retaining most of the variation observed in the AMPERE open flux series while simultaneously minimising the effect of noise. Because of the 90 min averaging of the open flux data, we are limited in observing physical phenomena over shorter timescales. Among these phenomena is the substorm phase with increased nightside reconnection, the substorm expansion phase. The expansion phase is typically shorter than the 90 min averaging period. For example, in *Milan et al.* (2007) substorm reconnection events were found to last 70 min, on average. The longer averaging window means that we will not accurately observe the exact period of flux closing caused by the nightside reconnection events. It is also difficult to observe variations in Φ_N during the nightside reconnection periods. Ideally, we want to obtain open flux data with a shorter timescale dependence akin to the 10 min timescale of the AMPERE open flux series, but this is unfortunately not viable due to the high level of noise in the open flux estimates, and the satellite separation in each orbital plane in the first Iridium fleet used in this study.

5.2 Impact of Dual-Lobe Reconnection

Magnetic reconnection between the magnetosphere and the IMF does not necessarily occur only at the magnetopause or in the magnetotail. During prolonged periods of northward-directed IMF, the IMF can reconnect with the sunward edge of both the magnetotail lobes, referred to as *dual-lobe reconnection* (DLR) (*Imber et al.*, 2006). The effect of DLR is that open field lines mapping to the sunward edge of the polar cap are closed, meaning we have flux closing on the dayside ionosphere. DLR also leads to what is known as horse collar auroral events (*Milan et al.*, 2020). It is not known how the presence of DLR might affect the AMPERE open flux estimates, which can possibly lead to additional inaccuracies. DLR might also affect the geomagnetic indices used, differently to how they are affected by nightside reconnection. This is especially true for the modified *SML** index, which only takes into account *SML* measurements from the nightside quadrant. Ideally, the geomagnetic indices would be affected at an equal rate from flux closing through nightside reconnection and dual-lobe reconnection. However, since we are mostly focusing on high activity periods, when B_Z is generally southward, we do not expect much DLR activity.

5.3 Estimating Open Flux through Integration

From the ECPC (Eq. 2.2), the dayside and nightside reconnection rates are directly proportional to the change in open flux. However, in empirical studies, the open flux itself is generally measured. Models estimating Φ_D and/or Φ_N are then integrated to fit the open flux estimate (e.g *Milan et al.*, 2012). This approach was also attempted early in the present study. However, the integration method has led to poor results as will be discussed in this section.

In the first approach, a similar method to that used in *Laundal et al.* (2020) (Sec. 2.10) was applied. Coefficients for the geomagnetic indices were estimated by applying Equation 2.15 over long timescales. Equation 2.18 was then applied, estimating the nightside reconnection rate using different geomagnetic indices. Φ_D and Φ_N, estimated from Equation 2.18, were then integrated so they could be compared to the open flux series from AMPERE. This method was attempted using different timescales and combining different indices as proxies for Φ_N, but some underlying issues limit this approach: The dayside and nightside reconnection rates estimated with this method do not exactly cancel each other out, such that the integrated reconnection rates lead to the estimated open flux to diverge into greater positive or negative values for increasing periods. This means that the estimated open flux becomes increasingly unreliable as time passes since errors from previous values propagate into later values due to the integration. Additionally, several data gaps exist in Φ_D and in some of the

indices, which are also problematic when integrating the data, leading to further propagation of errors.

Another method, based on multivariate regression analysis similar to the method in Section 3.5, was also explored. Instead of estimating the change in open flux with Φ_D and different indices, the explanatory variables were instead integrated and used in a regression model to estimate the open flux. The problem with this approach was that the coefficients became increasingly muted when building a model with data over a more extended period. The model can work reasonably well when only examining a single day, but for more extended periods, it becomes problematic with the coefficients reaching negligible values.

5.4 Estimating the Open Flux Error

When building a model based on Equation 2.2, the change in open flux estimated from the AMPERE open flux series is arguably one of the least accurate variables. By estimating the error in dF_{fit}/dt, the accuracy of the variable can be estimated. Since dF_{fit}/dt is a derivative based on F_{AMPERE}, it can be written as a finite difference:

$$f_i = a(A_i - A_{i-1}) \tag{5.1}$$

where f represents the change in open flux, A represents the open flux and a is a proportionality constant. With the change in flux given in Wb s^{-1} and assuming there are 10 min between independent AMPERE fits, we get the coefficient $a = 1/(10 \cdot 60s)$. From Equation 5.1, we obtain the following propagation of uncertainty:

$$\sigma_f^2 = 2a^2\sigma_A^2(1 - \rho_A) \tag{5.2}$$

where σ_f and σ_A are the uncertainties of f and A, respectively, and ρ_A is the autocorrelation of A. Before finding the uncertainty in the flux change, we must first find a value for the uncertainty in the AMPERE open flux. As outlined in Section 3.1, there are several steps in calculating the AMPERE open flux, each with a certain level of uncertainty. One important source of variance is the one degree accuracy of the R1/R2 boundary circle fits. A one degree increase or decrease in colatitude radius leads to significant jumps in the open flux values, depending on how large the radius is. A one degree increase in colatitude at high latitudes causes a smaller increase in open flux than a one degree increase at lower latitudes, due to the area within the OCB having a quadratic relationship with the radius. For example, in the AMPERE data set, there is a 31 MWb difference between a 10° and 11° colatitude circle fit,

and a 103 MWb difference between a 29° and 30° fit, on average. More typically observed, a one degree increase from 17° to 18° increases the open flux by 64 MWb, on average.

The mean change in open flux per change in colatitude can be written on the form, $dF_{\text{AMPERE}}(\Lambda)/d\Lambda$. By assuming the AMPERE method can accurately estimate the colatitude of the R1/R2 current boundary the main source of uncertainty is given by the one degree accuracy, which subsequently means the uncertainty in the open flux can be approximated as:

$$\sigma_A(\Lambda) = \frac{1}{\sqrt{N}} \frac{dF_{\text{AMPERE}}(\Lambda)}{d\Lambda} \tag{5.3}$$

where N is the number of degrees of freedom in F. The open flux series used is the polynomial fit with 90 min averaging. With there being 10 min between independent AMPERE fits, we then have 9 independent measurements when fitting the open flux, such that $N = 9$.

Autocorrelation, presented earlier in Section 3.5.3, is the correlation of a series with a delayed copy of itself. For ρ_A, it is the autocorrelation of F_{fit} we will find, since this open flux series is assumed to be the most accurate. F_{fit} was estimated from the 90 min polynomial fit function, meaning there is a 90 min difference between two independent values in the series, such that the autocorrelation should be found at a lag of 90 min. With a lag of 90 min, the autocorrelation of A is found to be $\rho_A = 0.715$.

Figure 5.1 presents how σ_A and σ_f changes with increasing magnetic colatitude, Λ. The vertical axis on the right hand side shows the uncertainty of σ_A, and the axis on the left hand side shows the uncertainty of σ_f, calculated with Equation 5.2.

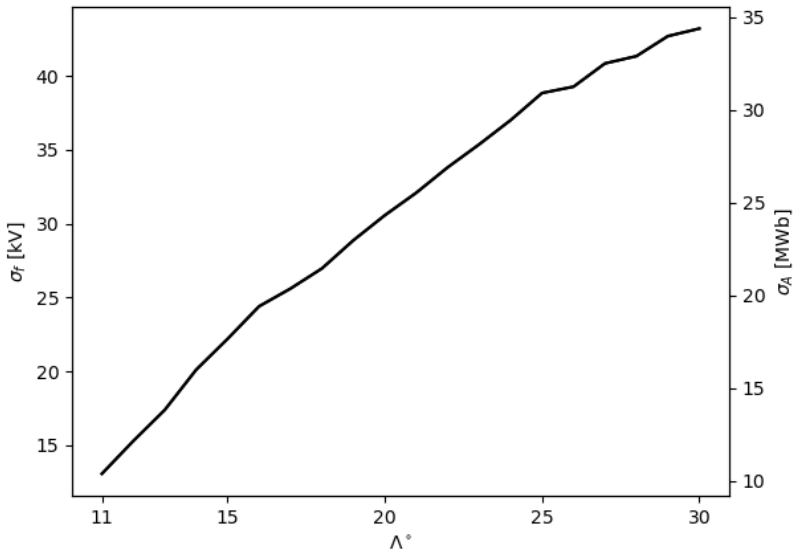

Figure 5.1: σ_A and σ_f as a function of geomagnetic colatitude.

The error graph for σ_f and σ_A in Figure 5.1 can be considered a best-case scenario for the errors in F_{PC} and dF_{PC}/dt, where the R1/R2 current boundary is assumed to be accurately estimated within one degree.

Looking at the AMPERE open flux series from the figures in Section 4.3, we find examples of events with different qualities of the boundary estimates: At time 1930 UT, 07 October 2015 (Fig. 4.5), there is an immediate two minute drop from 24° colatitude to 20° colatitude and back again. Such a brief and abrupt change in the polar cap size is most likely due to the current boundary being incorrectly fitted to 20° colatitude. This difference gives an open flux estimate error of $\sigma_A \approx 117$ MWb, which equates to $\sigma_f \approx 148$ kV, much greater than the errors presented in Figure 5.1. This error is also related to a fit of relatively high quality of 0.83. For lower quality periods, the error can be much more extreme, for example at time 0104, 4 March 2010 (Fig. 4.3). Here we see a sharp spike between 30° and 14° colatitude, resulting in errors of $\sigma_A \approx 433$ MWb and $\sigma_f \approx 543$ kV. Figure 4.6 is an example of a period where of the R1/R2 current boundary fit stays accurate within one degree. From 0400, 20 December 2015 until the end of the day, we only see one degree increments or decrements in the R1/R2 boundary fit colatitudes, indicating that the fits should be accurate within one degree colatitude.

Judging by the figures in Section 4.3 and the general trend of the R1/R2 boundary fits, it is very difficult to make a generalised estimate of the error in F_{PC} and dF_{PC}/dt. When looking at individual events, one might resort to some guesswork at within how many degrees the accuracy of the boundary fit lies.

5.4.1 OCB Boundary Correction Error

Looking back at the OCB boundary correction term, *K*, presented in Section 3.1.3, the correction term was estimated as from median offset between the OCB and the R1/R2 boundary. Figure 3.3 shows the median offsets with associated error bars for each MLT bin. Here, the error bars suggest the offset between the OCB and the R1/R2 boundary varies by several degrees. From this, we can assume the median OCB offset is not representative of the OCB offset at all times, meaning the OCB offset could differ on a case to case basis, leading to additional errors in the open flux estimates.

5.5 Determining the Best Model for Estimating the Open Flux Change / Nightside Reconnection Rate

Three different regression models were created in the previous chapters to estimate various variables. The first model, $(dF/dt)_{\text{reg}}$, presented in 3.5, estimated the open flux change, using Φ_D, *SML** and *ASY-H* as variables. The second model, $\Phi_{N,\text{reg}}$, presented in Section 4.2.1, estimated the nightside reconnection rate, $\Phi_N = \Phi_D - dF_{\text{fit}}/dt$, using *SML**, *ASY-H* and *PCN* as variables. The last model, F_{reg}, presented in Section 4.2.2, estimated the open magnetic flux using Φ_D, *SML**, *ASY-H* and *PCN*.

The open flux model, F_{reg}, was made since Φ_D and the geomagnetic indices showed a much higher correlation with F_{fit} than with dF_{fit}/dt, (Fig. 3.9). We also see the R-squared being significantly higher than the other models at 0.538. Despite the higher correlation, the open flux model is found to poorly reflect dF_{fit}/dt when differentiated, suggesting this model is worse than the others at detecting flux changes. The differentiated open flux model is not included in the event plots to keep the plots as simple as possible without much visual noise. The worse performance also has a physical explanation since Φ_D and the geomagnetic indices, assuming the indices are proportional with the nightside reconnection rate, are both describing flux change, not flux content. The high correlation of this model is mainly due to the independent variables generally are greater in magnitude when the open flux is also large, not because the variables are necessarily better at predicting the open flux at any given time.

When determining the best proxy for estimating the nightside reconnection rate, the two other models are better candidates. The models are compared to dF_{fit}/dt to determine which model has the better fit. The c panels in Section 4.3 shows this comparison with $(dF/dt)_{\text{reg}}$, and the d panels show the comparison with $\Phi_{N,\text{reg}}$ subtracted from Φ_D. Both models are very similar, the main difference being the $\Phi_{N,\text{reg}}$ model generally having values of greater magnitude. An issue with the $(dF/dt)_{\text{reg}}$ is that the magnitude of the dayside and nightside reconnection rates appear too low compared to dF_{fit}/dt. The Φ_D coefficient in this model is about 0.51, while a value closer to 1 is expected since Φ_D and dF_{fit}/dt are given in the same units. In the $\Phi_{N,\text{reg}}$ we remedy this issue by fitting the indices to the dependent variable given as $\Phi_N = \Phi_D - dF_{\text{fit}}/dt$. In this situation dF_{fit}/dt, Φ_D and Φ_N all have the same absolute magnitude in accordance with the ECPC. Comparing the two methods, we also find the $\Phi_{N,\text{reg}}$ model to show the best resemblance with dF_{fit}/dt, making it the best proxy for the open flux change and, by extension, the nightside reconnection rate.

Chapter 6

Conclusions

6.1 Conclusions

6.2 Using AMPERE to Monitor Changes in Open Flux

An open flux time series, F_{fit}, covering almost seven whole years, was estimated for the northern hemisphere. F_{fit} was estimated by performing a rolling 90 min 2nd order polynomial curve fit on open flux data derived from AMPERE Birkeland current maps.

Comparing F_{fit} to solar wind measurements and various geomagnetic indices, we see the open flux estimates tend to be wildly inaccurate during low activity periods. F_{fit} will often predict significant changes in open flux while there should be little to no reconnection activity, which violates the assumptions of the ECPC. This trend can be observed in the quiet periods of Figure 4.3.

For higher activity periods, however, F_{fit} is more accurate as the R1/R2 current boundary, correlated with the OCB, becomes easier to identify with stronger Birkeland currents. The AMPERE quality parameter reflects the magnitude of the Birkeland currents. The events presented in Figures 4.5 & 4.6 are two of the best periods found when comparing dF_{fit}/dt and the estimated open flux change through multivariate regression. These are both very high activity periods where Φ_D exceeds 100 kV, placing these events in the 99th percentile in terms of dayside reconnection activity.

We conclude that the open flux estimates are more accurate at higher activity periods based on the improved correlation with Φ_D and the geomagnetic indices and the noise reduction in the AMPERE open flux series. However, we can not confirm exactly how accurate the open flux estimates are in these higher-quality periods since we have no other simultaneous measurements or estimates of the open magnetic flux to compare with F_{fit}.

6.3 Producing a Nightside Reconnection Rate Proxy using Geomagnetic Indices

We used multivariate regression analysis to create three different regression models using Φ_D and various geomagnetic indices as independent variables. Of these models, $(dF/dt)_{\text{reg}}$ was designed to predict the open flux change, $\Phi_{N,\text{reg}}$ was designed to predict the nightside reconnection rate derived from $\Phi_N = \Phi_D - dF_{\text{fit}}/dt$, and F_{reg} to predict the open flux. Of these models, $\Phi_{N,\text{reg}}$ is concluded to offer the best proxy of the nightside reconnection rate and, by extension, the open flux change. We obtain the following representation of the ECPC:

$$\frac{dF_{PC}}{dt} = \Phi_D - \Phi_{N,\text{reg}} \tag{6.1}$$

The open flux change derived from Equation 6.1 and dF_{fit}/dt, respectively, have a Pearson correlation factor of about 0.32. The correlation is improved to 0.42 if ignoring AMPERE data with quality parameters below 0.5. These correlations mean that still more than half of the variation in dF_{fit}/dt is not being explained by the model. However, since we assume dF_{fit}/dt tend to be very inaccurate at depicting the real open flux change, the indices may be better at predicting the nightside reconnection rate than our model suggests. Since we do not know how precise our open flux estimate is, we cannot effectively predict how accurate the regression model is. From the study performed in *Laundal et al.* (2020), we can assume the use of geomagnetic indices is a viable method for predicting the nightside reconnection rate. For our approach to work, a more accurate estimate of the open magnetic flux is necessary.

References

Akasofu, S. I. (2011), A historical review of the geomagnetic storm-producing plasma flows from the sun, doi:10.1007/s11214-011-9856-y.

Anderson, B. J., K. Takahashi, and B. A. Toth (2000), Sensing global Birkeland currents with Iridium engineering magnetometer data, *Geophysical Research Letters*, *27*(24), doi:10.1029/2000GL000094.

Anderson, B. J., K. Takahashi, T. Kamei, C. L. Waters, and B. A. Toth (2002), Birkeland current system key parameters derived from Iridium observations: Method and initial validation results, *Journal of Geophysical Research: Space Physics*, *107*(A6), doi:10.1029/2001JA000080.

Anderson, B. J., H. Korth, C. L. Waters, D. L. Green, and P. Stauning (2008), Statistical Birkeland current distributions from magnetic field observations by the Iridium constellation, *Annales Geophysicae*, *26*(3), doi:10.5194/angeo-26-671-2008.

Anderson, B. J., H. Korth, C. L. Waters, D. L. Green, V. G. Merkin, R. J. Barnes, and L. P. Dyrud (2014), Development of large-scale Birkeland currents determined from the Active Magnetosphere and Planetary Electrodynamics Response Experiment, *Geophysical Research Letters*, *41*(9), doi:10.1002/2014GL059941.

Anderson, B. J., H. Korth, D. T. Welling, V. G. Merkin, M. J. Wiltberger, J. Raeder, R. J. Barnes, C. L. Waters, A. A. Pulkkinen, and L. Rastaetter (2017), Comparison of predictive estimates of high-latitude electrodynamics with observations of global-scale Birkeland currents, *Space Weather*, *15*(2), doi:10.1002/2016SW001529.

Axford, W. I., and C. O. Hines (1961), A UNIFYING THEORY OF HIGH-LATITUDE GEOPHYSICAL PHENOMENA AND GEOMAGNETIC STORMS, *Canadian Journal of Physics*, *39*(10), doi:10.1139/p61-172.

Bengfort, B., R. Bilbro, N. Danielsen, L. Gray, K. McIntyre, P. Roman, Z. Poh, et al. (2018), Yellowbrick, doi:10.5281/zenodo.1206264.

Borovsky, J. E., and J. A. Valdivia (2018), The Earth's Magnetosphere: A Systems Science Overview and Assessment, doi:10.1007/s10712-018-9487-x.

Burrell, A. G., G. Chisham, S. E. Milan, L. Kilcommons, Y. J. Chen, E. G. Thomas, and B. Anderson (2020), AMPERE polar cap boundaries, *Annales Geophysicae*, *38*(2), doi:10.5194/angeo-38-481-2020.

Chapman, S., and V. C. A. Ferraro (1931), A new theory of magnetic storms, *Journal of Geophysical Research*, *36*(2), doi:10.1029/te036i002p00077.

Cowley, S., and M. Lockwood (1992), Excitation and decay of solar-wind driven flows in the magnetosphere-ionosphere system, *Annales Geophysicae*, *10*.

Coxon, J. C., S. E. Milan, L. B. Clausen, B. J. Anderson, and H. Korth (2014), The magnitudes of the regions 1 and 2 Birkeland currents observed by AMPERE and their role in solar wind-magnetosphere-ionosphere coupling, *Journal of Geophysical Research: Space Physics*, *119*(12), doi:10.1002/2014JA020138.

Dungey, J. W. (1961), Interplanetary magnetic field and the auroral zones, *Physical Review Letters*, *6*(2), doi:10.1103/PhysRevLett.6.47.

Frey, H. U., S. B. Mende, V. Angelopoulos, and E. F. Donovan (2004), Substorm onset observations by IMAGE-FUV, *Journal of Geophysical Research: Space Physics*, *109*(A10), doi:10.1029/2004JA010607.

Fukushima, N. (1994), Some topics and historical episodes in geomagnetism and aeronomy, *Journal of Geophysical Research*, *99*(A10), doi:10.1029/94ja00102.

Gjerloev, J. W. (2012), The SuperMAG data processing technique, *Journal of Geophysical Research: Space Physics*, *117*(9), doi:10.1029/2012JA017683.

Huang, C. S. (2005), Variations of polar cap index in response to solar wind changes and magnetospheric substorms, *Journal of Geophysical Research: Space Physics*, *110*(A1), doi:10.1029/2004JA010616.

Iijima, T., and T. A. Potemra (1976), Field-aligned currents in the dayside cusp observed by Triad, *Journal of Geophysical Research*, *81*(34), doi:10.1029/ja081i034p05971.

Imber, S. M., S. E. Milan, and B. Hubert (2006), The auroral and ionospheric flow signatures of dual lobe reconnection, *Annales Geophysicae*, *24*(11), doi:10.5194/angeo-24-3115-2006.

Iyemori, M. T. M. N. Y. O., T., and H. Toh (2010), Mid-latitude geomagnetic indices asy and sym for 2009 (provisional).

Kauristie, K., A. Morschhauser, N. Olsen, C. C. Finlay, R. L. McPherron, J. W. Gjerloev, and H. J. Opgenoorth (2017), On the Usage of Geomagnetic Indices for Data Selection in Internal Field Modelling, doi:10.1007/s11214-016-0301-0.

Kilcommons, L. M., R. J. Redmon, and D. J. Knipp (2017), A new DMSP magnetometer and auroral boundary data set and estimates of field-aligned currents in dynamic auroral boundary coordinates, *Journal of Geophysical Research: Space Physics*, *122*(8), doi:10.1002/2016JA023342.

Kivelson, M. G., C. T. Russell, and M. E. Brown (1996), Introduction to Space Physics , *Physics Today*, *49*(4), doi:10.1063/1.2807586.

Laundal, K. M., S. E. Haaland, N. Lehtinen, J. W. Gjerloev, N. Østgaard, P. Tenfjord, J. P. Reistad, K. Snekvik, S. E. Milan, S. Ohtani, and B. J. Anderson (2015), Birkeland current effects on high-latitude ground magnetic field perturbations, *Geophysical Research Letters*, *42*(18), doi:10.1002/2015GL065776.

Laundal, K. M., J. P. Reistad, S. M. Hatch, T. Moretto, A. Ohma, N. Østgaard, P. A. Tenfjord, C. C. Finlay, and C. Kloss (2020), Time-scale dependence of solar wind-based regression models of ionospheric electrodynamics, *Scientific Reports*, *10*(1), doi:10.1038/s41598-020-73532-z.

Milan, S. E. (2015), Sun et Lumière: Solar wind-magnetosphere coupling as deduced from ionospheric flows and polar auroras, in *Astrophysics and Space Science Proceedings*, vol. 41, doi:10.1007/978-3-319-18359-6{_}2.

Milan, S. E., S. W. Cowley, M. Lester, D. M. Wright, J. A. Slavin, M. Fillingim, C. W. Carlson, and H. J. Singer (2004), Response of the magnetotail to changes in the open flux content of the magnetosphere, doi:10.1029/2003JA010350.

Milan, S. E., G. Provan, and B. Hubert (2007), Magnetic flux transport in the Dungey cycle: A survey of dayside and nightside reconnection rates, *Journal of Geophysical Research: Space Physics*, *112*(1), doi:10.1029/2006JA011642.

Milan, S. E., J. S. Gosling, and B. Hubert (2012), Relationship between interplanetary parameters and the magnetopause reconnection rate quantified from observations of the expanding polar cap, *Journal of Geophysical Research: Space Physics*, *117*(3), doi:10.1029/2011JA017082.

Milan, S. E., J. A. Carter, H. Korth, and B. J. Anderson (2015), Principal component analysis of Birkeland currents determined by the Active Magnetosphere and Planetary Electro-

dynamics Response Experiment, *Journal of Geophysical Research: Space Physics*, *120*(12), doi:10.1002/2015JA021680.

Milan, S. E., L. B. Clausen, J. C. Coxon, J. A. Carter, M. T. Walach, K. Laundal, N. Østgaard, P. Tenfjord, J. Reistad, K. Snekvik, H. Korth, and B. J. Anderson (2017), Overview of Solar Wind–Magnetosphere–Ionosphere–Atmosphere Coupling and the Generation of Magnetospheric Currents, doi:10.1007/s11214-017-0333-0.

Milan, S. E., J. A. Carter, G. E. Bower, S. M. Imber, L. J. Paxton, B. J. Anderson, M. R. Hairston, and B. Hubert (2020), Dual-Lobe Reconnection and Horse-Collar Auroras, *Journal of Geophysical Research: Space Physics*, *125*(10), doi:10.1029/2020JA028567.

Newell, P. T., and J. W. Gjerloev (2011), Evaluation of SuperMAG auroral electrojet indices as indicators of substorms and auroral power, *Journal of Geophysical Research: Space Physics*, *116*(12), doi:10.1029/2011JA016779.

Newell, P. T., and J. W. Gjerloev (2014), Local geomagnetic indices and the prediction of auroral power, *Journal of Geophysical Research: Space Physics*, *119*(12), doi:10.1002/2014JA020524.

Newell, P. T., T. Sotirelis, K. Liou, C. I. Meng, and F. J. Rich (2007), A nearly universal solar wind-magnetosphere coupling function inferred from 10 magnetospheric state variables, *Journal of Geophysical Research: Space Physics*, *112*(1), doi:10.1029/2006JA012015.

Ohma, A., N. Østgaard, J. P. Reistad, P. Tenfjord, K. M. Laundal, K. Snekvik, S. E. Haaland, and M. O. Fillingim (2018), Evolution of Asymmetrically Displaced Footpoints During Substorms, *Journal of Geophysical Research: Space Physics*, *123*(12), doi:10.1029/2018JA025869.

Parker, E. N. (1958), Dynamics of the Interplanetary Gas and Magnetic Fields., *The Astrophysical Journal*, *128*, doi:10.1086/146579.

Parker, E. N. (1996), The alternative paradigm for magnetospheric physics, *Journal of Geophysical Research: Space Physics*, *101*(A5), doi:10.1029/95ja02866.

Pedregosa, F., G. Varoquaux, A. Gramfort, V. Michel, B. Thirion, O. Grisel, M. Blondel, P. Prettenhofer, R. Weiss, V. Dubourg, J. Vanderplas, A. Passos, D. Cournapeau, M. Brucher, M. Perrot, and Duchesnay (2011), Scikit-learn: Machine learning in Python, *Journal of Machine Learning Research*, *12*.

Perreault, P., and S. kasofu (1978), A study of geomagnetic storms, *Geophysical Journal of the Royal Astronomical Society*, *54*(3), doi:10.1111/j.1365-246X.1978.tb05494.x.

Redmon, R. J., W. F. Denig, L. M. Kilcommons, and D. J. Knipp (2017), New DMSP database of precipitating auroral electrons and ions, *Journal of Geophysical Research: Space Physics*, *122*(8), doi:10.1002/2016JA023339.

Reiff, P. H., R. W. Spiro, and T. W. Hill (1981), Dependence of polar cap potential drop on interplanetary parameters, *Journal of Geophysical Research: Space Physics*, *86*(A9), doi:10.1029/ja086ia09p07639.

Richmond, A. D. (1995), Ionospheric Electrodynamics Using Magnetic Apex Coordinates., *Journal of geomagnetism and geoelectricity*, *47*(2), doi:10.5636/jgg.47.191.

Scurry, L., and C. T. Russell (1991), Proxy studies of energy transfer to the magnetosphere, *Journal of Geophysical Research*, *96*(A6), doi:10.1029/91ja00569.

Seabold, S., and J. Perktold (2010), Statsmodels: Econometric and Statistical Modeling with Python, in *Proceedings of the 9th Python in Science Conference*, doi:10.25080/majora-92bf1922-011.

Slavin, J. A., E. J. Smith, D. G. Sibeck, D. N. Baker, R. D. Zwickl, and S.-I. Akasofu (1985), An ISEE 3 study of average and substorm conditions in the distant magnetotail, *Journal of Geophysical Research*, *90*(A11), doi:10.1029/ja090ia11p10875.

Thébault, E., C. C. Finlay, C. D. Beggan, P. Alken, J. Aubert, O. Barrois, F. Bertrand, T. Bondar, A. Boness, L. Brocco, E. Canet, A. Chambodut, A. Chulliat, P. Coïsson, F. Civet, A. Du, A. Fournier, I. Fratter, N. Gillet, B. Hamilton, M. Hamoudi, G. Hulot, T. Jager, M. Korte, W. Kuang, X. Lalanne, B. Langlais, J. M. Léger, V. Lesur, F. J. Lowes, S. Macmillan, M. Mandea, C. Manoj, S. Maus, N. Olsen, V. Petrov, V. Ridley, M. Rother, T. J. Sabaka, D. Saturnino, R. Schachtschneider, O. Sirol, A. Tangborn, A. Thomson, L. Tøffner-Clausen, P. Vigneron, I. Wardinski, and T. Zvereva (2015), International geomagnetic reference field: The 12th generation international geomagnetic reference field - The twelfth generation, *Earth, Planets and Space*, *67*(1), doi:10.1186/s40623-015-0228-9.

Troshichev, O. A., and V. G. Andrezen (1985), The relationship between interplanetary quantities and magnetic activity in the southern polar cap, *Planetary and Space Science*, *33*(4), doi:10.1016/0032-0633(85)90086-8.

Waters, C. L., B. J. Anderson, and K. Liou (2001), Estimation of global field aligned currents using the iridium® system magnetometer data, *Geophysical Research Letters*, *28*(11), doi:10.1029/2000GL012725.

Waters, C. L., B. J. Anderson, D. L. Green, H. Korth, R. J. Barnes, and H. Vanhamäki (2020), Science Data Products for AMPERE, in *Ionospheric Multi-Spacecraft Analysis Tools*, doi: 10.1007/978-3-030-26732-2{_}7.